Doctoral Dissertation

Tectono-metamorphic evolution of the Himalayan metamorphic rocks: Insights from the Mandakini and Madhmaheswar Ganga river valley, Northwestern India

(ヒマラヤ変成岩の造構－変成発展史：北西インドの Mandakini および Madhmaheswar Ganga 川峡谷地域からの考察)

Shivaji Saha

Graduate School of Science, Hokkaido University

Department of Natural History Sciences

2020, September

“Look at the sky. We are not alone. The whole universe is friendly to us and conspires only to give the best to those who dream and work.”

Dr. A.P.J. Abdul Kalam

Abstract

Evolutionary signatures of active mountain building tectonic process as a consequence of collision between Indian plate and Tibetan plate are well preserved in the Himalayan metamorphic rocks. The ductile deformation of the crust caused by the Main Central Thrust which in turn, resulted from southward extrusion of high grade metamorphic rocks (amphibolite to granulite facies) of Greater Himalayan Sequence (GHS) over low grade (greenschist facies) Lesser Himalayan Sequence (LHS) creating an inverted metamorphic field gradient across the MCT. The study area in NW Himalaya along Madhmaheswar Ganga valley, Rudraprayag district, Uttarakhand, India is comprised of Munsiari formation and Vaikrita group of rocks (lower GHS). Garnet-kyanite bearing migmatitic gneiss of lower GHS (~ 3 km thickness) was juxtaposed over orthogneiss and garnet bearing metapellites of Munsiari formation (~ 7 km thickness) by north-easterly dipping MCT. Intercalations of metabasic rocks are persistent throughout Munsiari formation. An inverted Barrovian sequence is persistent from biotite zone through garnet zone upto kyanite zone where kyanite-in isograd lies immediately above the MCT.

In order to understand the inverted metamorphism along with the deformation condition in the study area, it is important to characterize the tectonic behavior of the rocks with increasing structural level across the MCT by means of microstructural observations and metamorphic P-T conditions of equilibrium mineral assemblages. Therefore, detailed microstructural analysis is necessary to define the shear zone by the degree of strain intensification across the MCT. This study aims at investigating the heterogeneity of the deformational behavior of quartz grains in terms of thickness of quartz layers and other associated phases along with the understanding of fabric development with respect to the MCT.

Microstructural observations are essentially focused on the quartzo-feldspathic gneiss of the Munsiari formation and L-GHS. Quartz microstructures from lower part of the Munsiari formation are generally characterized by subgrain rotation recrystallization (SGR). Some domains of polygonal quartz grains with triple point junction indicate SGR followed by static grain growth. Whereas, lobate boundaries of quartz grains with sweeping extinction and deformation lamellae has been documented from upper Munsiari formation indicating high temperature grain boundary

migration (GBM) overprinted by late stage low temperature deformation. Quartz grains in the L-GHS rocks are coarser than that of the Munsiari rocks and highly irregular in shape. High temperature deformation is evidenced by the presence of elongated subgrains and chessboard pattern extinction of quartz.

To carry out further microstructural studies, 14 samples were selected for EBSD analysis. Monomineralic quartz-rich and polyphase domains has been subjected to the investigation by means of understanding the development of Quartz LPO fabric across the MCT. Quartz *c*-axis fabric from quartz-rich domains of the Munsiari formation rocks shows a series of type-*II* crossed girdle fabrics with *Y*-maximum. Here, the quartz *c*-axes are aligned parallel to intermediate finite strain axis *Y*, revealing the intracrystalline deformation by active prism {10‑10} <a> slip system. In contrast, c-axis orientations obtained from thin monomineralic quartz layers (thickness 72-163 μm) records girdles ranging from small circle girdles to type-*I* crossed girdle fabric with r-maxima. In this case, the rhombohedral plane of quartz is aligned parallel to the foliation plane (*XY*), which indicate basal (0001) <a> slip and rhomb {10‑11} <a> slip system activity. Thus, there is an effect of thickness of monophase layers on fabric development and, perhaps the role of other phases has a strong impact on the fabric development for thin monomineralic layers.

On the other hand, polyphase domains are characterized by the quartz grains totally surrounded by other phases. The size of recrystallized quartz grains within polyphase domain increases from ~64.4 μm in Munsiari to ~109 μm in L-GHS. C-axes orientations are random for the Munsiari samples. Whereas, C-axis fabric with point maxima is observed for the L-GHS samples. However, those fabric patterns are strengthened with increasing modal abundance of quartz.

The strength of the quartz *c*-axis fabric is quantified as a function of eigenvectors (λ_1 = maximum; λ_2 = intermediate; λ_3 = minimum) from *c*-axes orientation distribution. Following Vollmer (1990), three end member fabric types are determined from these eigenvectors; those are point (*P*), girdle (*G*) and random (*R*). Then, by introducing cylindricity index (*B*) of Vollmer (1990), the variation in fabric strength of quartz LPO is shown as a function of strain localization throughout the Munsiari formation. Progressive increase in fabric intensity for both thin and quartz rich layers indicate an increase in strain towards the MCT.

The Geochemical studies are consisted of Garnet line profile analysis, X-ray elemental mapping for major elements such as Ca, Fe, Mn, Mg and the Point analysis of matrix minerals by an electron probe microanalyzer (EPMA). Garnets from the MCTZ and lowermost GHS are characterized by growth zoning with consistently decreasing X_{Mn} content from core to rim suggesting the grain growth during burial with increasing *P* and *T*. On the other hand, most of the garnet porphyroblasts in the L-GHS exhibit flat profile of X_{Mn} with little increase at rim. The diffusional zoning profile of the L-GHS garnets is a result of higher rate of diffusion of major elements at higher elevated temperature than that of growth zoning causing homogeneous distribution of these elements. Rim with higher X_{Mn} content signify retrograde reaction during exhumation and cooling of the lower GHS rocks. The results obtained from conventional thermobarometers is showing a peak *P-T* condition of 535 ± 25 °C and 5.8 ± 1.2 kbar from the assemblage of garnet + quartz + chlorite + chloritoid + plagioclase + biotite + muscovite ± ilmenite in the lowermost MCTZ. Whereas, the upper MCTZ rocks have experienced peak *P-T* condition of 632 ± 25 °C and 8.5 ± 1.2 kbar. In contrast, lowermost GHS experienced peak *P-T* condition of 683 ± 25 °C and 11 ± 1.2 kbar attained by the equilibrium assemblage of garnet + quartz + plagioclase + muscovite + biotite ± kyanite ± ilmenite ± rutile. a steep inverted pressure gradient of 16.4 ± 1.3 kbar km^{-1} persist between uppermost MCTZ sample and lowermost GHS sample which could suggest extreme thinning of rock strata due to MCT slip.

Acknowledgement

The idea to solve the mysterious questions which baffled mankind since the inception of consciousness triggered my ideology and personality to pursue my undying quest in the field of Geology (specify which field) under the aegis of Prof Toru Takeshita, whose aid and brace bolstered my idea to proliferate. Prof Takeshita‘s detailed insight and sagacious approach instigated my desire to complete this study.

Prof H. B. Srivastava, an altruist and adroit, was instrumental in tuning my career as a researcher.

Symbiosis and Proto-Cooperation are the most influential sociological phenomenon, which enhances your creativity and depth in the subject, which were provided by Dr. Subhajit Ghosh, Dr. Takeshi Imayama, Prof. Virginian Toy, Prof. Hafizur Rehman, Dr. Salvatore Iaccarino, Dr. Zach Michels and Debaditya Bandyopadhyay.

Field of Geology requires strenuous physical labor to accumulate the rock samples and immense mental strength, which were afforded and arranged by Dr. Subhajit Ghosh, Soumya Sarkar, Vinod Kumar Mauriya, Tapash Mahajan, Arjun Kumar, Iswar Rahi, Jitesh Srivastava and Suraj Rawat.

I am indebted to the members of Petrology and Petrotectonics Laboratory and Experimental Tectonics Laboratory (ETL), Department of Geology, Calcutta University, for their help me to make the things easier while working with the hand specimens for thin section preparation.

I would also like to thank K. Nakamura and H. Nomura for directing me through thin section preparation.

I would also like to extend my appreciation to Akiko Matsumoto for being there all the time when I was struggling with some error during EPMA and EBSD analysis at Hokkaido University.

It is with immense nostalgicity and emotion, I want to convey my heartfelt gratitude to Dr. Ayumi Okamoto for teaching me how to operate SEM-EDS and EPMA at Hokkaido University, Dr. Dinesh Pandit and Ryochi Kawabata for assisting me with the EPMA analysisat at Banaras Hindu University and Okayama University of Science and Dr. Thomas A. Czertowicz, and Dr. Dong Bui Van for EBSD analysis at Hokkaido University.

Man can not survive in discord. I feel blessed to have an amazing bunch of people from all around the world, with whom, I shared my days of ups and downs with. They are my family, they are 6G Lab members-Main Tokinaga, Dr. Hirokazu Masumoto, Kohei Yamashita, Dr. Dong Bui Van, Yuto Kimura, Kanji, Thomas Yeo, Kabangu Sakuwaha.

I am honor bound to reciprocate my fervor to the people who shaped me the way I am. Thanks to Dr. Sayantani Chatterjee, Dr. Rahul Jog and Chetna Sharma.

It would be preposterous to survive in foreign land without economic aid which were bestowed by Dr. Rahul Jog, Nirmit Sakre, Raj Kamal Kumar, Dr. Subhabrata Banerjee, Dr. Ram Avtar, Devika

Sasikumar, Dr. Subhajit Ghosh, Mayukh Talukdar, Santanu Bhattacharya, Dr. Prasenjit Dey, Debojit Talukdar.

In the land of austerity, it mesmerizes you to be part of a family which were provided by Indians in Okayama- Krishna Rao, Mandeep Singh and Abhinav K V.

I would especially like to thank Erica-san, Sarohdo-san and his family, Arisa-san and her family, for helping me in difficult time.

In the time of despair, I was beatified with the help from Dr. Yogendra Shah, Narmada Shah, Geoffrey Hughes, Samia Megh, Mohan Singh, Emiko Kato san who provided me with many part time jobs to sustain myself in the crisis.

Wencheng Huang and Arpan Chowdhury! You have done number of things for me when I was far away from Sapporo during COVID-19 pandemic. I greatly appreciate your help.

A human feels blessed when he/she is adorned with the boon of getting birth as a human. I was, I am and I will be the human being, the way I was nourish and nurtured by my parents and siblings who are the backbone of my life without whom I cant conceptualize the life it is. The blessing of my Late Father Mr. Damodar Saha, my mother Mrs. Pushpa Saha, elder sister Jayanti Saha and my soulmate twin Tania Saha made me believe that " You are far more than what you can conceive".

Contents

Chapter 5

Microstructural Analysis of Quartz in Monomineralic and Polyphase domains: A case study from Main Central Thrust (MCT) Zone Mylonites, western Himalaya, India

List of Figures

List of Tables

Chapter 1

Introduction

1.1. Himalayan orogenic belt

Continuous convergence of Indian and Asian plate since early Cenozoic time (~55Ma) gave rise to the formation of the Himalayan orogenic belt (Najman et al., 2010, 2017). The **Main Himalayan Thrust (MHT)** appeared as a detachment surface which facilitate the underthrusting of the Indian plate beneath Eurasia (Seeber and Armbruster, 1981; Zhao et al., 1993). With gradual compression from suture zone to foreland, crustal architecture in the Himalayas has been evolved into four major stratigraphic unit bounded by north-easterly dipping major thrust and normal fault system (Figure 1.1) (Gansser 1964; Le Fort, 1975; Hodges, 2000; Yin, 2006). Those thrust faults diverge extremely from the MHT (Nelson et al., 1996; Avouac, 2007).

Collision between two plates resulted in the formation of the **Indus–Tsangpo suture zone** (ITSZ), which ranges over 2000 kilometers in southern Tibet and separates the tectonic units of Gondwana affinities in the south from those of Eurasia in the north. (Aitchison et al., 2011; Replumaz et al., 2014). The ITSZ is structurally confined to the south by a triassic-cretaceous flysch unit and the north by the south-dipping Great Counter Thrust. (Yin, 2006). However, the Great Counter Thrust correlates locally with the northerly vergent thrust mechanism in the ITSZ. (Heim and Gansser, 1939; Ratschbacher et al., 1994; Yin et al., 1999). Ophiolites are found as discontinuous bodies along the ITSZ which have been regarded as remnants of the Jurassic–Cretaceous Neotethyan oceanic lithosphere originated from a seafloor spreading system that evolved between India and Asia during the Mesozoic (Nicolas et al., 1981; Allegre et al., 1984). Recent studies have shown that the ITSZ ophiolites formed in a suprasubduction zone environment (e.g. Hébert et al., 2003; Bédard et al., 2009) during the late Jurassic–early Cretaceous (Hébert et al., 2012). A flysch complex with blocks of Upper Permian platform limestone, lower Triassic pelagic limestone, serpentinite, late Cretaceous calcschist and basaltic pillow lavas, is structurally located below the entire ITSZ to the south. (e.g., Von, 1902; Heim and Gansser, 1939).

The northernmost unit called as **Tethyan Himalayan Sequence (THS)** is containing weakly metamorphosed sedimentary rock of passive continental margin of the Indian plate (Mid-

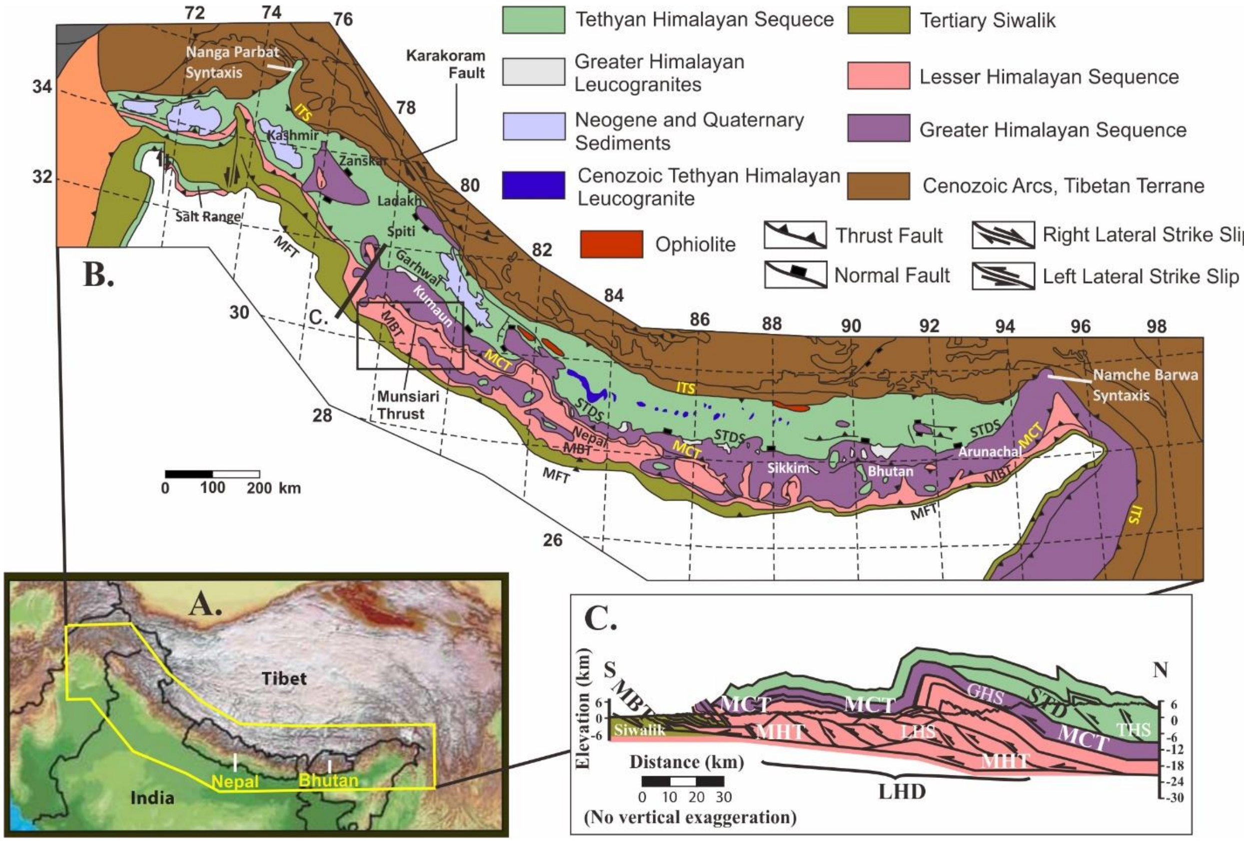

Figure 1.1. (A) Digital elevation model of the Himalaya and neighboring regions (Kohn 2007, 2014); Yellow polygon is drawn to show the range of the mountain belt presented in (B). (B) Simplified regional geologic map of the Himalaya (modified from Yin, 2006) illustrating main lithotectonic units; Black box showing the location of Kumaun-Garhwal Himlaya; Black line is the section line representing the cross section of western Himalaya. (C) Generalised cross section of western Himalaya exhibiting the distribution of major lithotectonic elemnts of the Himalayan orogeny (modified after Kohn, 2014). Geologic abbreviations: ITS, Indus Tsangpo Suture; LHD, Lesser Himalayan Duplex; MBT, Main Boundary Thrust; MCT, Main Central Thrust; MFT, Main Frontal Thrust; MHT, Main Himalayan Thrust; STDS, South Tibetan Detachment System.

Proterozoic to Cretaceous) (Brookfield, 1993; Jadoul et al., 1998; Yin, 2006). Hence, the THS represents syn-collisional deformation features along with the Eocene crustal thickening event (Garzanti, 1999; Godin, 2003; Aikman et al., 2008). Moreover, high-pressure metamorphic complex reported by Laskowski et al. (2016) suggests initial steep subduction of Indian passive margin at ca. 40 Ma. **Southern Tibetan Detachment System (STDS)** of normal faults with top-to-the-NE shear sense, marks the base of the THS (Burchfiel et al., 1992; Burg et al., 1984) and therefore, overprinted over the early Oligocene to the early Miocene ductile structures during the middle Miocene period (e.g., Carosi et al., 1998; Cottle et al., 2007; Iaccarino et al., 2017; Searle et al., 2003; Soucy La Roche et al., 2016).

Proterozoic to early Paleozoic metasedimentary rock of **Greater Himalayan Sequence (GHS)** (Parrish & Hodges, 1996; Gehrels et al., 2011) was started to exhume from mid-crustal depth ~ 20-23 m.y ago via concomitant activity of the **Main Central Thrust** (**MCT**; Vaikrita Thrust by Valdiya, 1980) below and the STDS above (Hodges et al., 1992; Parrish and Hodges, 1996; Godin et al., 2006b). According to Soucy La Roche et al., (2018), prograde metamorphism of GHS rocks persisted within the time period of 40-35 Ma led by the peak metamorphic event between 35 and 30 Ma.

Variable lithologies of the MCT footwall characterize the **Lesser Himalayan Sequence (LHS)** containing metasedimentary rocks of late Paleoproterozoic to early Mesoproterozoic age, sedimentary rocks of late Carboniferous to Permian age (Gondowana succession) and foreland basin sediments of Eocene to early Miocene age together with the ca. 1800-1830 Ma intrusives of granite and gabbro (DeCelles et al., 2004; Gehrels et al., 2011; Martin, 2017a; Najman et al., 2005, and references therein). Deformation of LHS rocks was accomplished through the development of the Lesser Himalayan Duplex (LHD) system (Srivastava and Mitra, 1994; DeCelles et al., 2001; Robinson et al., 2003). Another crustal scale fault within the LHS called the Ramgarh-Munsiari thrust carrying Paleoproterozoic rocks of the LHS, has been mapped through almost entire orogenic belt (Srivastava and Mitra, 1994; Pearson and DeCelles, 2005; Bhattacharya and Mitra, 2009; Robinson and Pearson, 2013; Mandal et al., 2015) and Robinson and Pearson (2013) explained it as a roof thrust of LHD system. Recent
study in north western Himalaya of Stübner et al. (2018) proposed the late Miocene to early Pliocene evolution of LHD system by accreting ramp over MHT. Whereas, the name, **Lesser Himalayan Crystalline Sequence (LHCS)**, has been given to denote low to medium metamorphic grade hanging-wall rocks of the Munsiari thrust (Pecher, 1989; Vannay and Grasemann, 1998). LHCS and a part of the lower GHS was subjected to ductile deformation during MCT activity by forming a wide shear zone called the **MCT Zone (MCTZ)** (Heim and Gansser 1939; Schelling and Arita 1991; Srivastava and Mitra 1994; DeCelles et al. 2002). The isolation of GHS from LHS by positioning the MCT in between, is done through different approaches in metamorphic petrology (Thakur et al., 2015; Spencer et al., 2012), structural criteria (Searle et al., 2008; Larson et al., 2017) and Nd-Sr isotopic compositions (Parrish & Hodges, 1996; Ahmad et al., 2000; Martin et al. 2005; Richards et al. 2005; Imayama and Arita, 2008). An inverted

Barrovian metamorphic sequence is notably observed through a part of LHS and GHS by superposing successive metamorphic zones from chlorite to sillimanite zone towards structural high (Le Fort, 1975; Arita, 1983; Vannay and Grasemann, 2001) and it accounts for an increase in metamorphic peak-T from ~ 500 °C in the LHCS to ~ 800 °C in the GHS (Célérier et al., 2009; Spencer et al., 2012; Thakur et al., 2015).

Southernmost unit, the **Sub-Himalaya**, represents the youngest thrust sheet of the orogeny consisted of mid-Miocene to Pliocene synorogenic sedimentary rocks of Siwalik group (DeCelles et al. 1998; Kumar et al. 2003; Najman et al. 2004; Ravikant et al. 2011). The Sub-Himalaya is separated from the LHS by middle to late Miocene **Main Boundary Thrust (MBT)** to the north (Heim and Gansser, 1939; Meigs et al., 1995; Mugnier et al., 1994) and from foreland basin sediments by the seismically active **Main Frontal thrust (MFT)** to the south (Gansser, 1964; Yeats and Lillie, 1991; Lavé and Avouac, 2000).

1.2. Evolution of metamorphic core of the mountain belt

There are three models explaining the emplacement of the Himalayan metamorphic core (the GHS rocks) between the LHS and the THS (Figure 1.1): wedge extrusion (e.g., Burchfiel and Royden, 1985; Grujic et al., 1996; Kohn, 2008), channel flow coupled to focused denudation (e.g., Beaumont et al., 2001; Hodges et al., 2001), and tectonic wedging (Webb et al., 2007; Yin, 2006). Wedge extrusion envisions the GHS as a northward-tapering wedge extruding to the south between the two lower grade sequences (Figure 1.2A). The South Tibet detachment kinematics may be driven by rotation of principal stresses along the topographic front that generates upper-crustal extension along the range crest (Burchfiel and Royden, 1985), or may represent adjustments to maintain critical taper if the range is modeled as a Coulomb wedge (e.g., Kohn, 2008; Robinson et al., 2006). In channel flow-focused denudation models, the GHS represents partially molten lower/middle crust in the thickened collision zone that tunnels southwards, driven by the gravitational potential of the high plateau (Figure 1.2B) (e.g., Beaumont et al., 2001, 2004; Godin et al., 2006a). This material channel is exhumed between active faults by erosion across a narrow zone where precipitation is focused by the orography of the topographic front (e.g., Beaumont et al., 2001; Hodges et al., 2001). The initiation of rapid exhumation and development of the paired

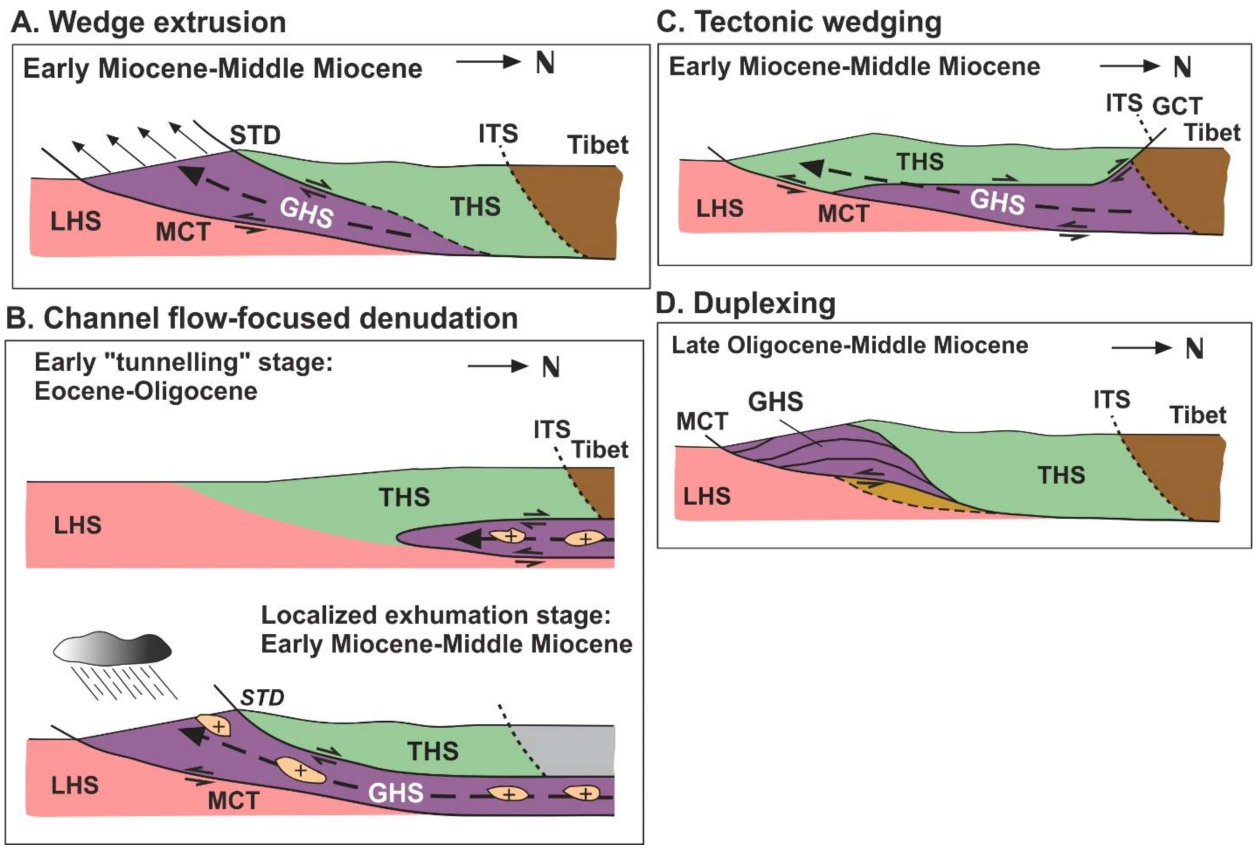

Figure 1.2. Tectonic models for the emplacement of the Greater Himalayan Sequence (GHS). (A) Wedge extrusion (e.g., Burchfiel and Royden, 1985). (B) Channel flow–focused denudation (e.g., Beaumont et al., 2001). (C) Tectonic wedging (e.g., Webb et al., 2007). (D) Duplexing process (e.g., Martin et al. 2010; Corrie and Kohn 2011; Webb et al. 2013).

channel flow-focused denudation system is speculated to result from a precipitation increase associated with a climatic shift (e.g., Beaumont et al., 2001; Clift et al., 2008; Hodges et al., 2001). In tectonic wedging models, top-north motion along the South Tibet detachment does not represent extension, but rather 10 s of kilometers of back thrusting in the Main Central thrust hanging wall (Figure 1.2C). The top-north displacement is kinematically linked to the north-directed Great Counter thrust system, which juxtaposes the THS rocks atop the Asian plate rocks and suture zone rocks to the north and was active in the Early–Middle Miocene (i.e., coeval with South Tibet detachment motion; Yin et al., 1999). This model was motivated by the discovery that the Main Central thrust and South Tibet detachment merge to the south in the western Himalaya, bounding the locally exposed leading edge of the GHS (Webb et al., 2007; Yin, 2006). Duplexing model suggests duplex development above a ramp in the sole thrust at mid-crust depth (Figure 1.2D) (e.g. DeCelles et al. 2001; Robinson et al. 2003; Bollinger et al. 2004, 2006; Bhattacharyya and Mitra 2009; Herman et al. 2010; Webb 2013).

1.3. Objective of this study

The Himalayas are the natural laboratory for understanding the metamorphic as well as the deformation processes of an active continent-continent collisional orogenic belt. The main purpose of being attached with the area around Mandakini and Madhmaheswarganga river valley is to do detailed microstructural analysis integrated with field mapping since there are no such previous works done in this area on microstructural aspects and metamorphic P-T evaluation. This work will contribute to connect two well explored area along Alaknanda valley in the east and Bhagirathi valley in the west. There are two key chapters, Chapter 4 and Chapter 5, which will address the fundamental aspects arising from the tectono-metamorphic processes experienced by the rocks of the Munsiari formation (MCTZ) and the Vaikrita formation (lower GHS). The aim of Chapter 5 is to study the inverted Barrovian sequence of metamorphic isograds, thereby explaining the metamorphic field gradient by means of phase relationship, mineral chemistry and peak metamorphic P-T results. The resolution of these aspects is of fundamental importance to the understanding of the tectonometamorphic evolution of the Himalayas. Further, it is crucial to deliberate over the possible mechanical and dynamic processes behind the existence of the metamorphic field gradient.

Purpose of the chapter 5 is inclined towards the understanding of deformation kinematics of the rocks within a continental scale shear zone known as Main Central Trust Zone (MCTZ). The major concern of the study is to elucidate the microstructural variation as a function of strain localization processes and other controlling factors. More specifically, quartzofeldspathic gneiss with mylonitic fabric were subjected to the EBSD analysis for explaining the deformational behavior of quartz grains in quartz rich domain as well as in polyphase domain of mylonites. Lattice preferred orientation (LPO) fabrics of quartz grains were obtained to observe the way how slip system activity of quartz grains and symmetry of CPO changes across the MCT. Furthermore, this research intends to quantify the CPO fabrics by means of eigenvectors of orientation data acquired from different domains of mylonites and to correlate the trend of change with different factors like strain intensification, effect of temperature , role of water content and presence of other associated mineral phases within a ductile shear zone.

Chapter 2

Geological framework of Garhwal-Kumaun Himalaya

2.1. Cenozoic Sub-Himalayan (SH) foreland belt

In Kumaun, Subhimalayan rocks (Figure 2.2) are composed of coarsening-upward, Neogene sedimentary rocks (~6.0 km thick; Najman, 2006; Ravikant et al., 2011) that were shed from the adjacent growing Himalayan thrust belt (DeCelles et al., 1998; Kumar et al., 2004). Within the Subhimalayan zone, the **Siwalik Group** is informally divided into lower, middle, and upper units (DeCelles et al., 1998, 2001, 2002). The **lower Siwalik unit**, deposited between 13 and 11 Ma (Kumar et al., 2004; Ravikant et al., 2011), is an ~1500-m-thick succession of alternating sandstone and mudstone. The **middle Siwalik unit**, deposited between 11 and 4.5 Ma (Kumar et al., 2004), is a >2300-m-thick, vertically and laterally stacked sandstone complex. The upper Siwalik unit, deposited between 4.5 and 1 Ma (Kumar et al., 2004), is a ~2300-m-thick succession of bedded conglomerate with lenticular bodies of sandstone and rare mudstone. Pre-Siwalik Group foreland basin units (e.g., Subathu/Bhainskati, Dagshai-Kasauli/Dumri Formations) crop out intermittently in the hanging wall and footwall of the Main Boundary thrust (Mukhopadhyay and Mishra, 2005; Robinson et al., 2006; Mishra and Mukhopadhyay, 2012). In eastern Kumaun, the lower Siwalik unit, as well as Neogene pre-Siwalik foreland basin strata (Lugad Gad Formation; Fig. 3B; Rupke, 1974), crop out between the Main Frontal thrust and Main Boundary thrust (Figure 2.2) in the Subhimalayan thrust system as three thrust sheets: the Main Frontal thrust sheet, an unnamed sheet, and the Main Dun thrust sheet. The Main Frontal thrust sheet is ~2900 m thick and contains a mudstone-sandstone sequence, including paleosols, of the lower Siwalik unit and the thickly bedded gray sandstone of the middle Siwalik unit. The basal part of the overlying Main Dun thrust sheet contains ~300 m of pale-green, biotite-rich sandstone of the Lugad Gad Formation (Rupke, 1974; Karunakaran and Rao, 1979), which is equivalent to the early Miocene Dumri Formation of western Nepal and Kasauli/upper Dharamsala Formation of Himachal Pradesh (Najman, 2006). Lugad Gad sandstone has prolifc paleosol horizons, ripples, and high biotite content, which are nearly absent in the overlying Siwalik sandstone. The Lugad Gad Formation is overlain by mudstone-dominated lower Siwalik Group rocks in the Main Dun thrust sheet (Mandal et al., 2019).

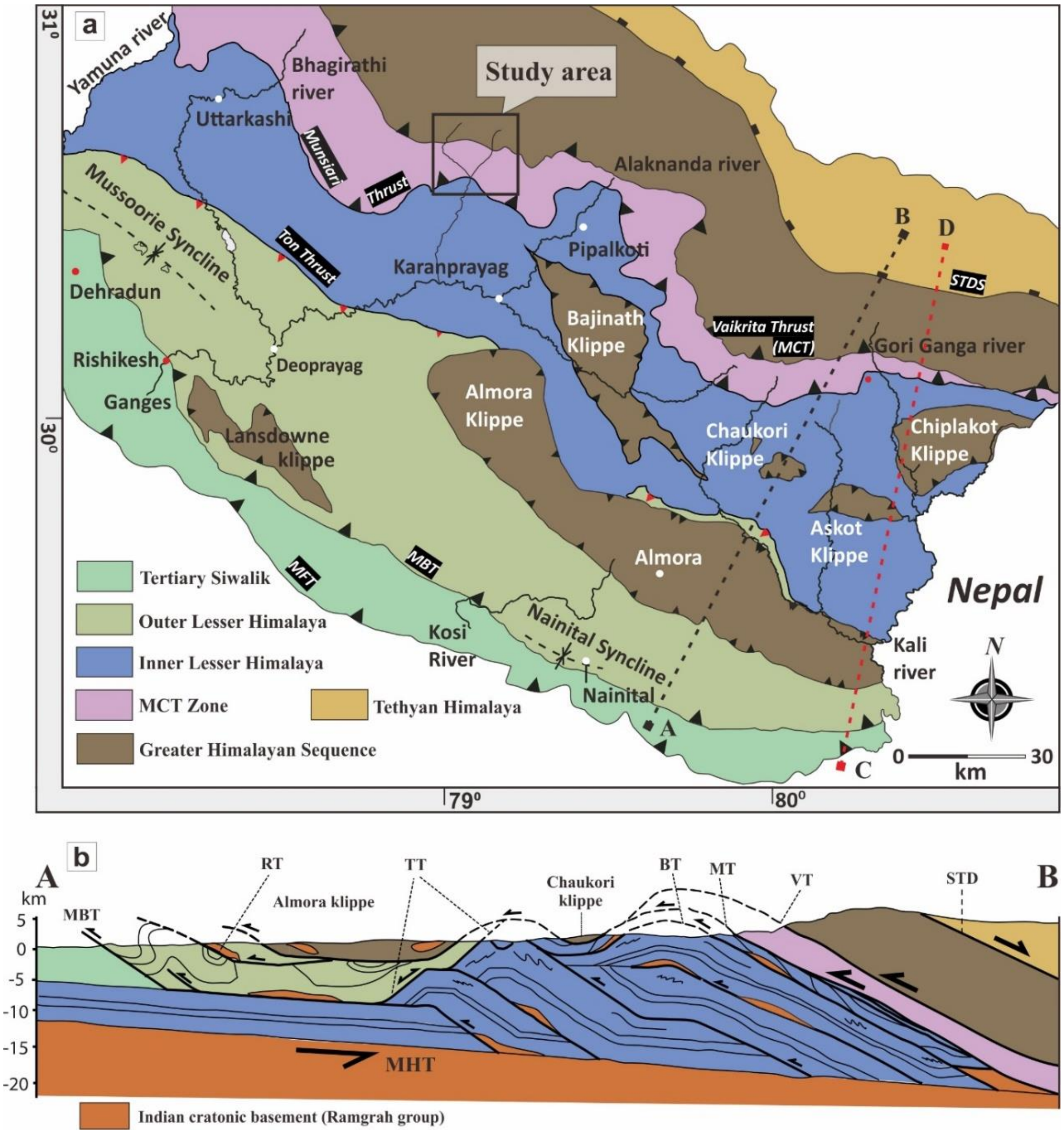

Figure 2.1. (a) Generalized geological map of Garhwal and Kumaun Himalaya with different tectonic units (after Célérier et al., 2009). The location of this part of the Himalaya is shown in Figure 1.1b. Black solid rectangle displays the study area shown in Figure 3.1a. Black dashed line (AB) is a section line for the cross section below. Red dashed line (CD) is drawn to produce a tectono-stratigraphy shown in Figure 2.2. (b) A schematic cross section through the Kumaun Himalaya (after Célérier et al., 2009). Thrust fault in the section are MBT- Main Boundary Thrust, RT- Ramgarh Thrust, TT- Tons Thrust, BT- Berinag Thrust, MT- Munsiari Thrust, VT- Vaikrita Thrust, STD- Southern Tibetan Detachment, MHT- Main Himalayan Thrust.

2.2. Lesser Himalaya

In India, the Lesser Himalayan sequence is composed of Paleoproterozoic to Cambrian igneous and metasedimentary rocks and is divided into two parts, Paleoproterozoic-Mesoproterozoic Lesser Himalayan rocks (1900-1600 Ma) and Neoproterozoic Lesser Himalayan rocks (1100-500

Ma), commonly referred as lower Lesser Himalaya and upper Lesser Himalaya, respectively (McKenzie et al., 2011; Mandal et al., 2016). Detailed descriptions of Lesser Himalayan rocks have been presented elsewhere (Valdiya, 1980; Srivastava and Mitra, 1994; Célérier et al., 2009; Mandal et al., 2015) and are summarized in Figure 2.2. Paleoproterozoic-Mesoproterozoic Lesser Himalayan rocks include the **Berinag-Munsiari** and **Rautgara Formations**, while Neoproterozoic–Cambrian Lesser Himalayan rocks include the **Mandhali**, **Chandpur**, **Nagthat**, **Blaini**, and **Krol Formations** (Figure 2.2). The age of the **Deoban Formation** is controversial, and proposed ages have ranged from latest Paleoproterozoic to latest Neoproterozoic (see discussion in Mandal et al., 2015). Because of lithologic similarity, and potentially overlapping ages, we group it with the **Mandhali Formation**. Basal Paleoproterozoic-Mesoproterozoic Lesser Himalayan rocks (i.e., greenschist- to lower-amphibolite-facies Berinag-Munsiari Formation) often crop out within the Lesser Himalayan tectono-stratigraphic zone as synclinal klippen, known as Lesser Himalayan Crystalline nappes/klippen (e.g., Askot and Chiplakot klippen). Paleoproterozoic-Mesoproterozoic Lesser Himalayan rocks have very negative whole-rock neodymium isotopic values (εNd = ~ -24.0; Ahmad et al., 2000; Robinson et al., 2001; Martin et al., 2005; Richards et al., 2005; Mandal et al., 2015; Martin, 2017), while Neoproterozoic–Cambrian Lesser Himalayan and Greater Himalayan rocks have less negative ε

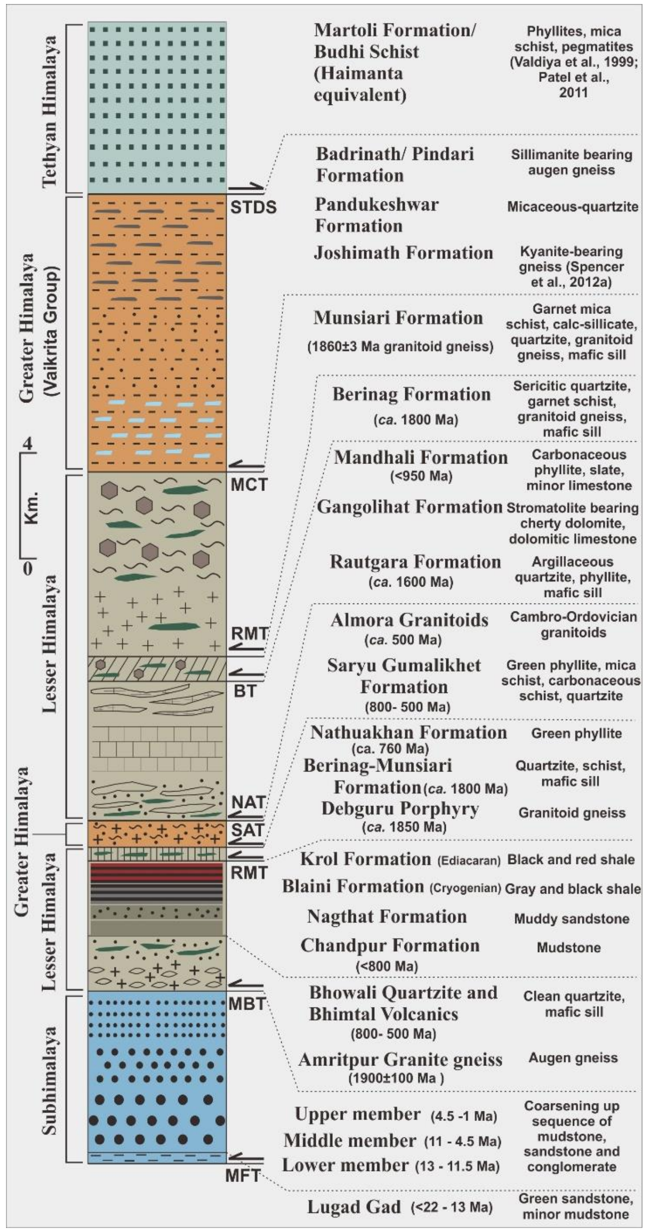

Figure 2.2. Generalized tectono-stratigraphy of the Kumaun Himalaya (after Mandal et al., 2019). MCT- Main Central Thrust, RMT- Ramgarh-Munsiari Thrust, BT- Berinag Thrust, NAT- North Almora Thrust, SAT- South Almora Thrust, MBT- Main Boundary Thrust, MFT- Main Frontal Thrust.

Nd values (~ -15.0; Ahmad et al., 2000; Robinson et al., 2001; Richards et al., 2005). Neoproterozoic-Cambrian Lesser, Greater, and Tethyan Himalayan rocks are difficult to distinguish using depositional ages and εNd values alone, because they may have been part of a single Neoproterozoic continental margin (Myrow et al., 2003, 2015; McKenzie et al., 2011). An intra-Lesser Himalayan thrust, known as the Tons thrust, is interpreted to separate Paleoproterozoic-Mesoproterozoic lower Lesser Himalayan rocks to the north from the Neoproterozoic-Cambrian Lesser Himalayan rocks to the south (Srivastava and Mitra, 1994; Richards et al., 2005; Célérier et al., 2009).

2.3. Greater Himalaya

Greater Himalayan rocks consist of Neoproterozoic–Ordovician metasedimentary and meta-igneous rocks (Parrish and Hodges, 1996; DeCelles et al., 2000; Yin, 2006; Gehrels et al., 2011), which are intruded by Miocene leucogranite (Visonà and Lombardo, 2002; Searle et al., 2010). Greater Himalayan rocks north of the Main Central thrust are upper-amphibolite- to granulite-facies metasedimentary and meta-igneous rocks (Figs. 4B and 4C), known as the **Vaikrita Group**, and they are divided from structurally low to high into the **Joshimath**, **Pandukeswar**, and **Badrinath Formations** (Spencer et al., 2012a, 2012b; Iaccarino et al., 2017). A single formation may consist of different thrust sheets (e.g., Corrie and Kohn, 2011), and the three formations may be separated by tectono-metamorphic discontinuities (Carosi et al., 2016). Temperatures and pressures are as high as ~800 °C and ~14 kbar in Greater Himalayan rocks north of the Main Central thrust in an ~500 km sector spanning central Nepal through Garhwal (Kohn, 2014). Medium- to high-grade metamorphic rocks of Greater Himalayan affnity (i.e., Neoproterozoic depositional ages and less negative Nd isotopic values) also crop out within the Almora klippe (Mandal et al., 2015) carried by the Almora thrust. Valdiya (1980) described these rocks as an allochthonous unit that originated from the upper-amphibolite- to granulite-facies Greater Himalayan metamorphic rocks to the north. The Almora klippe is composed of metasedimentary rocks and Cambrian–Ordovician (ca. 500 Ma) granitoids. These rocks show greenschist to upper-amphibolite facies structurally upward with temperatures from 500 °C to 700 °C and pressures of 4–8 kbar (Joshi and Tiwari, 2009; Rawat and Sharma, 2011); thus, these pressure-temperature conditions are lower than Greater Himalayan rocks north of the Main Central thrust.

Chapter 3

Geology of the study area

3.1. Introduction

The study area is located in Rudraprayag district of Uttarakhand in the Garhwal Himalaya (between 30°29´N, 78°59´E and 30°38´N, 79°13´E). The work is involved in the study of the lithology and structures exposed along three river valley traverse- (i) an orogen perpendicular section of Madhyamaheswar Ganga river valley, (ii) an orogen subparallel section of Mandakini river valley and (iii) Kalimath-Jalmalla road section gently inclined to the orogen axis (Figure 3.1a).

3.2. Geological setting

By following the work of Valdiya (1980) in the Garhwal Himalaya, it can be inferred that the study area is comprised of two major stratigraphic units. In the south, the formation known as Munsiari formation (LHCS) with the thickness of ~ 8 km thickness, is generally characterized by the existence of mylonitic granitic gneisses (Figure 3.2a & 3.6b, c) and garnet bearing metapellites (Figure 3.2b & 3.7i, k) with some intercalations metabasic rocks (Figure 3.2c & 3.6g, h), calc-silicates (Figure 3.2e & 3.6a), micaceous quartzite (Figure 3.6f) and marble (Figure 3.6e). This formation is considered to be the hanging wall block of the Munsiari thrust (MT). Generally, this formation represents a thick mylonitic zone identified by the presence of sigmoidal porphyroclast of feldspar (Figure 3.4b & 3.6b), stretched lenses of quartzofeldspathic domain (Figure 3.4a), C′-type shear band (Figure 3.4b) and isoclinal folds (Figure 3.5j). All these asymmetric structures indicate the effect of top-to-the-South sense of shearing. Deformational events of this formation can be interpreted through the observation of orogen-parallel and orogen-transverse folds and is discussed in the section 3.3. Presence of garnet (Figure 3.7k) and staurolite (Figure 3.7m) bearing metapellites delineates the garnet-in and staurolite-isograd of Barrovian metamorphic sequence.

In the north, overlying Vaikrita formation is composed of ~ 8 km thick strata of garnet-kyanite bearing migmatitic paragneiss (Figure 3.3a, c, d & 3.8a, b) which is in fact the lower part of the Greater Himalayan Sequence (L-GHS) associated with minor calc-silicate bodies (Figure 3.3b & 3.8c, d) and leucogranitic intrusives (Figure 3.8e). These two formations are separated by a structural discontinuity called as Main Central Thrust (MCT; locally known as Vaikrita thrust). Ductile shearing along the MCT, associated with emplacement of the Greater Himalayan

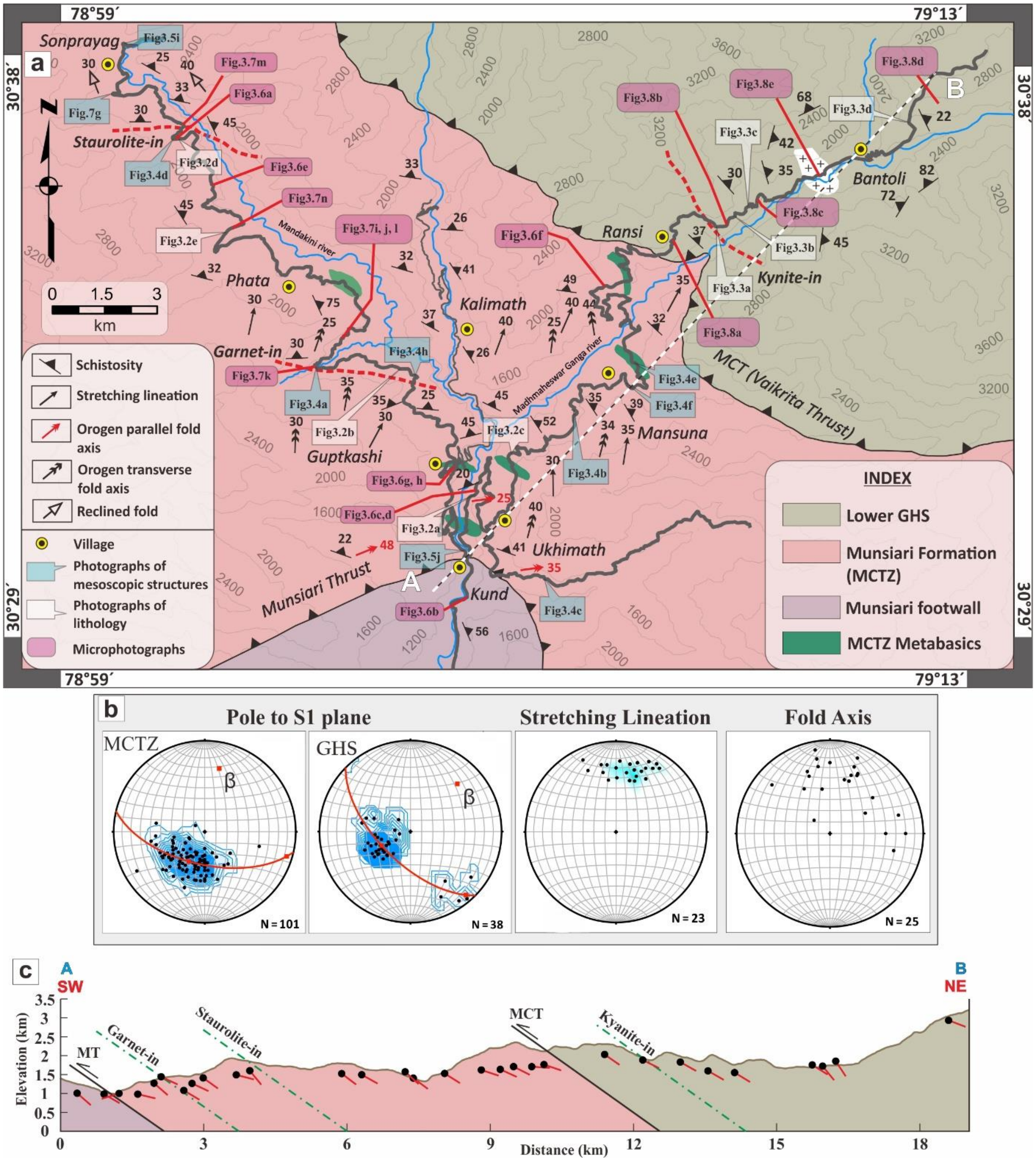

Figure 3.1. (a) Geological map of western Himalaya along Mandakini River and Madhmaheswar river valley, Uttarakhand, India. The location of the study area is marked in Figure 2.1a. Attitudes of schistosity, mineral stretching lineation and folds are shown using different symbols. The Locations of field photographs and microphotographs are shown using different colors. Dashed line AB represents the line along which the cross section profile of the study area is drawn. (b) Lower hemisphere equal area stereographic projection of the poles to the main foliation planes (S_m). Best fit great circles (red) are drawn to get the orientation of β-poles (fold axis of large scale regional fold). Orientation of the linear structures (lineation and fold axis) are also shown in lower hemisphere equal area projection. (c) Geological cross section of the study area along AB line. Apparent dip of main foliation (S_m) are shown along with the tectonic contacts and metamorphic isograds.

Sequence, is expressed by moderately dipping tectonic foliations (40°–60°) striking 090°–120°, and a prominent, gently plunging stretching lineation (20°–40°) trending 030°–050° (Figure 3.1a, b). Well-developed mineral stretching lineation especially defined by micaceous minerals, indicating the tectonic transport direction of the thrust sheet. A change in attitude of foliations is observed in the upper part of lower GHS (dipping 65°-80°, striking 010°–020°).

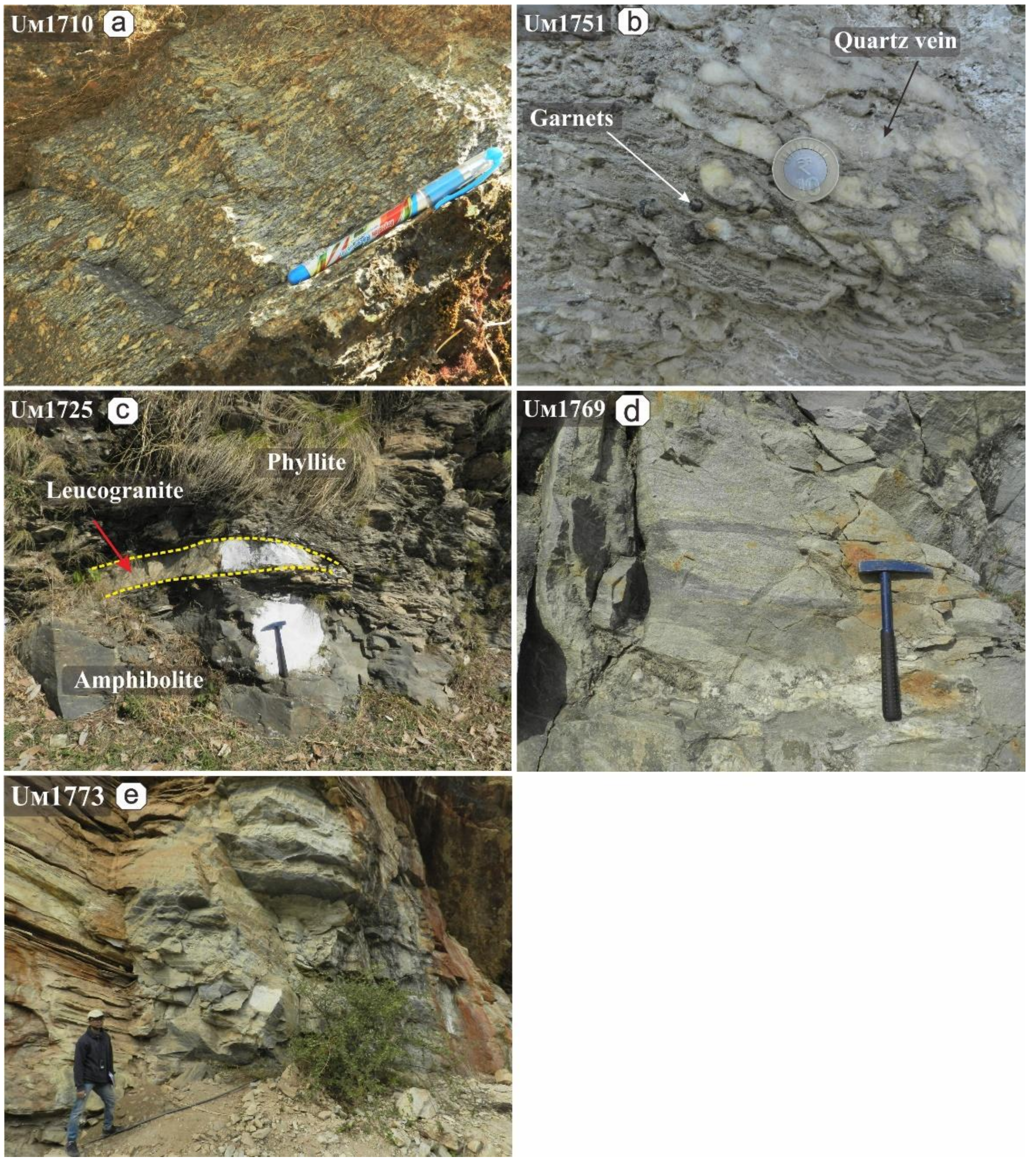

Figure 3.2. Representative field photographs showing lithological variation in the Munsiari formation (MCTZ). (a) Highly schistose augen gneiss with alternating layers of stretched quartzofeldspathic domain and micas. (b) Metapelitic schist showing the occurrence of large garnet porphyroblast. (c) Schistose leucogranitic layer within metabasic rock body and phyllite. (d) Migmatitic gneiss with leucosome (light colored) and melanosome (dark colored). (e) Calcsilicate rock body.

3.3. Mesoscopic Structures

Detailed fieldwork along the Mandakini and Madhmaheswar Ganga river section produced a new high resolution geological and structural map (Figure 3.1a). Our field study revealed several distinct tectono-stratigraphic and metamorphic units from chlorite-biotite grade to migmatite rocks through garnet-kyanite grade rocks, covering a distance of 45 and 30 km along E-W and

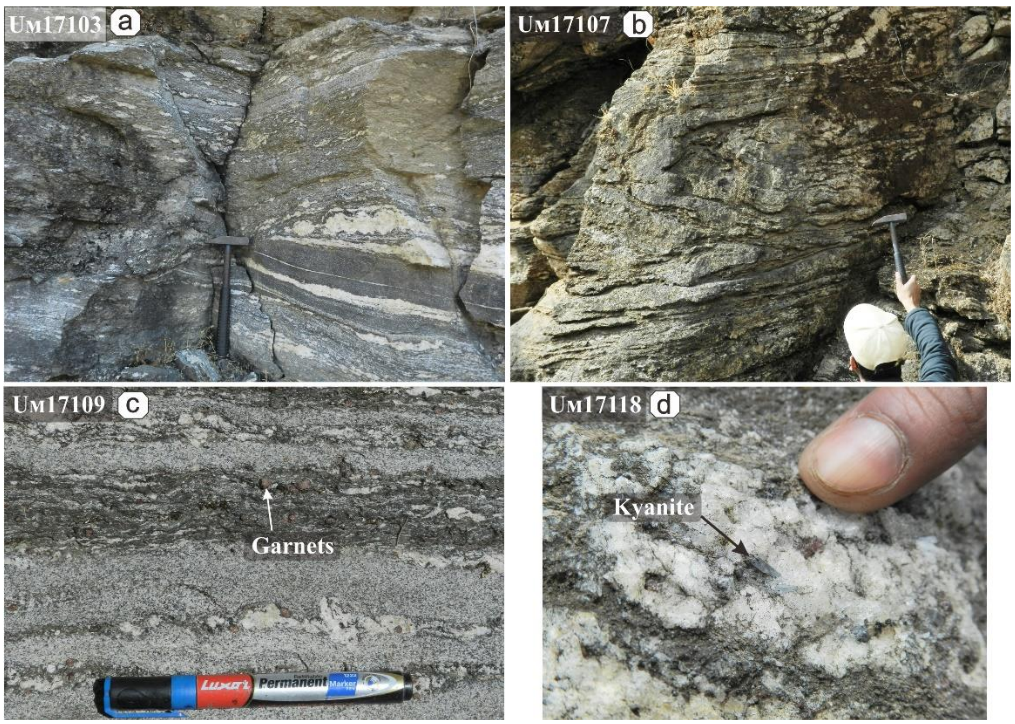

Figure 3.3. Representative field photographs showing lithological variation in the Vaikrita formation (L-GHS). (a) Migmatitic paragneiss characterized by higher mafic minerals and and stretched lenses of quartzofeldspathic fraction. (b) Folded calcsilicate body showing intense weathering effect ('elephant skin weathering'). (c) Large garnet porphyroblasts in the mafic rich layer of paragneiss. (d) Structurally higher most sample showing the presence of coarse kyanite blebs within quartzose layer of paragneiss.

N-S, respectively (Figure 3.1a). Our field investigation show that the dominant S1 foliation and the bedding (S0) plane, both are affected by the regionally occurring F2 recumbent folds, with broadly E-W trending fold axis (Figure 3.4e, f). Although, the bedding parallel S1 foliation is a common structural fabric, but associated F1 folds are practically absent in our study area. However, several earlier workers (Thakur and Choudhury, 1983; Kumar, 1997; Srivastava et al., 2011) identified the oldest F1 folds from different Himalayan sectors. The F2 folds were later co-axially refolded by the broadly E-W trending upright folds (F3) (Figure 3.4a, e). The F2 and F3 have events are consistent with the Himalayan shortening. Interestingly, the general orientation of planar fabrics strikes from NW-SE to E-W (Fig. 3.1a, b), while the linear fabrics like the stretching lineation shows broadly N-S orientation (Figure 3.1b). Such rotation of strikes conforms the presence of large-scale orogen perpendicular cross fold (F4) similar to the eastern Himalaya (Figure 3.4g) (Ghosh, 2017). In some places, the earlier F2 recumbent folds become reclined due to the superposition of the F4 folds. Such a diverse orientation of different generations of folds are predicted to form due to superimposition of orogen-parallel E-W and orogen-across N-S tending buckle folds (Bose et al., 2014; Ghosh, 2017).

3.4. Microstructures

An overall lithological variation and characteristic microstructures of the study area can be observed through the microphotographs (figure 3.6, 3.7 & 3.8). Mylonitic granitic gneiss is dominated by the presence of feldspar porphyroclast where fine grained matrix aggregates form a network of shear bands (Figure 3.6b). Metapelites contain large porphyroblast of snowball garnets with rotated trails of relatively fine grained inclusions merging to the main foliation (S_m) indicating syntectonic growth of garnets (Figure 3.7k, l). Orientation of micas and the microlithons of quartz-feldspar aggregate define a pervasive disjunctive foliation. Some garnet grew over the main foliation suggesting post-tectonic growth (Figure 3.7 j). In the sample 1755, relict of pre-existing foliation (S_{m-1}) can also be observed with an angular relationship to the main foliation. Quartz grains in the microlithons has irregular grain boundary formed by the effect grain boundary migration recrystallization (GBM).

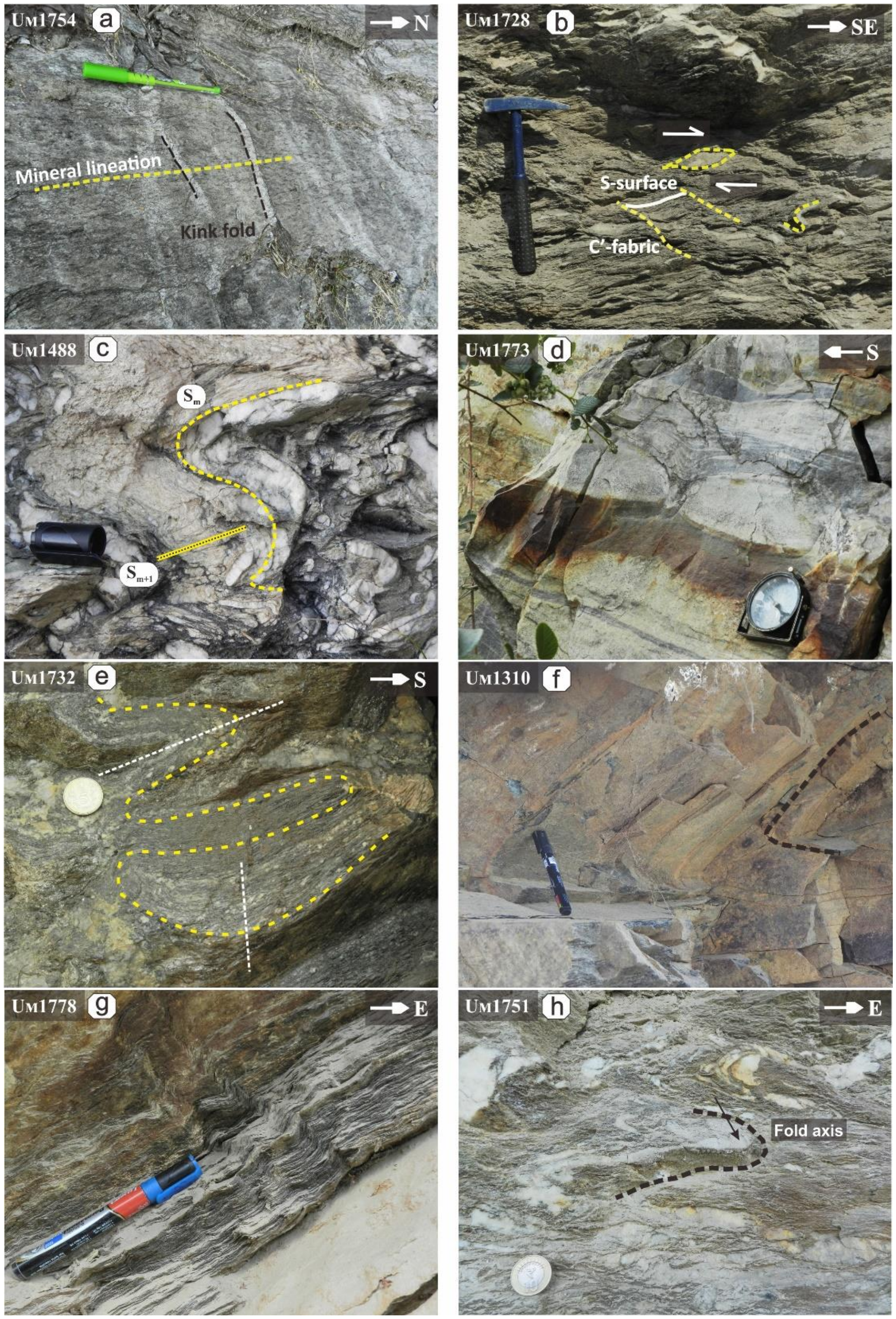

FIGURE 3.4. Representative mesoscopic structures present in the Munsiari formation (MCTZ). (a) Northerly plunging mineral stretching lineation orientated perpendicularly with orogen parallel easterly plunging kink fold (F_3). (b) S-C' fabric and asymmetric porphyroclast representing the transport of material with top-to-the-SE shear sense. (c) Outcrop of micaceous quartzite showing the presence of axial planar cleavage (S_{m+1}) in folded (F_2) main foliation (S_m). (d) Boudinage structure in quartzose layer embedded within calc-silicate layers. (e) Orogen parallel recumbent fold (F_2) in metapelitic schist. (f) Orogen parallel recumbent fold (F2) in calcsilicate rock. (g) Orogen transverse northerly plunging kink fold (F4). (h) Orogen transverse northerly plunging reclined fold of quartz vein (F_2).

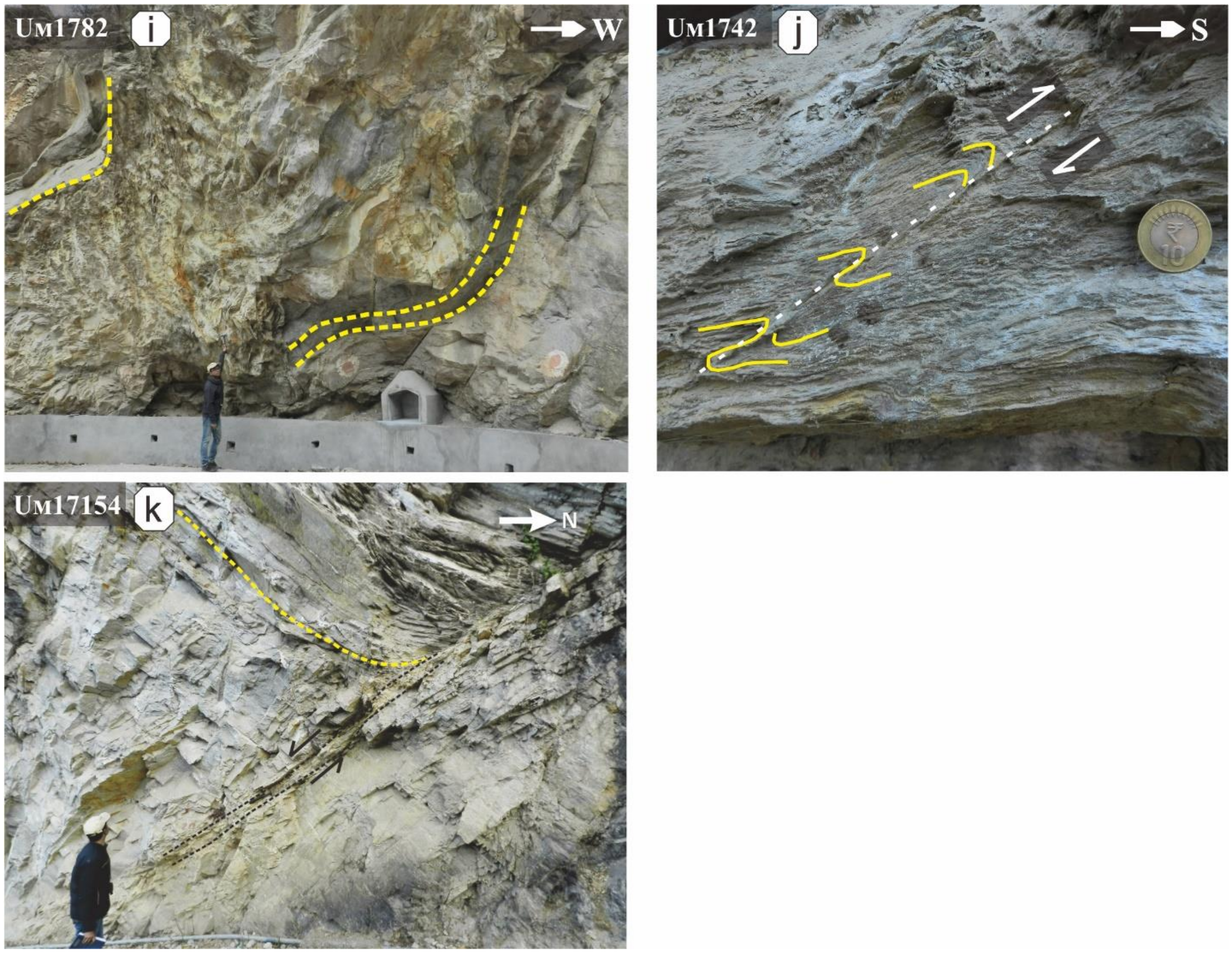

Figure 3.5. Representative mesoscopic structures present in the Munsiari formation (MCTZ). (i) Orogen transverse northerly plunging reclined fold (F_2) in granitic gneiss. (j) Small scale tight folds formed in metapelitic schist as a result of top-to-the-South sense of shearing. (k) Normal fault

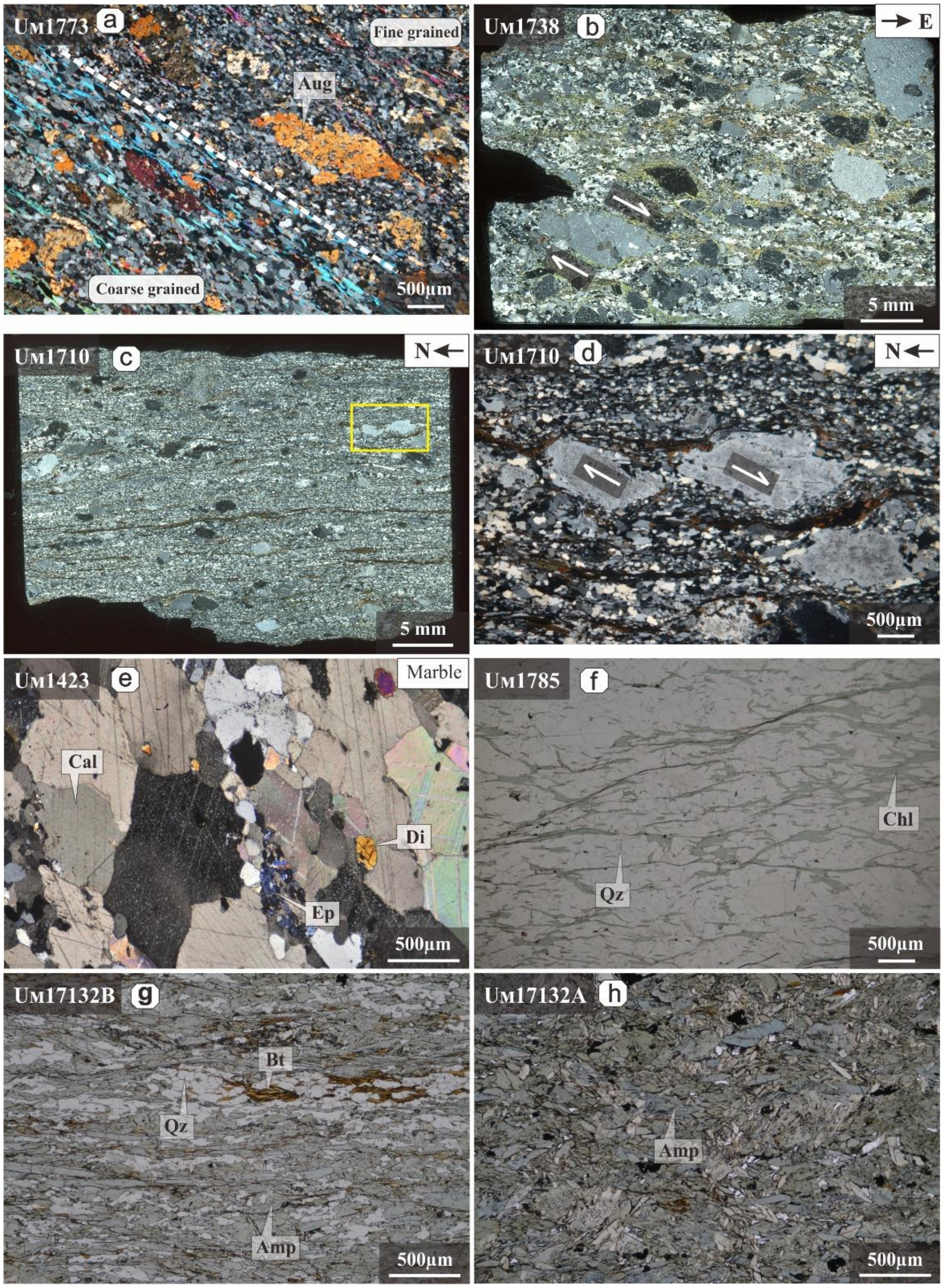

Figure 3.6. Representative microphotographs showing overall lithological variation and microstructures of the Munsiari formation (MCTZ). (a) Calcsilicate rock characterized by the presence of clinopyroxene; There is a sharp contact present in between coarse and fine grained fraction. (b) Mylonitic augen gneiss showing anastomosing spaced foliation; Sigmoidal porphyroclast of K-feldspar showing top-to-the-Southeast. (c) Highly schistose augen gneiss. (d) Microfaulting of K-feldspar porphyroclast represents the effect of top-to-the-Southwest shearing. (e) Coarse grained marble. (f) Schistose impure green quartzite with chlorite aggregates forming spaced foliation. (g) Foliated metabasic rocks with elongated amphiboles defining schistosity. (h) Massive metabasic rock with minor modal abundance of quartz and feldspar.

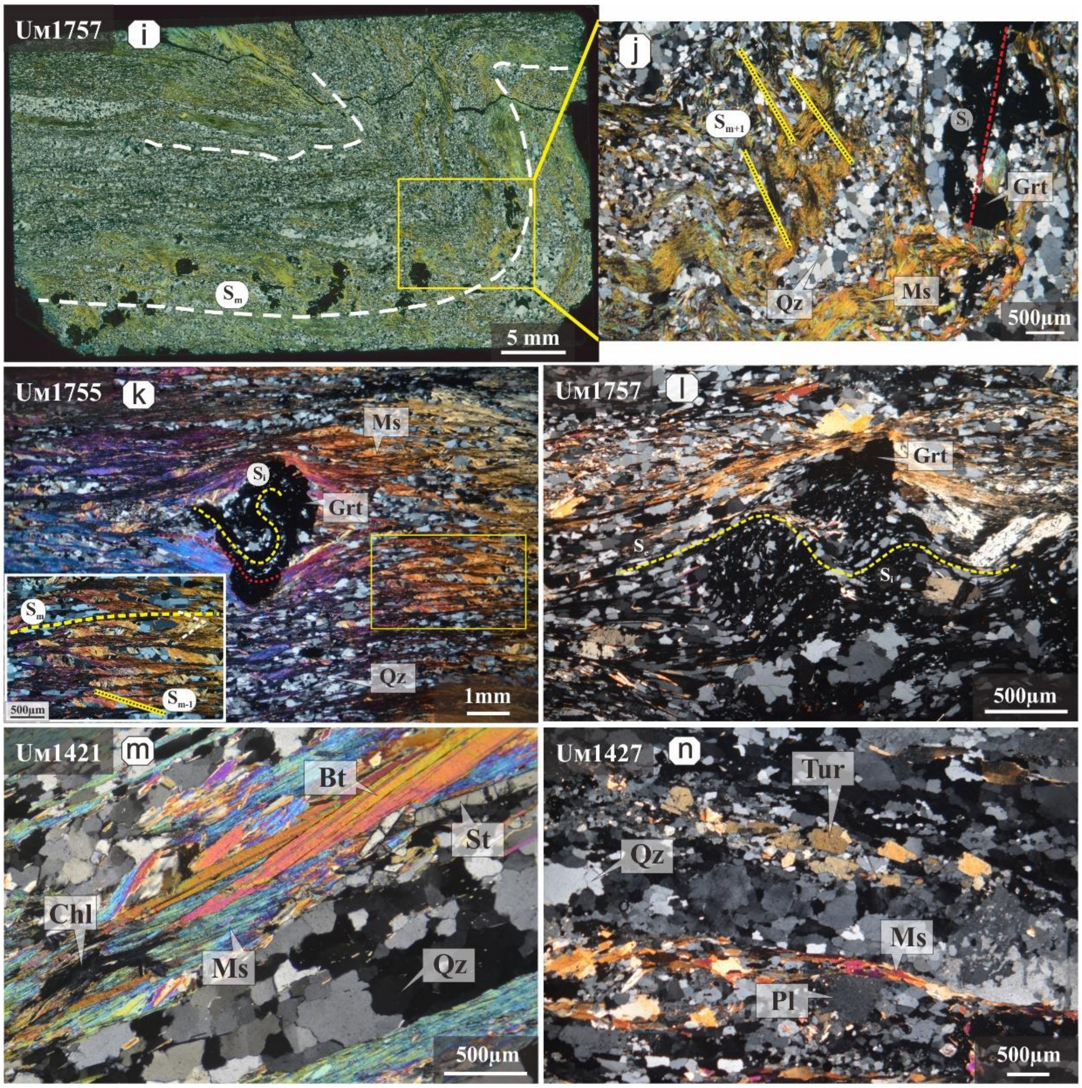

Figure 3.7. Representative microphotographs showing lithological variation and microstructures of the Munsiari formation (MCTZ). (i) Garnet bearing metapellite shows folding of main foliation (S_m) (b) Folding incorporates to the development of axial planar cleavage mostly defined by the mica layers; Internal foliation (S_i) within Garnet porphyroblast is concordant to the external foliation (S_e) indicates post-tectonic growth of garnet. (k) Snowball S_i pattern in garnet porphyroblast; Trace of pre-existing foliation (S_{m-1}) within microlithons (inset). (l) Syntectonic garnet porphyroblast. (m) Occurrence of acicular staurolite grains in metapelites. (n) Tourmaline bearing schistose leucogranite.

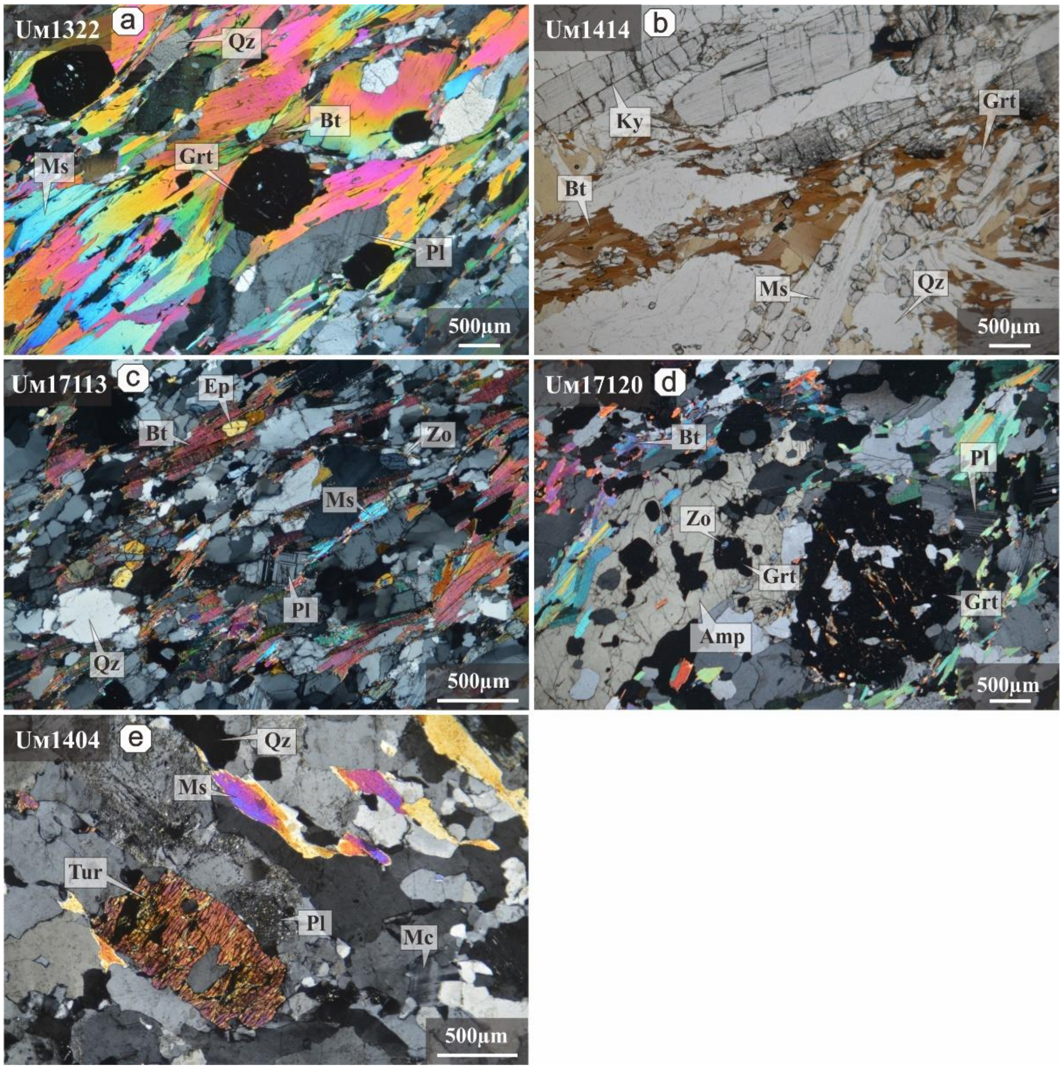

Figure 3.8. Microphotographs showing lithological variation and microstructures of the Vaikrita formation (L-GHS). (a) Garnet bearing coarse grained paragneiss. (b) Coarse bladed aggregate of kyanite in paragneiss. (c) & (d) Garnet bearing samples showing the occurrence of calc-silicate mineral such as epidote and zoisite. (e) Tourmaline bearing less deformed leucogranite.

Chapter 4

Tectono-thermal evolution of the MCT shear zone and lower Greater Himalayan Sequence and its implications

4.1. Introduction

The Himalayan range, extending for over 2400 km (Fig. 1), played a crucial role in strengthening our knowledge on the formation of mountains belts due to the collision of continental plates. The Himalaya formed as a result of the collision between the Indian and Eurasian plates (Gansser, 1964), initiating in the Paleocene (e.g., Zhuang et al., 2015) and continuing today (Bilham et al., 1997; Bettinelli et al., 2006). The subduction of the Indian plate in the NW Himalayas thickened the crust through the formation of the North Himalayan nappes at 50–40 Ma (e.g., Guillot et al., 2003; Epard and Steck, 2008). Barrovian metamorphism ensued in the middle crust during the late Eocene and early Oligocene (Steck, 2003; Chambers et al., 2009; Langille et al., 2012, 2014), while a fold and thrust belt, composed of passive Indian margin rocks within the Tethyan Sedimentary Series (TSS), formed in the upper crust (Searle et al., 1990; Steck et al., 1993; Wiesmayr and Grasemann, 2002). The formation of thickened crust, shear zones, and detachments during these early orogenic stages (e.g., Eocene and Oligocene), in many cases, exerted a strong control on the subsequent localization of midcrustal flow, partial melting, extrusion, and exhumation that characterized the Miocene (e.g., Steck, 2003)

The Main Central Thrust Zone (MCTZ) has long been recognized as one of the major terrane boundary shear zones of the Himalayan orogen that accommodated a significant amount of crustal shortening during Cenozoic time since the collision of the Indian with the Asian plate (Heim and Gansser 1939; Schelling and Arita 1991; Srivastava and Mitra 1994; DeCelles et al. 2002). Continental scale thrusting along this northward-dipping shear zone transported the medium- to high-grade Greater Himalayan Sequence (GHS) of Neoproterozoic to Cambrian age to the north over the Lesser Himalayan Sequence (LHS) of Palaeo- to Mesoproterozoic age to the south. Following Valdiya (1979, 1980) and Metcalfe (1993), the MCTZ in this study area of eastern Garhwal can be recognized as a package of sheared rocks bounded by the Munsiari Thrust (MCT of Heim and Gansser 1939 and Le Fort 1975; MCT I of Arita 1983; LMCT of Imayama et al. 2010) at the base and the Vaikrita Thrust (MCT II of Arita 1983; Vannay and Grasemann 1998; Caddick et al. 2007) at the top.

Over the entire Himalayan belt, this MCTZ is characterized by the existence of inverted Barrovian sequence with increasing metamorphic grade towards structural higher levels. In the western

Himalayas, the gradient is observed from chlorite through biotite to garnet zones in the Bhagirathi valley (Metcalfe, 1993) and in the progression of Garnet–staurolite–kyanite–sillimanite reported from the Sutlej valley (Vannay and Grasemann 1998, 2001; Caddick et al. 2007). There is a debate on the continuation of the gradient to the GHS. In the Sutlej valley, Vannay and Grasemann (1998) further established a second inverted metamorphic sequence that lies entirely within the HHCS. On the other hand, continuity of the inverted metamorphic sequence of the MCTZ into the GHS has been proposed in the Kishtwar window, where Stephenson et al. (2000) placed the garnet zone in the LHCS and staurolite and kyanite zones in the GHS. The problem of metamorphic continuity between the LHCS and GHS arises particularly where the uppermost part of the inverted metamorphic sequence of the MCTZ contains kyanite, which is a typical pelitic mineral throughout the GHS. However, in most regions, this pervasive kyanite developed in the GHS due to a pre-MCT phase of metamorphism (Metcalfe 1993; Stephenson et al. 2000). Furthermore, contrary to the common view that the metamorphism in the GHS is a Cenozoic phenomenon (Catlos et al. 2001; Martin et al. 2007), and several studies provide geochronological and/or petrological evidences of a pre-Himalayan medium-to-high-grade regional metamorphic imprint in the HHCS in different parts of the orogen, for example, in Pakistan (Treloar et al. 2000), Alaknanda valley (Argles et al. 1999), Sutlej valley (Marquer et al. 2000; Thakur and Patel 2012) and Nepal (Gehrels et al. 2003, 2006). The intermediate P ⁄ T-type metamorphism (kyanite zone) in the GHS has been recognized as the Eohimalayan (M1) stage in the Late Eocene–Oligocene (c. 38–32 Ma; Simpson et al., 2000; Godin et al., 2001). After this Barrovian-type metamorphism, high-T (mainly sillimanite zone) at medium- to low-pressure metamorphism caused the widespread anatexis in the Early–Middle Miocene, Neohimalayan stage (M2) at c. 26–18 Ma (e.g. Simpson et al., 2000; Daniel et al., 2003; Viskupic et al., 2005).

The study area is among those areas in Himalayas where a detailed metamorphic studies are still lacking. This study investigates the phase relationships, mineral chemistry and peak metamorphic conditions associated with the Munsiari formation (MCTZ) and L-GHS rocks in the Eastern

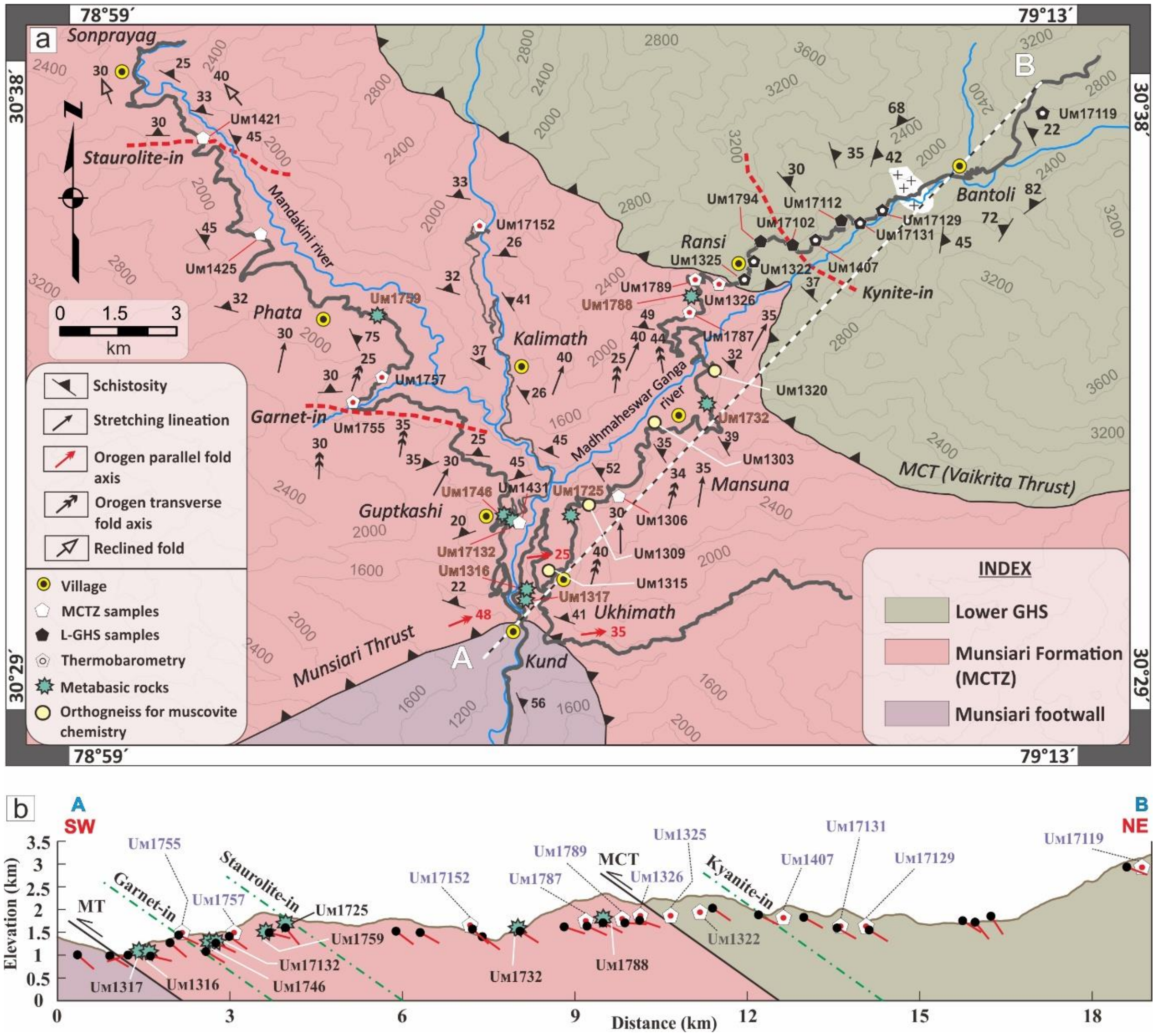

Figure 4.1. (a) Tectono-metamorphic map of the research area in the Western Himalaya. Samples for petrography and geochemical analysis are shown in the map; (b) The Simplified cross-section as illustrated along an orogen transverse line (A-B) is outlined by the sample locations and symbols representing apparent dip of general attitude of main foliation plane (Sm).

Garhwal region of India (Figure 4.1a) by combining structural field mapping and thermobarometry along the transects perpendicular to the strike of the orogen.

4.2. Sample description

The study area is comprised of medium to high grade of metamorphic rocks (greenschist to lower amphibolite facies) which are included in two stratigraphic formations. Munsiari formation, a footwall block of the MCT belonging to the MCTZ, mostly exhibits mylonitic orthogneiss, metapellites, calcsilicate rocks along with some disseminated bodies of schistose and massive metabasic rocks, marbles and schistose leucogranites. Foliated metabasic rocks are conformable with surrounding schistose rocks. Hanging wall block of the MCT called as Vaikrita formation belonging to the L-GHS mainly consists of migmatitic paragneiss associated with calcsilicate rocks and intrusives of leucogranites. For a detailed metamorphic studies, an emphasis was given on garnet bearing metapellites and garnet-kyanite bearing migmatitic paragneiss.

Petrographic studies were performed for 22 samples to determine the mineral assemblages of the study area and the microstructural relationships among the phases. Sampling has been done from three sections in the study area: Madhmaheswar Ganga river valley and Mandakini river valley. The majority of samples were taken from an orogen transverse road section along Madhmaheswar Ganga River valley. Twelve samples of garnet bearing schists and gneisses were selected for the thermobarometric analysis. In order to understand the *P-T* conditions of studied metamorphic rocks, Six samples of garnet bearing metapellites from Munsiari formation (LHCS) and another six samples of garnet-kyanite bearing paragneiss (coarse grained) from lower GHS were chosen. In addition, nine metabasic rocks belonging to the MCTZ was also subjected to evaluate the metamorphic conditions in contrast to that of pelitic and gneissic suits of rocks.

4.3. Methodology

Thin sections were prepared by cutting the samples along the plane which is parallel to the dip direction and perpendicular to the foliation. Final stages of polishing of thin sections were done by using 3 and 1 mm diamond paste to make the samples suitable for geochemical analysis. Samples were firstly examined using optical microscope for identifying the mineral phases along with the microstructural characterization. Mineral abbreviations used in the text and the figures were taken after Whitney and Evans (2010).

4.3.1. Geochemical studies

Preliminary approach

After deciding the domains by optical microscopy, JEOL JSM-5310 scanning electron microscope (SEM) at Hokkaido University was used with the help of an Oxford Energy 200 with LINK ISIS system. 15 kV accelerating voltage and 1 nA beam current was selected for the analysis. Semiquantitative electron-dispersive spectroscopy (EDS) analysis was carried out to obtain an overall idea of chemical heterogeneity, thereby knowing the equilibrium mineral assemblages. In particular, the importance has been given to identify the retrograde rim of garnet, inclusion phases within garnet porphyroblast and some other major and accessory mineral phases of matrix. Back scatter electron (BSE) images were taken to exhibit the mineral assemblages and textural relationships distinctly. Therefore, this method assisted to select the areas of interest for detailed quantitative analysis.

Quantitative analysis - Mineral chemistry

Mineral compositions for thermobarometric analysis were acquired from Electron probe micro-analyzer (EPMA) installed at three different laboratories. Major geochemical analysis was carried out at Hokkaido University, Sapporo with JEOL-8800R EPMA, accompanied by some more analysis using CAMECA SXFive EPMA at DST-SERB National Facility, Department of Geology, Banaras Hindu University, Varanasi and JEOL JXA-8230 EPMA at Okayama University of Science, Okayama. At Hokkaido University, the applied acceleration voltage and beam current for spot analysis were 15 kV and 20 nA with beam size of 1 µm for garnet, plagioclase, chloritoid, ilmenite and amphiboles. We had to reduce the beam current (12 nA) and increase the beam size (5-10 µm) for mica group of minerals. It took ~3 min to complete each point analysis. The calibration was done using natural mineral standards including orthoclase (for K and Si), jadeite (Na), wollastonite (Ca), periclase (Mg), hematite (Fe), corundum (Al), rhodonite (Mn) and chromite (Cr). Wavelength-dispersive spectrometers with TAP (Mg, Na, Al, Si), LIFH (Mn, Fe, Ni) and PET (Ca, K, Ti, Cr) crystals were deployed for the quantification. The intermediate phase of experimental work was carried out on the Electron Probe Micro Analyzer (EPMA) CAMECA SXFive instrument at DST-SERB National Facility, Deparment of Geology (Center of Advanced Study), Insititue of Science, Banaras Hindu University. Polished thin section were coated with 20 nm thin layer of carbon for electron probe micro analyses using LEICA-EM ACE200 instrument. The CAMECA SXFive instrument was operated by SXFive Software at a voltage of 15 kV and current 10, 12, 30 and 100 nA with a LaB6 source in the electron gun for generation of electron beam. Natural silicate mineral andardite as internal standard used to verify positions of crystals (SP1-TAP/LiF, SP2-LiF/PC3, SP3-LPET, SP4-TAP and SP5-PET) with respect to corresponding wavelenght dispersive (WD) spectrometers (SP#) in CAMECA SX-Five instrument. The following X-ray lines were used in the analyses: Na-*Kα*, Mg-*Kα*, Al-*Kα*, Si-*Kα*, P-*Kα*, K-*Kα*, Ca-*Kα*, Ti-*Kα*, Cr-*Kα*, Mn-*Kα*, Fe-*Kα* and Ni-*Kα*. Natural mineral standards: albite, halite, periclase, peridote, corundum, wollastonite, apatite orthoclase, rutile, chromite, rhodonite, and hematite; pure metal standard: Be and Ni supplied by CAMECA-AMETEK used for routine calibration, X-ray elemental mapping and quantification. Routine calibration, acquisition, quantification and data processing were carried out using SxSAB version 6.1 and SX-Results softwares of CAMECA. The operating conditions of quantitative spot analysis using JEOL JXA-8230 EPMA at Okayama University of Science, Okayama are 15 kV accelerating voltage, and 12 nA beam current for all mineral phases. The operating conditions of garnet element mapping are 15 kV accelerating voltage, 25 nA beam current, and 100 msec/spot measurement time. 1 µm beam size was used. The calibration was done using natural and synthetic mineral standards including K-Ti-phosphate (for K), albite (Na), wollastonite (Ca,Si), periclase (Mg), hematite (Fe), kyanite (Al), pyrophanite (Mn), Eskolaite (Cr) and Rutile (Ti). All garnet elemental maps were produced for the element of Mn, Mg, Fe and Ca. All analyses were corrected using conventional ZAF method. Mineral structural formulae recalculation has been done by following the instruction of John Brady, Smith College provided on the website of SERC, Carleton College.

4.3.2. Thermobarometric investigations

Thermobarometers

Individual thermobarometer as well as internally consistent thermodynamic database based average P-T estimation method were employed to obtain peak metamorphic temperatures and corresponding pressures. Primarily, garnet-biotite (GB) Fe-Mg exchange thermometer using Holdaway (2000) calibration was applied for all samples except one sample without biotite (UM17152). Temperature was estimated by assuming that all iron is divalent. Results are also obtained for Fe^{3+} by following Holdaway (2000) where it was suggested that 3 mol.% of total iron in garnet and 11.6 mol.% of that in biotite were in Fe^{3+} state. For the sample without biotite, garnet-ilmenite Fe-Mg exchange thermometer (Martin et al., 2009) was used. In addition, some other alternative thermometers were also used to compare the results obtained from garnet-biotite exchange thermometers. Ti-in-biotite thermometer of Henry et al. (2005) (lower MCTZ samples; UM1755 & UM1757) and Ti-in-muscovite thermometer of Wu & Chen (2015) (structurally higher most sample in L-GHS; UM17129) were applied. Absolute error for Holdaway (2000) calibration was estimated as ± 25°C whereas Martin et al., (2009) estimated relative error as ± 35°C. Precision of the Ti-in-biotite geothermometer is estimated to be ±24 °C at the lower temperature range and improves to ±12 °C at higher temperatures. The random error of this thermometer is estimated to be of ±65 °C. A revised Garnet-biotite-muscovite-plagioclase (GBMP) barometer of Wu, 2015 was considered to be effective for determining metamorphic pressures for all samples. We used garnet-biotite-Al_2SiO_5-quartz (GBAQ) barometer calibrated by Wu (2017) for two structurally higher most samples with kyanite (UM17129 & UM17119). The total error of the GBMP barometer was evaluated to be about ±1.2 kbar whereas the random error of the GBAQ geobarometer was determined to be around ±1.8 kbar.

Lastly, the average P-T method guided by a thermobarometric software THERMOCALC 3.33, with the updated Holland and Powell [1998] data set (tc-ds55. txt), was also used to determine peak metamorphic condition from the thermodynamic data [Powell and Holland, 1994]. Furthermore, amphibole-plagioclase thermometer of Holland & Blundy (1994) and a revised barometric calibration of Molina et al., (2015) were applied for metabasic rocks. Two garnet-amphibole bearing gneiss belonging to L-GHS and one from the MCTZ were found to be used for hornblende-garnet thermometer of Ravna (2000).

Analytical strategies to select mineral phases and locations for EPMA analysis

For the case of MCTZ garnets with growth zoning unaffected by retrograde reaction, nearest rim composition of garnets were taken into consideration along with the compositions of biotite, muscovite and plagioclase as close to the garnet as possible. Caution must be taken on the basis of textural observations to avoid the rim composition affected by retrograde net transfer reaction. In order to minimize the effect of retrograde reaction, the compositions of biotite, muscovite and plagioclase are selected to be distal to the garnet grain with retrograde rim. On the other hand, L-GHS garnets are characterized by flat diffusional zoning profile with retrograde rim. In this situation, for estimating peak metamorphic condition, core composition with minimum X_{Fe} (= Fe/Fe+Mg) were used in addition to the composition of equilibrium matrix phases distal to the garnet crystal. However, in the case of garnets with flat zoning profile, it is also essential to consider the large garnets to avoid the probability of resetting of core compositions during retrograde reactions. On account of this problem, Martin et al., (2009) suggested the minimum diameter of 700 μm for garnet crystals to reduce the changes of garnet composition during cooling process. Minimum size of the garnets used in this study is 927 μm. We used the composition of ilmenite inclusions from near rim part of garnet for garnet-ilmenite thermometer. On account of determining *P-T* condition of initial stage of garnet growth, we took the composition of ilmenite inclusion from garnet core for only two samples (UM1787 & UM1789). One sample (UM1326) was taken with ilmenite inclusion at middle part of garnet to get an idea about *P-T* condition of intermediate phase of garnet growth history.

4.4. Microstructural observations and phase relations

Representative samples for the petrographic analysis are described here in an order from lower to higher structural levels. Petrographic studies were carried out through the MCTZ rocks including garnet bearing metapellites (UM1755, UM1757, UM17152, UM1787 and UM1326), staurolite bearing schist (UM1421), Marble (UM1432 and UM1425) and mylonitic orthogneiss (UM1306) (Figure 4.2 and 4.3). On the other hand, L-GHS samples include garnet-bearing gneiss (UM1325), kyanite-bearing gneiss (UM17102, UM17129 and UM17119) and calc-gneiss (UM1794 and UM17112) (Figure 4.4). In particular, this section illustrates what we observed through the optical microscopy and SEM-EDS analysis. The mineral assemblages are presented in the Table 4-1.

4.4.1. Munsiari formation (MCTZ) samples

Metapellites

Sample UM1755: assemblage of grt-chl-bt-ms-qz-ilm-tur-ep-aln-ap

This is a garnet bearing sample collected from structurally lowest part of the MCTZ (Figure 4.2a and b). Therefore, it delineates the garnet-in isograd in the study area. The garnet-in reaction is considered as follows.

chlorite + muscovite + plagioclase + quartz = grt + biotite + H2O (1)

Generally, it is a fine grained rock with coarse grained garnet porphyroblasts (~ 3mm in diameter).

These garnets are associated with the matrix phases such as biotite, muscovite, quartz, ilmenite and accessory tourmaline, apatite, epidote and allanite. Shape preferred orientation of muscovite, biotite and ilmenite define the main foliation (S_m) of this sample. This type of foliation can be classified as a disjunctive foliation where closely spaced microlithons are dominated by quartz grains. Microlithons are also occupied by obliquely oriented mica flakes which are thought to be a remnant of earlier foliation (S_{m-1}). Whereas, some fractions of older foliation (S_{m-1}) are folded (Figure 3.7k). Plagioclase is absent in this sample. Chlorites are found as a retrograde product near garnet rim and along some biotite flakes (Figure 4.2d). Inclusion phases in garnet include quartz, ilmenite, muscovite, apatite, epidote, allanite and cordierite. Sinusoidal inclusion trail (S_i) are mostly defined by stretched ilmenite and quartz. The garnet porphyroblasts are warped by the main foliation (S_m), which is discontinuous with the internal foliation (S_i). Hence, it could be interpreted as an intertectonic porphyroblasts since garnets overgrew the earlier foliation, but truncated by the external foliation (S_e, Passchier & Trouw, 2005).

Sample UM1757: assemblage of grt-chl-cld-bt-ms-pl-qz-ilm-aln

This sample is a medium-grained pelitic schist comprised of muscovite, chlorite, chloritoid, plagioclase, biotite and quartz (Figure 4.2c and d). Main foliation (S_m) is mostly defined by the shape preferred orientation of muscovite, chlorite and minor amount of biotite and ilmenite. Chloritoid laths are also orientated parallel to S_m. These foliation planes are generally segregated by discontinuous quartzo-feldspathic domains constructing anastomosing disjunctive foliation networks. Garnet porphyoroblasts upto 1mm in diameter are wrapped by S_m. Concordant relationship between S_i and S_m could suggest syntectectonic growth history. Resorption of garnet occurred along the fracture by producing muscovite and quartz (Figure 4.2c). Some retrograde chloritoid oriented oblique to S_m, are present along the rim and fracture of garnet porphyroblasts (Figure 4.2c). Late stage chlorite flakes are found along with biotite flakes whereas some are found to be oblique to S_m. Late generation phases also include coarse muscovite grains grown at the expense of quartzo-feldspathic fraction (Figure 4.2d). Presence of prograde (2) and retrograde (3, 4) chloritoid can be explained by the following reactions (Spear, 1993).

Fe-chlorite + muscovite = Fe-chloritoid+annite+quartz+H_2O (2)

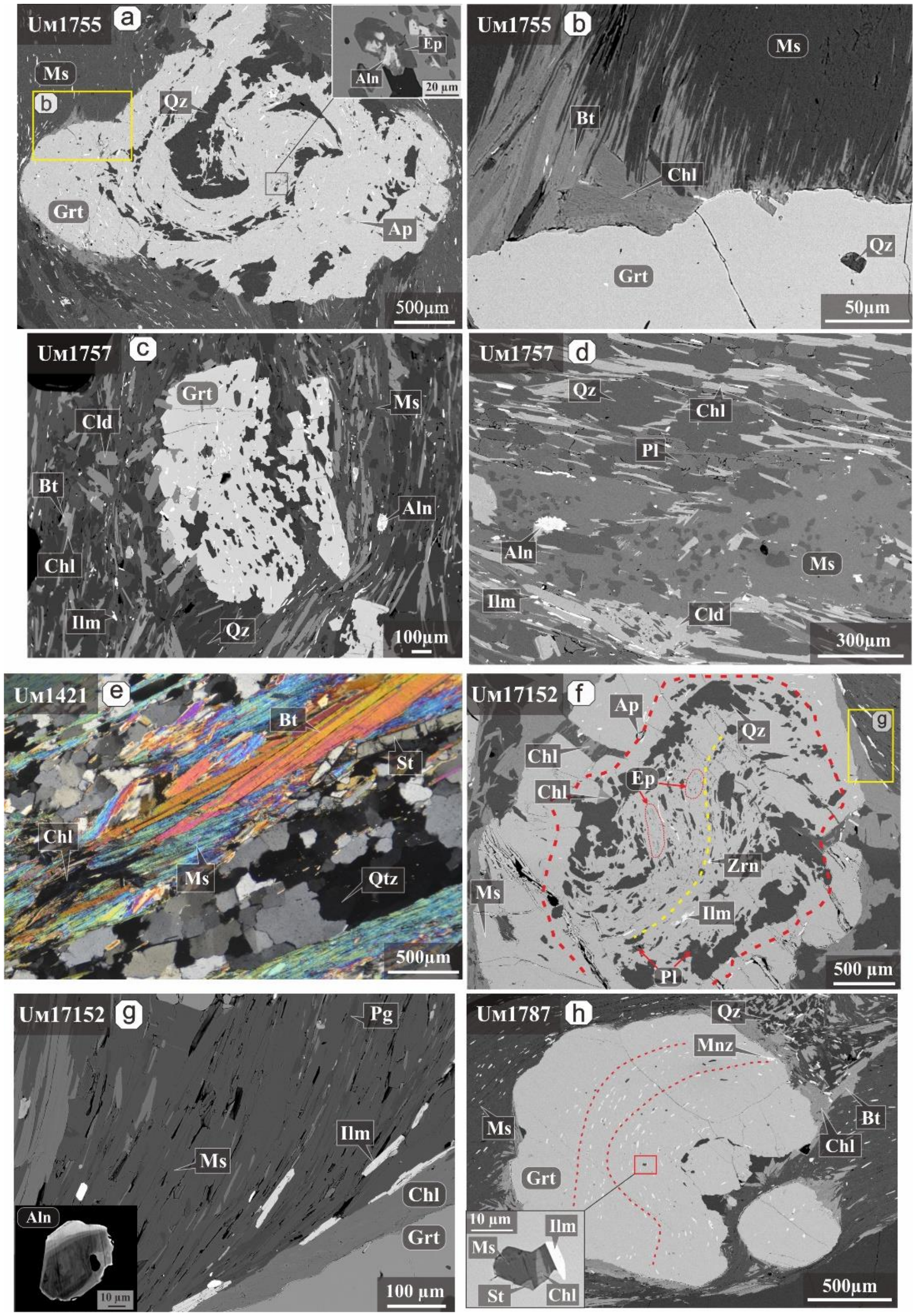

Figure 4.2. Representative microstructures of the metamorphic rocks from the Munsiari formation (MCTZ). (a) BSE image showing spiral inclusion trails in garnet porphyroblast wrapped by the main foliation defined by muscovite and ilmenite. Inclusions of epidote and alanite are shown in the inset. (b) Replacement of garnet and biotite by chlorite as a result of retrograde reaction. (c) Garnet porphyroblast is embedded in the matrix phases composed of muscovite-biotite-chloritoid-chlorite-ilmenite. (d) Porphyroblast of muscovite surrounded by chloritoid-chlorite-plagioclase-ilmenite. (e) Elongated staurolite aligned with biotite. (f) Garnet porphyroblasts with sinusoidal inclusion trails formed by ilmenite, quartz, epidote and minor plagioclase. Garnet rim is inclusion free and completely surrounded by chlorite. (g) BSE image showing the presence muscovite and paragonite in the main foliation. The inset shows zoned matrix allanite. (h) Spiral inclusion trails in garnet porphyroblast, defined by the orientation of ilmenite. The inset shows composite inclusion comprised of staurolite-muscovite-chlorite-ilmenite.

chloritoid ↔ garnet + chlorite + staurolite + H_2O (3)

chloritoid + biotite + H_2O ↔ garnet + chlorite (4)

Sample UM1421: assemblage of bt-st-chl-ms- pl-qz-ilm

This sample represents staurolite-in isograd in the study area (Figure 4.2e). The sample is medium-grained, which primarily consists of biotite, muscovite, plagioclase, quartz, chlorite alongwith minor staurolite and ilmenite. The main foliation (S_m) is defined by the alignment of coarse-grained muscovite and biotite. Continuous coarse-grained quartzo-feldspathic domain produces well-developed disjunctive foliation. Minor allanite is sparsely distributed in the matrix. The association of staurolite and biotite within S_m could be explained by assuming the following reactions (5, 6).

garnet + chlorite = staurolite + biotite + H_2O (KFMASH system) (5)

chlotite + muscovite + quartz = staurolite + biotite + H_2O (6)

Sample UM17152: assemblage of grt-chl-ms-pg-pl-qz-ilm-tur-ep-aln-ap

This sample collected from middle part of the MCTZ, is a medium-grained metapelitic schist comprising porphyroblasts of garnet, which are surrounded by a spaced foliation defined by muscovite and chlorite and a matrix of quartz, plagioclase, ilmenite, apatite and zircon (Figure 4.2f and g). Biotite is absent in the matrix. BSE image is showing the presence of lamellae of paragonite within the layers of muscovite (Figure 4.2g). Garnet porphyroblast are highly euhedral in shape with up to 2.5 mm in diameter. These crystals exhibit inclusion-rich core surrounded by inclusion-poor mantle. Inclusion phases are comprised of quartz, plagioclase, chlorite, ilmenite, epidote, zircon and apatite. The core preserves the sinusoidal inclusion trails pertaining to the earlier foliation (S_i) which indicates intertectonic growth history of garnet, because the S_i is truncated by the S_m. Late stage chlorite partially replaces the edges of garnet. Allanite grains in the matrix show chemical zoning (Figure 4.2g).

Sample UM1787: assemblage of grt-chl-bt-ms-qz-ilm

This is coarse-grained metapellites with widely spaced foliation defined solely by muscovite

(Figure 4.2h). Garnet porphyroblasts (upto 1.5mm in diameter) are embedded within the muscovite layers and surrounded by biotite. Biotite is present along the edges of garnet as well as discrete flakes within the strain shadow around garnet and the main foliation domain. Chlorite forms as a result of late stage retrograde process. Plagioclase is rare in this sample. Spiral pattern of ilmenite inclusions as an internal foliation (S_i) within garnet is continuous to the external foliation which suggests syntectonic growth of garnet. Garnet also contains a composite inclusion made up of polymineralic mineral phases showing assemblage of muscovite, chlorite, ilmenite and staurolite. Inclusions of cordierite and monazite are present in the garnet.

Sample UM1326: assemblage of grt-chl-ms- pl-qz-ilm-tur

This rock represents the metamorphic signature of the structurally highest part in the MCTZ (Figure 4.3i). It is a fine grained rock with relatively higher modal abundance of quartz. A continuous foliation (S_m) is developed by the presence of biotite-muscovite flakes and fibrous chlorite. Plagioclase is less abundant in the matrix. Garnet porphyroblasts are relatively smaller with up to 0.4 mm in diameter. Inclusions of quartz define the internal foliation (S_i) which is not continuous with S_m. Thus, the garnet porphyroblasts could be interpreted as intertectonic porphyroblasts. Minor amount of tourmaline is present in the matrix.

Mylonitic orthogneiss

Sample UM1306: assemblage of qz-pl-bt-ep with fsp porphyroclasts, myrmekites and oxides

This sample is a medium to coarse grained augen orthogneiss exhibiting well-developed foliation defined mostly by the alignment of biotite (Figure 4.3j and k). The sample includes quartz, plagioclase, K-feldspar, biotite, epidote along with accessory Fe-oxides. Majority of porphyroclasts are dominated by K-feldspar with albite lamellae (perthitic texture) and Carlsbad twinning. Plagioclase phenocrysts containin muscovite formed by sericitization process. Leucocratic part of matrix is primarily composed of quartz showing the signature of dynamic recrystallization by subgrain rotation recrystallization (SGR, Passchier & Trouw, 2005). Quartz also occurs as a vermicular intergrowth in plagioclase which is collectively known as myrmekite (Sederholm, 1899). Larger quartz clasts are characterized by undulose extinction. Epidote occurrence within biotite flakes possibly means metasomatic biotite replacement by epidote (Figure 4.2b). This replacement can be explained by the following reaction (7).

biotite+plagioclase+quartz+H_2O+O_2+Ca^{2+} = epidote+K-feldspar+H^+ (Wintsch et al., 2005) (7)

Marble

Sample1431: assemblage of cal-aug-Kfs-pl-qz-zo

This sample is a coarse-grained impure marble mainly composed coarse calcite (Figure 4.3l and m). Many mineral phases such as K-feldspar, augite, plagioclase, and quartz are found within calcite aggregates. Plagioclase includes several zoisite inclusions. These inclusions are found to be surrounded by the intergrowth of albitic domain in that host plagioclase (Figure 4.3m).

Sample1425: assemblage of cal-di-qz-pl

This is another sample of impure marble with bimodal grain size distribution of calcite (Figure 4.3n). Cacite is only the dominant phase in coarse-grained domain associated with minor fraction of diposide. Whereas, fine-grained region is interlayered within the coarse-grained domain and it is rather a polyphase mixture constituted by calcite, quartz, diopside and plagioclase.

4.4.2. Lower GHS samples

Pelitic gneiss

Sample UM1325: assemblage of grt-bt-ms-pl-qz-ilm-aln-ap

This sample is a migmatitic metapellites from the immediate hanging wall of the MCT, which marks structurally lowermost unit of GHS (Figure 4.4a and b). Grain size is much larger than that of the Munsiari formation rocks. This rock contains the assemblage of garnet, biotite, muscovite, plagioclase, quartz and ilmenite, apatite, allanite as accessories. The main foliation is formed by coarse grained muscovite layers depicting the nature of anastomosing disjunctive foliation (Passchier & Trouw, 2005). Fine grained biotite flakes are dispersed into the quartzo- feldspathic domains. It is found that garnet porphyroblasts (up to 2.5 mm in diameter) are mostly associated

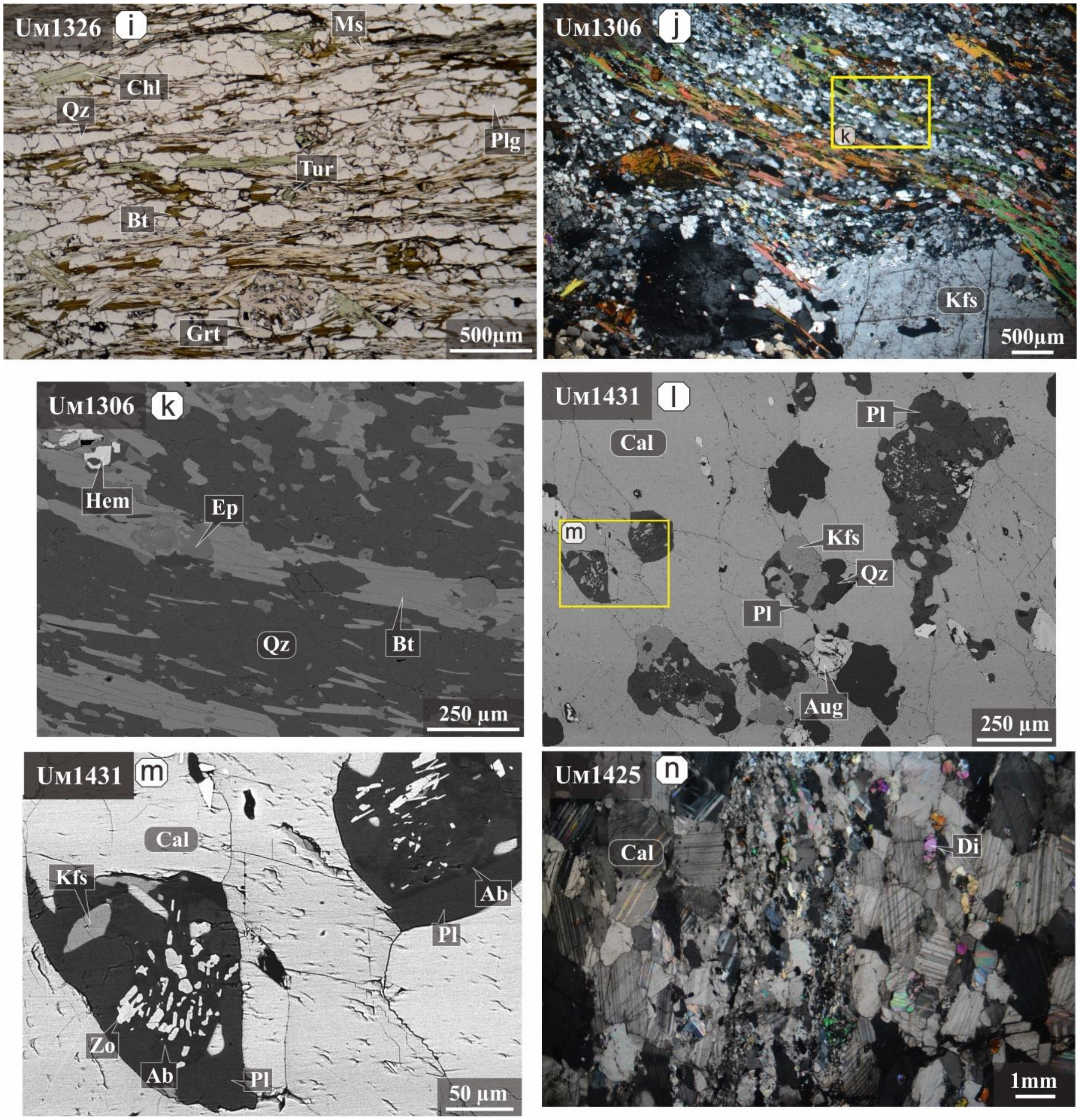

Figure 4.3. Representative microstructures of the metamorphic rocks from the Munsiari Formation (MCTZ). (i) garnet-bearing metapelite from the upper part of Munsiari Formation; (j) orthogneiss showing the presence of feldspar porphyroclast and well-developed mylonitic foliation; (k) biotite flakes in the mylonitic foliation associated with epidote; (l) marble containing augite, plagioclase and K-feldspar; (m) plagioclase with inclusions of zoisite, showing patchy zonation; (n) marble consisting of diopside, plagioclase and K-feldspar.

with quartzo-feldspathic aggregates. Unlike the MCTZ garnet porphyroblast, inclusions in L-GHS garnets are randomly orientated throughout the crystal. Inclusion phases show the occurrence of quartz, apatite, allanite, zircon and minor ilmenite where allanite exhibits patchy zonation of cerium (Ce).

Sample UM17102: assemblage of grt-bt-ms-pl-qz-ky-chl

This is a garnet-kyanite bearing pelitic gneiss, which marks the first appearance of kyanite in this study area (Figure 4.4c and d). It comprises of garnet, kyanite, biotite, muscovite, plagioclase, quartz, chlorite and some minor oxide phases. Garnet crystals are much smaller than other garnet in L-GHS. Kyanite grains are located within the main foliation defined by muscovite and biotite. Among L-GHS samples, chlorite is present only in this specimen where it is found to be attached with biotite (Figure 4.4d). Production of kyanite can be explained by the reaction (8) whereas the hydrous reaction (9) could explain retrograde biotite breakdown to chlorite (Spear, 1993).

staurolite = garnet + biotite + Al_2Si0_5 + H_2O (8)
staurolite + chlorite ↔ biotite + kyanite + H_2O (9)

Sample UM17129: assemblage of grt-bt-ms-pl-qz-ilm-rt-ky-and-ap

This sample is a coarse-grained garnet-kyanite bearing pelitic gneiss (Figure 4.4e) where modal abundance of kyanite is lesser than the other kyanite bearing samples (UM17102 and um17119). Garnet porphyroblast (up to 1.2 mm in diameter) is more or less anhedral due to presence of biotite flakes at the edges. Other major matrix phases are muscovite, plagioclase and quartz. Garnet porphyroblasts are generally lack of internal fabric and rich in a variety of randomly oriented inclusion phases including andalusite, biotite, muscovite, cordierite, quartz and zircon. Accessory phases found in matrix, are rutile, ilmenite, monazite, apatite and zircon.

Sample UM17119: assemblage of grt-bt-pl-qz-ky-rt

This sample is another garnet-kyanite bearing pelitic gneiss collected from the highest structural level of the study area (Figure 4.4f). Garnet porphyroblasts are anhedral with up to 2.5 mm in diameter. Matrix phases are mostly dominated by plagioclase, quartz and kyanite. Biotite is less abundant. Muscovite is absent. Rutile is dominant accessory phase along with some monazite and zircon. Garnet porphyroblast is rich in inclusion except a narrow zone near rim. Inclusion phases are primarily quartz associated with minor plagioclase and biotite.

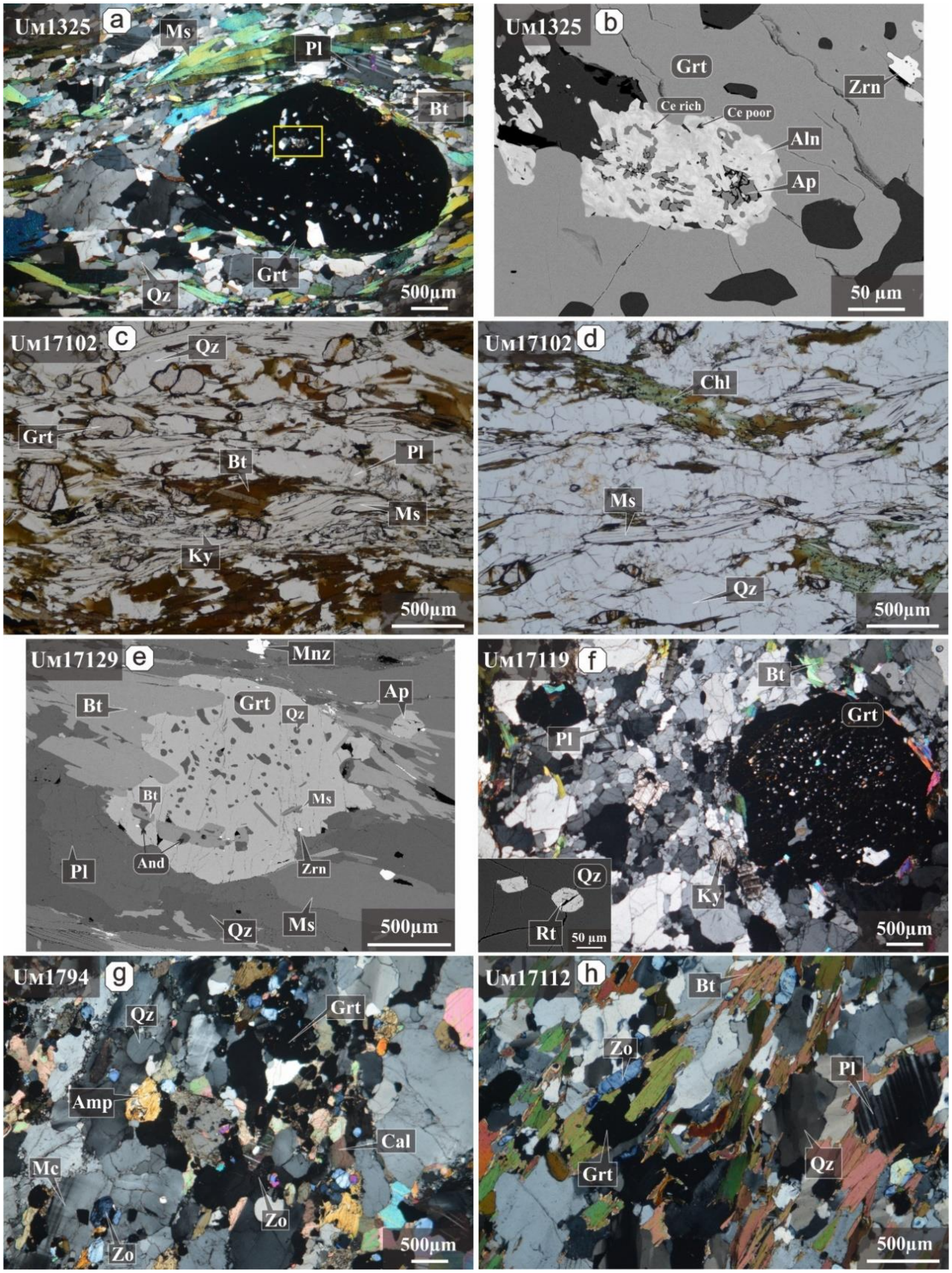

Figure 4.4. Representative microstructures of the metamorphic rocks from the L-GHS. (a) Garnet bearing pelitic gneiss with relatively coarse-grained micas and quartzofeldspathic aggregates. (b) Inclusion allanite in garnet porphyroblast showing patchy zonation. (c) Sample showing the presence of elongated kyanite along with garnet, micas and plagioclase. (d) Retrograde chlorite associated with biotite in kyanite bearing gneiss. (e) Kyanite bearing pelitic gneiss contains inclusions of biotite, andalusite, muscovite, quartz and minor zircon. (f) Garnet- kyanite bearing pelitic gneiss where rutile (inset) is present in the matrix. (g, h) Calc-gneiss comprised of garnet, zoisite, calcite, K-feldspar, plagioclase and micas.

Table 4-1. Mineral Assemblages of the study area.

Mineral Phases	Grt	Bt	Ms	Pl	Kfs	Chl	Cld	Pg	St	Ky	And	Tur	Zo	Ep	Aln	Ap	Spn	Ilm	Rt	Cal	Aug	Di
Munsiari Formation																						
UM1755	●	●	●			●						●		●	●	●		●				
UM1757	●	●	●	●		●	●								●			●				
UM17152	●		●	●		●		●				●		●	●	●		●				
UM1785						●						●										
UM1326	●	●	●	●		●						●						●				
UM1421		●	●	●		●			●													
UM1787	●	●	●			●												●				
UM1306		●	●	●	●								●	●		●						
UM1425																				●		●
UM1431				●	●								●							●	●	
UM1427			●	●	●							●										
UM1773																	●				●	
Lower GHS																						
UM1325	●	●	●	●											●	●		●				
UM17102	●	●	●	●		●				●									●			
UM17112	●	●		●									●									
UM1793	●	●			●							●	●									
UM17129	●	●	●	●						●	●					●		●	●			
UM17119	●	●		●						●									●			

Calc-silicate rocks

Sample UM1794: assemblage of qz-grt-mc-zo-cal-amp

This sample is a garnet-amphibole bearing calc-silicate rocks (Figure 4.4g). Other mineral phases are calcite, zoisite, K-feldspar and quartz. Plagioclase and mica are relatively less abundant. K-feldspar, mainly microcline is abundant in this sample.

UM17112: assemblage of qz-bt-grt-pl-zo

This sample is a representative sample taken from a calc-silicate belt in kyanite zone (Figure 4.4h). Mineral assemblage is zoisite, garnet, biotite, quartz, and plagioclase.

4.5. Mineral chemistry

4.5.1. Garnet

Growth zoning exclusively persists in the garnets of the Munsiari formation (MCTZ) which can be observed prominently through the X-ray elemental maps for Mn (Figure 4.5) and EPMA line profiles of X_{sps} (= Mn/(Mn +Mg + Ca + Fe)) concentration from core to rim (Figure 4.6a, b and c). In all the cases, a “bell shaped” line profile for X_{Mn} characterizes the MCTZ garnets, which further corresponds to a prograde metamorphic reaction (e.g. Tracy et al., 1976; Spear, 1993). Basically, the zoning profile exhibits a decrease in X_{sps} towards rim where minimum X_{sps} represents the peak metamorphic condition. The zoning relatively is more strong in small garnets of uppermost MCTZ sample (UM1326) where garnet shows a gradual decrease of X_{sps} , balanced by an increase of X_{prp}, from the core (X_{sps} = 14.5%, X_{prp} = 5.1%) to the mantle (X_{sps} = 2.2 %, X_{prp} = 9.1%) (Figure 4.6c). While the outermost rim of this garnet (UM1326) shows noticeable increase in X_{sps} which is visible in the X-ray elemental map (Figure 4.5), suggesting a diffusion-controlled retrograde zoning because of the exchange of Fe-Mg cation between garnet rim and biotite at the contact during cooling (e.g. Florence and Spear, 1991; Spear, 1991, 1993; Kohn and Spear, 2000; Caddick et al., 2010). On the other hand, large garnet crystals of the MCTZ preserves relatively weaker growth zoning, for instance, X_{sps} of the garnets in the sample UM1755 (structurally lowermost sample of the MCTZ) decreases from 9% to 0.7% towards rim.

In contrast to the growth zoning of the MCTZ garnets, L-GHS garnets is basically characterized by the diffusional zoning profile except one sample (UM1325) in lower most part. Growth zoning profile of sample UM1325 shows a noticeable decrease in X_{sps} from 16% at the core to 2.8% at the rim followed by a sharp increase up to 5% at the outermost rim (Figure 4.6d). Sample UM1407 exhibits a flat zoning profile (Figure 4.6e) with rimward composition more or less similar to the core (Fe/Fe+Mg= X_{Fe}= 72%, X_{sps} = 2.2%, X_{grs}= 6% and X_{prp}= 26%). However, the rim represent a zone of increasing X_{Fe} and decreasing X_{prp} (outermost rim: X_{Fe}= 82% and X_{prp}= 17%). Compositional characteristics of sample UM17129 (Figure 4.6f) is much similar to the sample UM1407. Structurally higher most sample UM17119 is relatively enriched with X_{prp} (= 53% at core) and as a result, X_{Fe} become less (= 49% at core) (Figure 4.6g). X_{grs} has decreased markedly (core: <1%) from other samples. Whereas, the rim is characterized by a zone of decreasing X_{prp} (Outermost rim: 40%) and increasing X_{Fe} (outermost rim: 61%). Hence, these flat profiles suggest homogenization of the cations during high temperature diffusion and the chemical gradient near rim could be explained by retrograde Fe-Mg reaction during exhumation (e.g. Florence & Spear, 1991; Spear, 1991, 1993; Kohn & Spear, 2000; Caddick et al., 2010) and retrograde garnet consumption (Kohn & Spear, 2000; Viruete et al., 2000). Therefore, it is observed that a significant change in the composition at the point of peak metamorphism has been encountered from growth zoning (rim composition, UM1325: X_{prp}= 6.6 %, X_{Fe}= 92.5%) to diffusi-

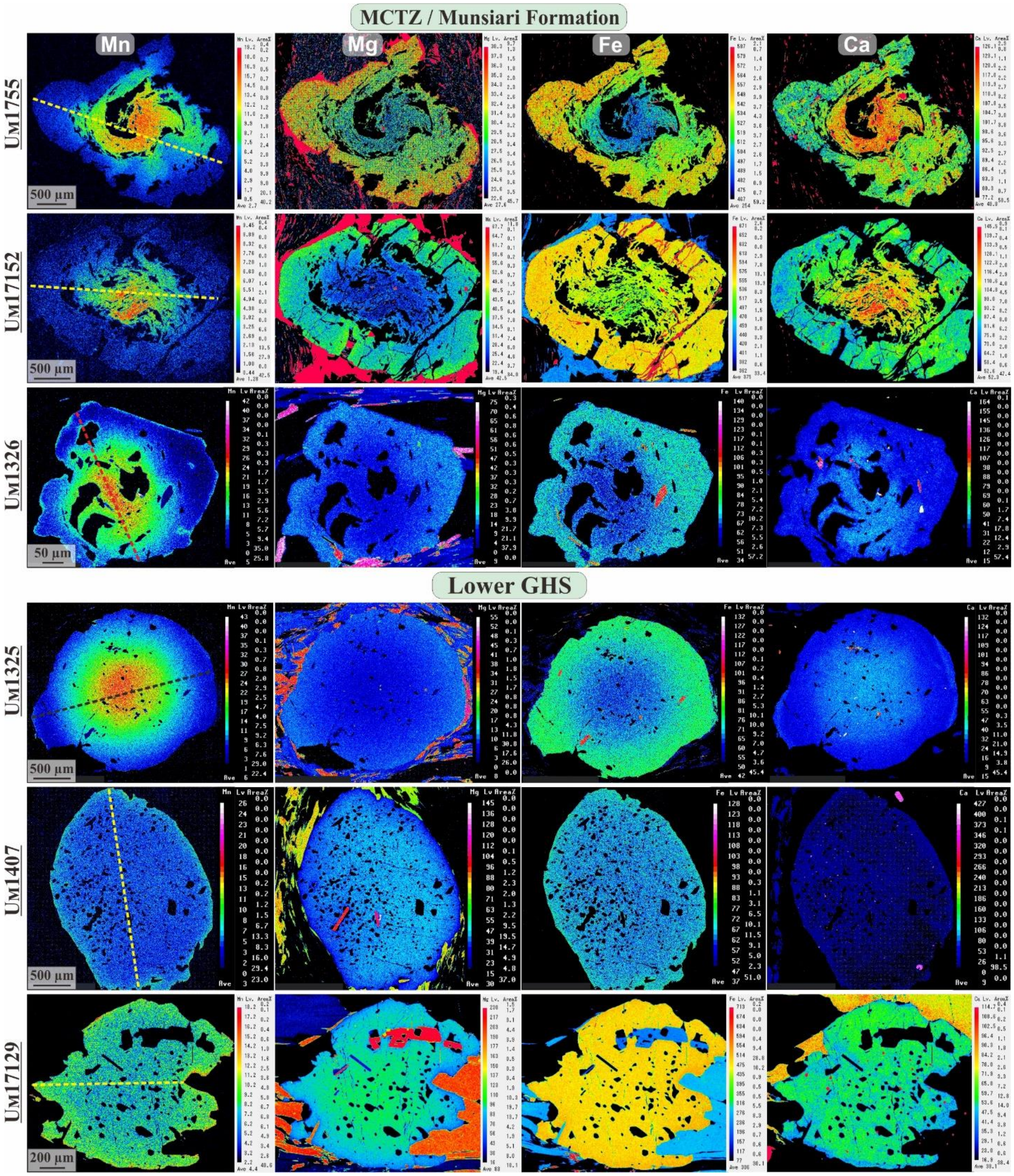

Figure 4.5. X-ray compositional maps of garnets from the representative samples obtained for the elements of Mn, Mg, Fe and Ca. EPMA line profile analysis was done through the dashed lines marked in garnets.

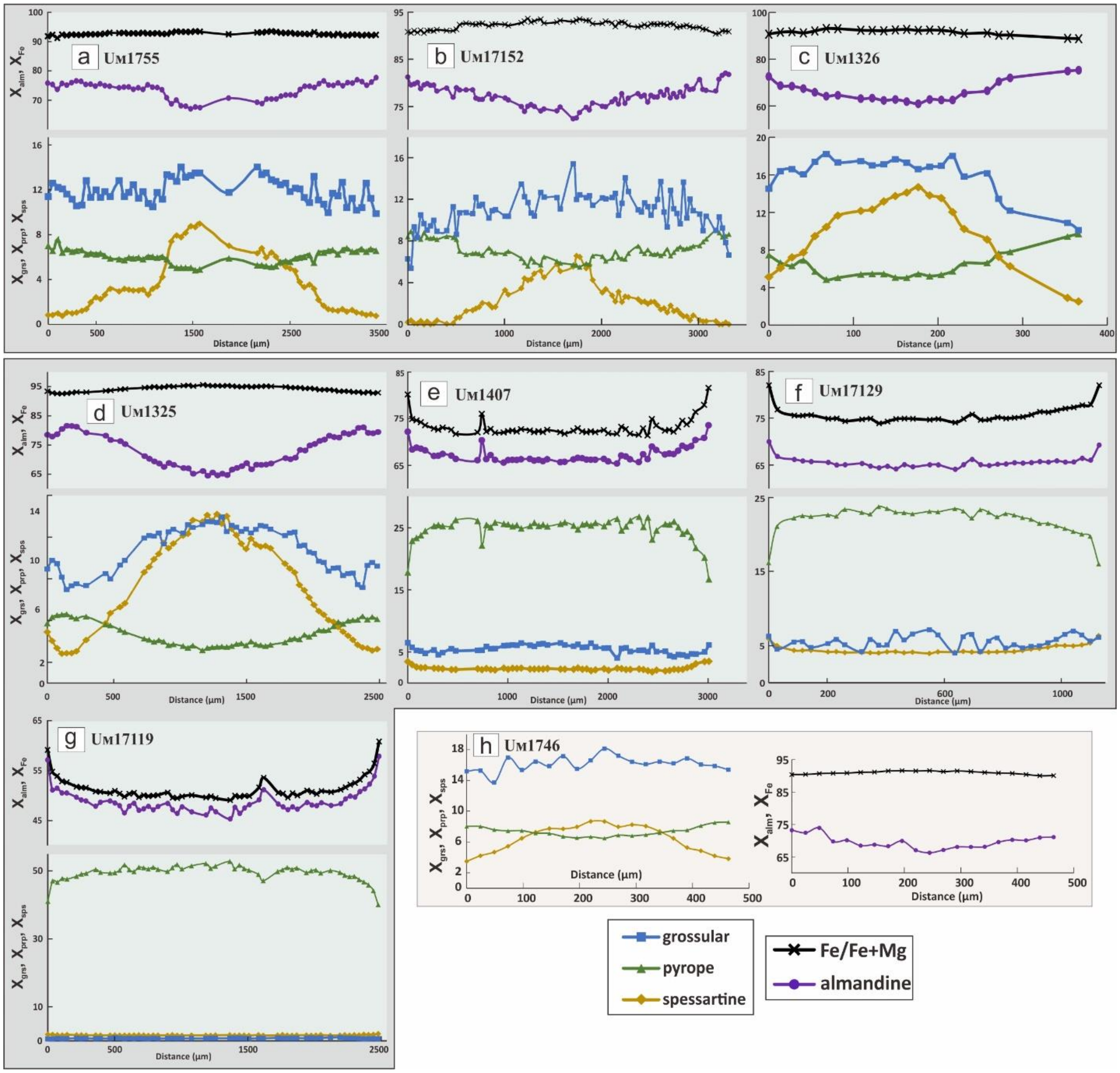

Figure 4.6. EPMA line profiles of zoned garnets showing relative concentration of elements. Figures (a-g) showing the variation in the compositional profiles towards higher structural level across the MCT. (a-c) Garnets from the Munsiari Formation. (d-g) Garnets from the L-GHS. (h) Zoning profile of garnet in metabasic rock of the Munsiari Formation.

onal zoning (core composition, UM17129: X_{prp}= 23%, X_{Fe}= 74%) (Figure 4.6d-g). All garnet compositions are summarized in the Table 4-2.

4.5.2. Biotite

Chemical compositions of biotite were analyzed for grains in the matrix, in contact with garnet and inclusions in garnet porphyroblasts. Chemical compositions of biotite grains in the matrix are nearly homogeneous in all samples, and show no significant variation within a single crystal and between different grains in thin sections. In the case of Lower MCTZ samples, X_{Mg} of biotite matrix shows X_{Mg} of 0.47-0.49 and Ti content of 0.15-0.17 *a.p.f.u* (= atoms per formula unit). Whereas, in the upper MCTZ samples, X_{Mg} and Ti concentration of matrix biotite varies from 0.35 to 0.45 and 0.16 to 0.18 *a.p.f.u* respectively. Sample UM1325 (lower most GHS) exhibits a sharp decrease in X_{Mg} to 0.27 and a rise in Ti up to 0.31 *a.p.f.u* from upper MCTZ samples. Matrix Biotite composition from other lower GHS samples ranges from 0.50 to 0.57 for X_{Mg} and this amount increases up to 0.77 in the higher most sample (UM17119). On the other hand, Ti content starts increasing from the upper MCTZ samples (from 0.20 to 0.37 *a.p.f.u.)* and then decreases to 0.24 a.p.f.u. in UM17119 from the lower GHS. Hence, there is steep compositional gradient observed across the MCT (Figure 4.7a and b). In all samples, biotite composition in contact with garnet is more or less similar to the matrix composition. X_{Mg} of inclusion biotite is generally higher than that of matrix. In addition, $X_{Mg\ VS.}$ Ti scatter plot for the matrix biotite shows two distinct clusters showing the difference between the MCTZ and L-GHS samples (Figure 4.7c). All biotite compositions are summarized in the Table 4-3.

4.5.3. White mica

White micas are among the most abundant phyllosilicates in metasedimentary rocks of almost all the bulk compositions. They occur in a wide range of metamorphic conditions, and exhibit extensive compositional variations strongly controlled by the degree of metamorphism (Guidotti and Sassi, 1998). They display a number of chemical substitutions, with complete solid-solution between idealized muscovite (Al-rich) and celadonite (Fe-rich) end members, partial solid-solution between muscovite and paragonite, and substitution by Ti in the octahedral sites (Guidotti, 1984). Among them, the Tschermak substitution $[(Mg, Fe^{2+})^{vi}, Si^{iv}=Al^{vi}, Al^{iv}]$, which controls the chemistry of phengites, is thought to be particularly sensitive to metamorphic conditions (Guidotti, 1984). In this study, white mica compositions are analyzed on the basis of celadonite content (Figure 4.7e), Tschermak substitution (Figure 4.7f), Ti substitution on tetrahedral site (Figure 4.7g) and Na/Na+K ratio (Figure 4.7h) by following other previous work on white micas of MCTZ samples (Paudel & Arita, 2006; Montemagni et al., 2018). Additionally, four samples of orthogneiss (UM1315, UM1309, UM1303 and UM1320) from the MCTZ, has also been analyzed to correlate the metamorphic condition with that of metapellites. Composition of ideal muscovite (Al_2O_3 = 38.4%, FeO = 0%) is taken as a reference (Figure 4.7e).

In the MCTZ, white mica constituting main foliation (S_m) of metapellites shows occurrence over wider range of Al_2O_3 (34% to 38%) and relatively narrow range of FeO (0.89% to 1.86%). Relicts white mica constituting older foliation (S_{m-1}) in sample UM1755 and porphyroblasts in sample UM1757 have the composition very close to S_m. White mica in mylonitic orthogneiss shows relatively lower amount of Al_2O_3 (30.31% to 34.08%) and higher FeO (1.72% to 4.65%). On the other hand, white micas from L-GHS is a bit scattered showing a wide range of celadonite-rich compositions (Al_2O_3: 31.12-34.78%, FeO: 1.39-3.78%). Figure 4.7f shows the degree of Tschermak substitution with respect to a line with a slope of -1 which represents the balance in substitution between the octahedral site and tetrahedral site. The line is basically fitted with the compositions of L-GHS samples and MCTZ orthogneiss. Whereas, the compositions of MCTZ metapellites are relatively scattered around the line. Ti concentration in tetrahedral site is higher for L-GHS ranging from 0.07 to 0.12 *a.p.f.u.* whereas MCTZ samples show a range from 0.0004 to 0.03 *a.p.f.u.* (Figure 4.7g). Na/Na+K ratio is much higher in sample UM17152 where paragonite (Na-white mica) is also found along with K-white micas (Na= from 0.50 in K-white micas to 1.47 *a.p.f.u.* in paragonite). All muscovite compositions are summarized in the Table 4-4.

4.5.4. Plagioclase

Plagioclase in MCTZ samples shows a range of X_{An} content from 11.62 to 27.53. Lower most sample UM1325 has X_{An} ranging from 8.63 to 12.64. Other samples in lower GHS contain X_{An} ranging from 16.56 to 24.53 except the structurally higher most sample UM17119 having X_{An} ranging from 4.56 to 5.86. All plagioclase compositions are summarized in the Table 4-5 and plotted in ternary diagram (Figure 4.7d).

4.5.5. Chlorite

In lower MCTZ, X_{Mg} of matrix chlorite composition varies from 0.43 to 0.44 whereas in the upper MCTZ, retrograde chlorite of the sample UM17152 contains X_{Mg} of 0.42 and prograde chlorite of the sample UM1326 has X_{Mg} of 0.49. All chlorite compositions are summarized in the Table 4-6.

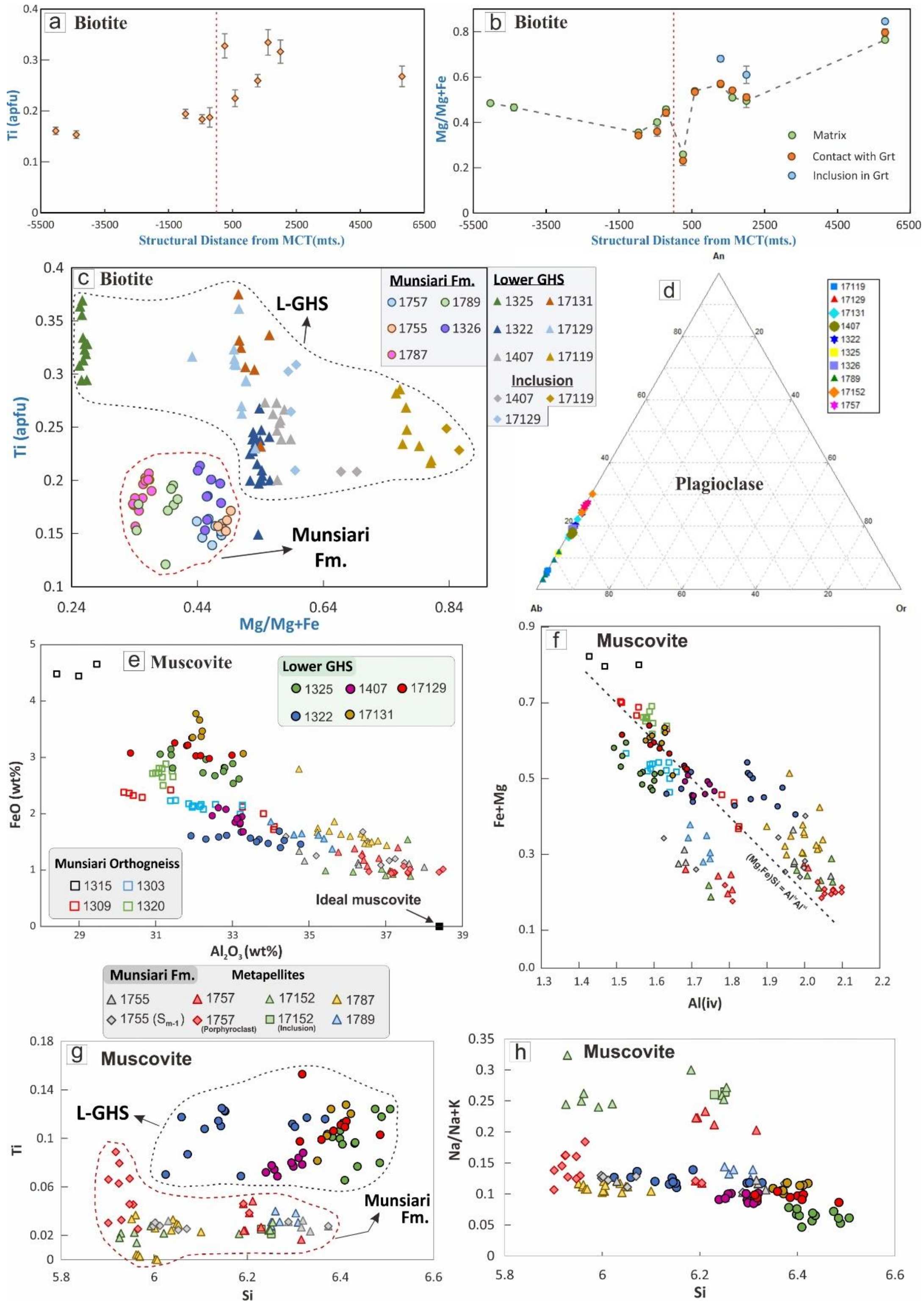

Figure 4.7. Scatter plots showing the chemical compositions of matrix phases. (a, b) Variation of Ti concentration (a.p.f.u) and X_{Mg} plotted in biotite across the MCT; (c) Ti (a.p.f.u) v. X_{Mg} in biotite; (d) plagioclase compositions; (e) FeO v. Al_2O_3 plot for muscovite; (f) Fe+Mg (a.p.f.u) v. Al(iv) (a.p.f.u) plot showing the degree of Tschermak substitution; (g) Ti (a.p.f.u) v. Si (a.p.f.u) and (h) X_{Na} v. Si (a.p.f.u) for muscovite.

Table 4-2. Representative garnet compositions (wt%) obtained from EPMA analysis.

Sample No.	1325			1322		1407		17131		17129		17119		1794		17120	
Position	Gt_C	Gt_{NR}^+	Gt_R	Gt_C^+	Gt_R	Gt_C^+	Gt_R	Gt_C^+	Gt_R	Gt_C^+	Gt_R	Gt_C^+	Gt_R	Gt_R	Gt_C^+	Gt_C^+	Gt_R
SiO2	35.66	36.82	36.24	37.78	37.63	39.83	38.11	37.86	37.45	37.24	36.96	39.51	39.37	40.74	35.97	37.27	38.13
TiO2	0.04	0.01	0.00	0.00	0.00	0.07	0.00	0.01	0.01	0.00	0.01	0.00	0.01	0.03	0.11	0.07	0.05
Al2O3	21.59	21.54	21.55	21.75	21.03	22.41	21.75	20.88	20.31	20.58	21.54	23.78	22.66	17.92	20.89	21.10	20.93
Cr2O3	0.00	0.00	0.05	0.00	0.00	0.04	0.05	0.07	0.00	0.02	0.00	0.00	0.01	0.09	0.11	-0.01	0.05
FeO	29.68	36.55	34.81	31.31	32.41	31.05	33.82	31.27	33.78	31.05	32.91	24.65	28.34	18.89	20.14	22.86	22.19
MnO	6.78	1.24	2.09	1.08	1.26	1.05	1.57	1.44	2.94	1.81	2.59	0.50	0.58	1.96	3.40	1.99	3.13
MgO	0.81	1.63	1.39	5.14	3.99	6.88	4.27	6.20	3.79	5.85	4.01	13.98	10.84	1.65	0.73	4.30	3.89
CaO	5.33	3.08	3.69	3.99	4.19	2.27	2.20	2.91	2.66	2.90	2.73	0.31	0.22	18.04	17.27	11.72	12.21
Na2O	0.09	0.03	0.03	0.03	0.03	0.03	0.03	0.00	0.02	0.03	0.00	0.00	0.00	0.00	0.01	0.05	0.05
K2O	0.00	0.00	0.00	0.00	0.00	0.02	0.02	0.00	0.01	0.01	0.01	0.00	0.33	0.00	0.00	0.03	0.03
Total	99.98	100.91	99.86	101.07	100.55	103.64	101.81	100.65	100.96	99.48	100.75	102.72	102.36	99.34	98.63	99.37	100.67
Si	2.91	2.96	2.95	2.96	2.99	3.01	2.99	2.98	2.99	2.97	2.94	2.90	2.96	3.19	2.90	2.94	2.97
Ti	0.00	0.00	0.00	0.00	0.00	0.00	0.00	0.00	0.00	0.00	0.00	0.00	0.00	0.00	0.01	0.00	0.00
Al	2.08	2.04	2.07	2.01	1.97	1.99	2.01	1.94	1.91	1.94	2.02	2.06	2.01	1.66	1.99	1.97	1.93
Cr	0.00	0.00	0.00	0.00	0.00	0.00	0.00	0.00	0.00	0.00	0.00	0.00	0.00	0.00	0.00	0.00	0.00
Fe	2.02	2.46	2.37	2.05	2.15	1.96	2.22	2.06	2.26	2.07	2.19	1.51	1.78	1.24	1.36	1.51	1.45
Mn	0.47	0.08	0.14	0.07	0.09	0.07	0.10	0.10	0.20	0.12	0.18	0.03	0.04	0.13	0.23	0.13	0.21
Mg	0.10	0.20	0.17	0.60	0.47	0.77	0.50	0.73	0.45	0.70	0.48	1.53	1.21	0.19	0.09	0.50	0.45
Ca	0.47	0.27	0.32	0.34	0.36	0.18	0.18	0.25	0.23	0.25	0.23	0.02	0.02	1.51	1.49	0.99	1.02
Na	0.01	0.00	0.00	0.00	0.00	0.00	0.00	0.00	0.00	0.00	0.00	0.00	0.00	0.00	0.00	0.00	0.00
K	0.00	0.00	0.00	0.00	0.00	0.00	0.00	0.00	0.00	0.00	0.00	0.00	0.03	0.00	0.00	0.00	0.00
Total	8.06	8.02	8.02	8.04	8.03	8.00	8.01	8.05	8.05	8.06	8.04	8.07	8.05	7.93	8.06	8.04	8.03

Sample No.	1755		1757			17152		1787			1789			1326		
Position	Gt_C	Gt_R^+	Gt_C	Gt_{NR}^+	Gt_R	Gt_C	Gt_R^+	Gt_C	Gt_{NR}^+	Gt_R	Gt_C	Gt_{NR}^+	Gt_R	Gt_C	Gt_{NR}^+	Gt_R
SiO2	36.70	36.41	38.97	35.69	36.10	35.59	36.36	35.42	36.22	35.86	36.82	37.18	37.41	37.54	37.62	37.09
TiO2	0.11	0.00	0.02	0.04	0.04	0.06	0.05	0.01	0.00	0.00	0.17	0.06	0.04	0.04	0.01	0.00
Al2O3	19.89	20.16	20.93	22.36	22.20	22.10	22.10	21.95	22.19	22.41	19.77	20.37	20.30	21.09	21.09	21.31
Cr2O3	0.00	0.04	0.00	0.00	0.00	0.03	0.04	0.02	0.03	0.02	0.53	0.03	0.10	0.00	0.00	0.00
FeO	32.09	35.87	33.99	36.18	37.26	33.89	36.08	37.40	39.67	39.75	29.29	34.49	34.41	29.39	34.12	35.08
MnO	3.92	0.35	1.80	1.11	1.19	1.49	0.12	2.88	0.57	0.51	7.78	1.71	1.84	6.10	1.73	2.10
MgO	1.22	1.72	1.92	2.08	1.89	1.31	2.33	1.62	2.33	2.16	0.74	1.41	1.63	1.32	2.16	2.23
CaO	6.35	5.55	4.22	4.06	2.87	6.42	4.45	1.66	0.90	0.89	6.09	6.18	5.77	6.28	4.76	3.47
Na2O	0.00	0.01	0.01	0.01	0.04	0.02	0.00	0.04	0.03	0.00	0.02	0.02	0.01	0.00	0.02	0.03
K2O	0.02	0.01	0.00	0.00	0.03	0.00	0.00	0.00	0.00	0.02	0.00	0.01	0.03	0.00	0.00	0.00
Total	100.29	100.11	101.88	101.52	101.62	100.90	101.53	101.01	101.94	101.61	101.21	101.46	101.55	101.76	101.52	101.30
Si	2.99	2.97	3.07	2.86	2.90	2.87	2.90	2.88	2.90	2.88	2.98	2.98	3.00	2.99	2.99	2.97
Ti	0.01	0.00	0.00	0.00	0.00	0.00	0.00	0.00	0.00	0.00	0.01	0.00	0.00	0.00	0.00	0.00
Al	1.91	1.94	1.94	2.11	2.10	2.10	2.08	2.10	2.09	2.12	1.89	1.93	1.92	1.98	1.98	2.01
Cr	0.00	0.00	0.00	0.00	0.00	0.00	0.00	0.00	0.00	0.00	0.03	0.00	0.01	0.00	0.00	0.00
Fe	2.18	2.44	2.24	2.43	2.50	2.28	2.41	2.54	2.66	2.67	1.98	2.31	2.30	1.96	2.27	2.35
Mn	0.27	0.02	0.12	0.08	0.08	0.10	0.01	0.20	0.04	0.03	0.53	0.12	0.12	0.41	0.12	0.14
Mg	0.15	0.21	0.23	0.25	0.23	0.16	0.28	0.20	0.28	0.26	0.09	0.17	0.19	0.16	0.26	0.27
Ca	0.55	0.48	0.36	0.35	0.25	0.55	0.38	0.14	0.08	0.08	0.53	0.53	0.49	0.54	0.41	0.30
Na	0.00	0.00	0.00	0.00	0.01	0.00	0.00	0.01	0.01	0.00	0.00	0.00	0.00	0.00	0.00	0.00
K	0.00	0.00	0.00	0.00	0.00	0.00	0.00	0.00	0.00	0.00	0.00	0.00	0.00	0.00	0.00	0.00
Total	8.06	8.07	7.96	8.08	8.06	8.08	8.06	8.07	8.05	8.05	8.05	8.05	8.04	8.02	8.02	8.03

Gt_C = core Composition, Gt_{NR} = near rim Composition, Gt_R = rim Composition; $^+$Composition for the thermobarometric analysis; Garnet structural formula was recalculated on the basis of 12 O.

Table 4-3. Representative biotite compositions (wt%) obtained from EPMA analysis.

	Munsiari formation/MCTZ									Lower GHS			
Sample No.	**1755**		**1757**	**1787**		**1789**		**1326**		**1325**		**1322**	
Position	Bt_{cnt}^{+}	Bt_{m}	Bt_{m}^{+}	Bt_{cnt}	Bt_{m}^{+}	Bt_{cnt}	Bt_{m}^{+}	Bt_{cnt}	Bt_{m}^{+}	Bt_{cnt}	Bt_{m}^{+}	Bt_{cnt}	Bt_{m}^{+}
SiO2	35.21	34.97	34.97	34.13	34.74	35.08	35.82	34.52	35.80	33.86	34.04	35.17	35.80
TiO2	1.40	1.51	1.30	1.35	1.59	1.52	1.68	1.71	1.43	2.43	2.62	2.02	1.81
Al2O3	19.94	19.38	19.76	19.37	19.16	18.37	18.15	18.78	18.32	17.24	17.58	18.96	19.62
Cr2O3	0.02	0.04	0.05	0.00	0.00	0.06	0.05	0.04	0.00	0.01	0.04	0.00	0.06
FeO	20.21	19.25	19.55	24.29	23.31	23.38	22.59	20.48	20.56	26.24	25.84	18.28	17.24
MnO	0.01	0.01	0.00	0.04	0.01	0.11	0.07	0.06	0.07	0.15	0.16	0.11	0.05
MgO	10.16	10.49	10.06	7.06	7.12	6.95	8.39	9.77	9.64	5.27	5.22	11.39	12.06
CaO	0.00	0.00	0.00	0.00	0.04	0.00	0.00	0.00	0.03	0.00	0.00	0.00	0.00
Na2O	0.17	0.23	0.19	0.22	0.15	0.06	0.10	0.17	0.12	0.05	0.05	0.19	0.26
K2O	9.57	9.28	9.36	10.09	9.78	8.57	8.74	10.30	9.77	9.80	9.70	9.63	9.57
Total	96.69	95.15	95.24	96.54	95.95	94.10	95.59	95.81	95.74	95.06	95.24	95.74	96.47
Si	5.30	5.33	5.33	5.29	5.37	5.49	5.49	5.30	5.46	5.39	5.39	5.31	5.33
Ti	0.16	0.17	0.15	0.16	0.18	0.18	0.19	0.20	0.16	0.29	0.31	0.23	0.20
Al	3.54	3.48	3.55	3.53	3.49	3.39	3.28	3.40	3.30	3.24	3.28	3.38	3.44
Cr	0.00	0.00	0.01	0.00	0.00	0.01	0.01	0.00	0.00	0.00	0.01	0.00	0.01
Fe	2.54	2.45	2.49	3.15	3.01	3.06	2.90	2.63	2.62	3.50	3.42	2.31	2.15
Mn	0.00	0.00	0.00	0.00	0.00	0.01	0.01	0.01	0.01	0.02	0.02	0.01	0.01
Mg	2.28	2.38	2.28	1.63	1.64	1.62	1.92	2.23	2.19	1.25	1.23	2.57	2.68
Ca	0.00	0.00	0.00	0.00	0.01	0.00	0.00	0.00	0.01	0.00	0.00	0.00	0.00
Na	0.05	0.07	0.06	0.07	0.04	0.02	0.03	0.05	0.03	0.02	0.02	0.06	0.08
K	1.84	1.80	1.82	1.99	1.93	1.71	1.71	2.02	1.90	1.99	1.96	1.86	1.82
Total	15.71	15.69	15.68	15.82	15.68	15.50	15.54	15.84	15.69	15.70	15.64	15.72	15.69

	Lower GHS										
Sample No.	**1407**			**17131**		**17129**			**17119**		
Position	Bt_{in}	Bt_{cnt}	Bt_{m}^{+}	Bt_{cnt}	Bt_{m}^{+}	Bt_{in}	Bt_{cnt}	Bt_{m}^{+}	Bt_{in}	Bt_{cnt}	Bt_{m}^{+}
SiO2	38.73	38.25	37.77	36.67	36.36	36.41	36.22	36.58	39.76	39.03	38.58
TiO2	1.98	2.21	2.52	2.73	2.88	2.38	2.79	3.23	2.40	2.20	2.20
Al2O3	19.60	18.73	18.87	17.70	16.34	18.60	17.05	16.85	17.85	18.01	17.50
Cr2O3	0.02	0.03	0.03	0.00	0.00	0.00	0.03	0.07	0.05	0.13	0.17
FeO	11.90	15.50	15.77	17.74	19.14	15.71	19.24	18.76	6.95	8.49	9.78
MnO	0.01	0.06	0.00	0.07	0.07	0.01	0.04	0.01	0.00	0.00	0.05
MgO	15.08	11.67	11.53	11.24	11.13	12.60	10.73	10.78	19.81	18.17	17.94
CaO	0.02	0.00	0.03	0.00	0.00	0.00	0.00	0.00	0.00	0.00	0.00
Na2O	0.47	0.23	0.27	0.23	0.20	0.36	0.25	0.25	1.13	0.76	0.69
K2O	9.65	10.23	10.23	9.49	9.30	8.88	9.36	9.42	7.36	7.33	8.07
Total	97.46	96.89	97.02	95.87	95.42	94.95	95.70	95.94	95.31	94.11	94.98
Si	5.53	5.61	5.54	5.50	5.53	5.44	5.49	5.52	5.61	5.61	5.57
Ti	0.21	0.24	0.28	0.31	0.33	0.27	0.32	0.37	0.25	0.24	0.24
Al	3.30	3.24	3.26	3.13	2.93	3.28	3.05	2.99	2.97	3.05	2.98
Cr	0.00	0.00	0.00	0.00	0.00	0.00	0.00	0.01	0.01	0.01	0.02
Fe	1.42	1.90	1.93	2.23	2.43	1.96	2.44	2.37	0.82	1.02	1.18
Mn	0.00	0.01	0.00	0.01	0.01	0.00	0.01	0.00	0.00	0.00	0.01
Mg	3.21	2.55	2.52	2.51	2.52	2.81	2.43	2.42	4.17	3.90	3.86
Ca	0.00	0.00	0.00	0.00	0.00	0.00	0.00	0.00	0.00	0.00	0.00
Na	0.13	0.06	0.08	0.07	0.06	0.10	0.07	0.07	0.31	0.21	0.19
K	1.76	1.91	1.91	1.82	1.80	1.69	1.81	1.81	1.32	1.34	1.49
Total	15.55	15.52	15.54	15.57	15.61	15.55	15.61	15.56	15.46	15.39	15.53

Bt_{cnt} = contact to Garnet, Bt_{in} = inclusion in Garnet, Bt_{m} = matrix; $^{+}$Composition for the thermobarometric analysis; Biotite structural formula was recalculated on the basis of 22 O.

Table 4-4. Representative muscovite compositions (wt%) obtained from EPMA analysis.

	Munsiari formation/MCTZ											Lower GHS					
Sample No.	**1755**		**1757**		**17152**			**1787**		**1789**	**1326**	**1325**	**1322**	**1407**	**17131**	**17129**	
Position	Ms_m	Ms_{m-1}	Ms_m^+	Ms_p	Ms_m^+	Ms_{in}	Pg_m	$Ms_{m(fine)}$	$S_{m(coarse)}$	Ms_m^+	Ms_m^+	Ms_m^+	Ms_m^+	Ms_m^+	Ms_m^+	Ms_m^+	Ms_{in}
SiO2	47.97	47.48	47.27	44.90	45.13	47.98	43.97	44.21	45.34	48.06	44.62	47.29	47.41	47.11	48.28	48.50	47.00
TiO2	0.33	0.31	0.24	0.46	0.28	0.22	0.11	0.33	0.00	0.39	0.35	0.93	1.12	0.75	1.25	1.12	0.70
Al2O3	34.74	35.19	36.19	37.58	37.00	35.73	40.69	36.36	37.03	34.81	35.03	32.18	32.85	33.15	32.19	32.05	31.92
Cr2O3	0.09	0.01	0.00	0.03	0.00	0.07	0.05	0.04	0.00	0.00	0.00	0.00	0.03	0.01	0.02	0.01	0.14
FeO	1.34	1.25	1.38	0.96	0.90	1.19	0.58	1.64	1.44	1.65	2.53	2.64	1.62	1.92	3.37	3.03	2.77
MnO	0.00	0.01	0.01	0.00	0.00	0.05	0.00	0.00	0.00	0.01	0.02	0.02	0.03	0.03	0.00	0.04	0.03
MgO	0.84	0.62	0.49	0.45	0.73	0.64	0.11	0.77	0.73	1.01	0.77	1.01	1.31	1.41	1.12	1.33	1.46
CaO	0.00	0.00	0.00	0.02	0.00	0.00	0.65	0.00	0.00	0.00	0.02	0.00	0.02	0.01	0.00	0.00	0.00
Na2O	0.80	0.69	1.63	0.98	1.92	2.00	5.81	0.92	0.96	0.84	1.71	0.63	0.93	0.82	0.81	0.68	0.74
K2O	9.23	9.13	8.63	10.50	9.25	8.45	2.98	10.62	10.67	9.03	9.70	10.78	10.61	11.21	9.20	9.63	9.50
Total	95.35	94.67	95.84	95.88	95.21	96.31	94.96	94.88	96.17	95.80	94.75	95.48	95.92	96.40	96.24	96.38	94.26
Si	6.32	6.29	6.20	5.95	5.99	6.25	5.72	5.95	6.00	6.30	6.03	6.34	6.30	6.26	6.38	6.40	6.35
Ti	0.03	0.03	0.02	0.05	0.03	0.02	0.01	0.03	0.00	0.04	0.04	0.09	0.11	0.07	0.12	0.11	0.07
Al	5.39	5.49	5.59	5.87	5.79	5.49	6.24	5.77	5.78	5.38	5.58	5.09	5.14	5.19	5.01	4.98	5.08
Cr	0.01	0.00	0.00	0.00	0.00	0.01	0.01	0.00	0.00	0.00	0.00	0.00	0.00	0.00	0.00	0.00	0.02
Fe	0.15	0.14	0.15	0.11	0.10	0.13	0.06	0.18	0.16	0.18	0.29	0.30	0.18	0.21	0.37	0.33	0.31
Mn	0.00	0.00	0.00	0.00	0.00	0.01	0.00	0.00	0.00	0.00	0.00	0.00	0.00	0.00	0.00	0.00	0.00
Mg	0.17	0.12	0.10	0.09	0.14	0.12	0.02	0.15	0.14	0.20	0.15	0.20	0.26	0.28	0.22	0.26	0.29
Ca	0.00	0.00	0.00	0.00	0.00	0.00	0.09	0.00	0.00	0.00	0.00	0.00	0.00	0.00	0.00	0.00	0.00
Na	0.20	0.18	0.41	0.25	0.49	0.50	1.47	0.24	0.25	0.21	0.45	0.16	0.24	0.21	0.21	0.17	0.19
K	1.55	1.54	1.44	1.77	1.57	1.40	0.50	1.82	1.80	1.51	1.67	1.84	1.80	1.90	1.55	1.62	1.64
Total	13.82	13.79	13.91	14.09	14.12	13.93	14.12	14.16	14.13	13.83	14.21	14.03	14.04	14.13	13.87	13.89	13.95

Ms_m = main foliation, Ms_{in} = inclusion in Garnet, Ms_{m-1} = relict older foliation, Ms_p = porphyroclast, Pg_m = Paragonite; $^+$Composition for the thermobarometric analysis; Muscovite structural formula was recalculated on the basis of 22 O.

Table 4-5. Representative plagioclase compositions (wt%) obtained from EPMA analysis.

	Munsiari formation/MCTZ					Lower GHS														
Sample No.	**1757**	**17152**		**1789**	**1326**	**1325**		**1322**		**1407**		**17131**		**17129**		**17119**		
Position	Pl_m^+	Pl_m^+	Pl_{in}	Pl_m^+	Pl_m^+	Pl_m-C	Pl_m-R$^+$	Pl_m-C	Pl_m-R$^+$	Pl_m-C	Pl_m-R$^+$	Pl_m-C	Pl_m-R$^+$	Pl_m-C	Pl_m-R$^+$	Pl_m-C	Pl_m-R$^+$	Pl_{in}
SiO2	60.83	61.78	61.36	65.56	63.80	67.33	66.20	63.61	62.12	64.80	65.47	64.66	62.88	63.71	63.62	67.48	67.72	66.22
TiO2	0.00	0.01	0.00	0.00	0.00	0.00	0.01	0.00	0.00	0.00	0.00	0.02	0.00	0.00	0.01	0.00	0.00	0.02
Al2O3	24.50	23.51	24.69	21.56	23.25	21.08	21.83	23.08	24.01	22.48	22.62	22.19	22.76	22.72	22.94	20.12	20.03	20.53
Cr2O3	0.00	0.05	0.24	0.08	0.00	0.00	0.03	0.00	0.00	0.04	0.00	0.05	0.01	0.08	0.00	0.00	0.00	0.00
FeO	0.06	0.04	0.00	0.07	0.03	0.01	0.00	0.03	0.10	0.00	0.04	0.03	0.04	0.01	0.00	0.06	0.00	0.40
MnO	0.01	0.00	0.00	0.04	0.00	0.00	0.00	0.01	0.00	0.02	0.00	0.00	0.05	0.01	0.03	0.00	0.00	0.00
MgO	0.00	0.00	0.00	0.00	0.01	0.00	0.02	0.00	0.00	0.00	0.00	0.01	0.00	0.00	0.00	0.00	0.03	0.00
CaO	6.28	5.85	5.34	2.80	4.11	1.84	2.74	4.31	5.28	3.85	3.78	3.90	5.22	4.43	4.66	1.43	1.13	1.61
Na2O	9.14	10.04	8.72	11.76	9.50	10.79	10.46	9.30	8.98	9.64	9.28	10.85	10.04	10.39	10.36	12.66	13.02	10.68
K2O	0.08	0.06	0.10	0.09	0.05	0.13	0.10	0.10	0.05	0.19	0.14	0.14	0.07	0.17	0.17	0.02	0.14	0.03
Total	100.90	101.34	100.45	101.94	100.75	101.18	101.39	100.44	100.54	101.01	101.32	101.85	101.06	101.51	101.77	101.76	102.07	99.48
Si	2.69	2.73	2.71	2.85	2.80	2.92	2.87	2.80	2.74	2.83	2.85	2.82	2.77	2.79	2.78	2.93	2.93	2.92
Ti	0.00	0.00	0.00	0.00	0.00	0.00	0.00	0.00	0.00	0.00	0.00	0.00	0.00	0.00	0.00	0.00	0.00	0.00
Al	1.28	1.22	1.29	1.11	1.20	1.08	1.12	1.20	1.25	1.16	1.16	1.14	1.18	1.17	1.18	1.03	1.02	1.07
Cr	0.00	0.00	0.01	0.00	0.00	0.00	0.00	0.00	0.00	0.00	0.00	0.00	0.00	0.00	0.00	0.00	0.00	0.00
Fe	0.00	0.00	0.00	0.00	0.00	0.00	0.00	0.00	0.00	0.00	0.00	0.00	0.00	0.00	0.00	0.00	0.00	0.01
Mn	0.00	0.00	0.00	0.00	0.00	0.00	0.00	0.00	0.00	0.00	0.00	0.00	0.00	0.00	0.00	0.00	0.00	0.00
Mg	0.00	0.00	0.00	0.00	0.00	0.00	0.00	0.00	0.00	0.00	0.00	0.00	0.00	0.00	0.00	0.00	0.00	0.00
Ca	0.30	0.28	0.25	0.13	0.19	0.09	0.13	0.20	0.25	0.18	0.18	0.18	0.25	0.21	0.22	0.07	0.05	0.08
Na	0.78	0.86	0.75	0.99	0.81	0.91	0.88	0.79	0.77	0.82	0.78	0.92	0.86	0.88	0.88	1.07	1.09	0.91
K	0.00	0.00	0.01	0.00	0.00	0.01	0.01	0.01	0.00	0.01	0.01	0.01	0.00	0.01	0.01	0.00	0.01	0.00
Total	5.06	5.09	5.02	5.09	5.01	5.00	5.01	5.00	5.02	5.00	4.97	5.07	5.07	5.07	5.07	5.09	5.11	5.00

Pl_m-C = core of matrix plagioclase, Pl_m-R$^+$ = rim of matrix plagioclase, Pl_{in} = inclusion in garnet; $^+$Composition for the thermobarometric analysis; Plagioclase structural formula was recalculated on the basis of 8 O.

Table 4-6. Representative chlorite & chloritoid compositions (wt%) obtained from EPMA analysis.

Sample No.	1755		1757	17152		1787	1789	1326	1757
Location	Chl_{cnt}	Chl_m	Chl_m^+	Chl_{cnt}	Chl_m^+	Chl_{cnt}	Chl_{cnt}	Chl_m^+	Ctd_m
SiO2	24.05	23.66	23.92	24.97	23.77	23.41	24.85	24.92	24.34
TiO2	0.11	0.09	0.10	0.09	0.09	0.08	0.10	0.03	0.00
Al2O3	21.38	22.04	22.09	23.26	21.98	22.82	20.23	22.69	38.54
Cr2O3	0.00	0.00	0.03	0.03	0.02	0.04	0.00	0.00	0.05
FeO	28.73	28.36	29.19	27.49	29.21	33.54	30.12	25.62	24.60
MnO	0.00	0.00	0.00	0.02	0.05	0.05	0.16	0.10	0.08
MgO	12.69	12.58	12.44	10.64	11.79	9.82	9.71	13.83	2.56
CaO	0.02	0.02	0.00	0.02	0.00	0.00	0.14	0.01	0.01
Na2O	0.01	0.01	0.01	0.01	0.00	0.02	0.03	0.10	0.01
K2O	0.01	0.00	0.00	0.03	0.00	0.07	0.15	0.05	0.01
Total	87.00	86.76	87.78	86.55	86.92	89.82	85.49	87.35	90.20
Si	5.22	5.14	5.15	5.37	5.18	5.04	5.54	5.28	1.72
Ti	0.02	0.02	0.02	0.01	0.01	0.01	0.02	0.01	0.00
Al	5.47	5.64	5.61	5.90	5.64	5.79	5.31	5.66	3.21
Cr	0.00	0.00	0.00	0.00	0.00	0.01	0.00	0.00	0.00
Fe	5.21	5.15	5.25	4.95	5.32	6.04	5.61	4.54	1.46
Mn	0.00	0.00	0.00	0.00	0.01	0.01	0.03	0.02	0.00
Mg	4.11	4.07	3.99	3.41	3.83	3.15	3.23	4.36	0.27
Ca	0.01	0.00	0.00	0.01	0.00	0.00	0.03	0.00	0.00
Na	0.00	0.01	0.01	0.01	0.00	0.01	0.01	0.04	0.00
K	0.00	0.00	0.00	0.01	0.00	0.02	0.04	0.01	0.00
Total	20.03	20.03	20.03	19.67	19.99	20.07	19.82	19.92	6.67

Chl_{cnt} = chlorite in contact with garnet; Chl_m = Main foliation; Ctd_m = matrix chloritoid; $^+$Composition for the thermobarometric analysis; Chlorite structural formula was recalculated on the basis of 28 O whereas 10 O was used for chloritoid.

Table 4-7. EPMA point analysis of representative samples for garnet-ilmenite thermometry.

Sample No	UM17152		UM1787				UM1789				UM1326	
Position	Ilm	Grt rim	Ilm	Grt core	Ilm	Grt rim	Ilm	Grt core	Ilm	Grt rim	Ilm	Grt mid
SiO2	0.02	37.58	0.03	37.19	0.06	36.59	0.04	37.16	0.04	37.65	0.09	37.20
TiO2	53.60	0.14	52.48	0.11	52.98	0.20	52.61	0.29	53.51	0.27	50.08	0.46
Al2O3	0.01	22.46	0.04	22.22	0.03	22.27	0.02	22.40	0.02	22.48	0.03	21.67
Cr2O3	0.03	0.00	0.01	0.02	0.01	0.00	0.02	0.00	0.02	0.00	0.01	0.03
FeO	48.34	35.10	48.24	37.99	48.00	37.86	47.06	31.07	47.09	33.68	49.69	32.47
MnO	0.02	0.10	0.31	1.93	0.49	2.12	1.27	6.26	0.74	2.72	0.41	2.79
MgO	0.51	2.14	0.31	1.64	0.03	1.75	0.22	1.36	0.04	1.66	0.34	1.55
CaO	0.03	5.25	0.00	1.83	0.00	1.82	0.01	4.28	0.01	4.98	0.02	5.99
Na2O	0.00	0.02	0.00	0.01	0.03	0.02	0.00	0.03	0.02	0.02	0.00	0.01
K2O	0.00	0.01	0.00	0.00	0.00	0.01	0.00	0.00	0.00	0.00	0.00	0.00
Total	102.54	102.79	101.41	102.93	101.63	102.65	101.25	102.86	101.50	103.45	100.67	102.18
Si	0.00	2.94	0.00	2.94	0.00	2.91	0.00	2.93	0.00	2.94	0.00	2.94
Ti	0.99	0.01	0.99	0.01	0.99	0.01	0.99	0.02	1.00	0.02	0.96	0.03
Al	0.00	2.07	0.00	2.07	0.00	2.09	0.00	2.08	0.00	2.07	0.00	2.02
Cr	0.00	0.00	0.00	0.00	0.00	0.00	0.00	0.00	0.00	0.00	0.00	0.00
Fe	0.99	2.30	1.01	2.51	1.00	2.52	0.98	2.05	0.98	2.20	1.06	2.15
Mn	0.00	0.01	0.01	0.13	0.01	0.14	0.03	0.42	0.02	0.18	0.01	0.19
Mg	0.02	0.25	0.01	0.19	0.00	0.21	0.01	0.16	0.00	0.19	0.01	0.18
Ca	0.00	0.44	0.00	0.15	0.00	0.15	0.00	0.36	0.00	0.42	0.00	0.51
Na	0.00	0.00	0.00	0.00	0.00	0.00	0.00	0.01	0.00	0.00	0.00	0.00
K	0.00	0.00	0.00	0.00	0.00	0.00	0.00	0.00	0.00	0.00	0.00	0.00
Total	2.01	8.02	2.01	8.01	2.01	8.04	2.01	8.02	2.00	8.01	2.04	8.02

Ilmenite structural formula was recalculated on the basis of 3 O.

4.6. Metabasic rocks of Munsiari formation (MCTZ)

Petrography and mineral chemistry

Sample UM1317

This sample is a fine-medium grained schistose amphibolite collected from the lower most structural level in the MCTZ (Figure 4.8a). This is composed mostly of aggregates of amphibole, plagioclase, quartz, biotite and minor epidote. There are two types of amphiboles categorized on the basis of the occurrence and composition. Amphibole is present as porphyroblast (P-Amp) which is surrounded by elongated prismatic matrix amphibole (M-amp). Both are compositionally calcic. M-amp and biotite define the schistosity (S_m). This sample is basically characterized by compositional layers developed by alternating layers of amiphiboles and quartzo-feldspathic domain. Chemical zoning is preserved in P-Amp. According to Leake *et al*. (1997), a rimward compositional change was encountered from actinolitic hornblende to ferrian tschermakitic hornblende (7.18 to 6.37 atoms per formula unit of Si). Whereas, M-amp also exhibits the composition towards ferrian tschermakitic hornblende.

Sample UM1316

This sample is non-schistose amphibolite collected from an exposure very close to UM1317 (Figure 4.8b, c and d). Mineral assemblage is mostly dominated by coarse grained amphibole (P-Amp; ~0.8 mm) along with very fine grained fraction (~10 µm) of quartz, plagioclase, epidote and minor titanite and ilmenite. Fine grained fraction is observed to be within the interstitial space between P-Amp aggregates. P-Amp are chemically zoned suggesting prograde metamorphism in terms of a rimward increase in $Al^{(T)}$ from 1.02 to 1.74 atoms per formula unit (*a.p.f.u)* . Patchy zonation can be seen among epidote grains suggesting the changes in Fe^{3+} content (Figure 4.8d; darker zone in BSE image indicating low Fe^{3+}). Whereas, polygonal grains of plagioclase with 120 ° triple junction (foam texture; Spry 1969; Kingery et al., 1976), also reveal chemical changes with a decrease of Si content from core to rim (Figure 4.8d).

Sample UM1746

This is the only metabasic rock sample that shows the occurrence of garnet porphyroblasts (Figure 4.8e). This is a non-foliated rock with the assemblage of amphibole, quartz and chlorite.

Plagioclase is absent. Garnet porphyroblast (~*463* µm in diameter) exhibits the signature of growth zoning (Figure 4.6h) with a rimward decrease in Mn from 0.25 to 0.11 *a.p.f.u* (core X_{mn} = 8.7%; rim X_{mn} = 3.5%). Composition of matrix amphiboles are calcic which further can be classified as ferri-tschermakite (Leake *et al*., 1997).

Sample UM17132A

This sample is a compact schistose amphibolite with very less quartzo-feldspathic fraction (Figure 4.8f). It contains the mineral assemblage of amphibole, quartz, plagioclase and ilmenite. Fine grained quartz is mostly abundant as inclusion in amphiboles. Amphiboles are dominantly tschermakite associated with minor ferrian-magnesio hornblende (Leake *et al*. 1997).

Sample UM17132B

This is a schistose amphibolite consisting amphibole, plagioclase, K-feldspar, quartz, epidote, sphene and minor biotite (Figure 4.8g). Schistosity is developed by the orientation of elongated amphiboles, which are compositionally known as tschermakitic hornblende. Quartz and feldspar aggregates constitute the microlithons. Epidote porphyroblasts are observed to be placed within the quartzo-feldspathic domain which locally produce pinch and swell structure (Figure 4.8g). Patchy chemical zonation is persistent in epidote porphyroblast due to heterogeneous distribution of Fe^{3+}. Few inclusions of amphibole is present in epidote porphyroblast. Albitic plagioclase around these porphyroblast contain exsolved phases of K-feldspar. A vein of K-feldspar with numerous euhedral crystals is present along the schistosity (Figure 4.8h).

Sample UM1759:

This is a massive non-foliated metabasic rock composed of amphibole, plagioclase, biotite and quartz (Figure 4.9i).

Sample UM1725

This sample has a porphyroblastic texture with a strong foliation characterized by alignment of the amphibole (Figure 4.9j and k). Thus, P-Amp is surrounded by the assemblage containing stretched M-amp, plagioclase, quartz, epidote and elongated clusters of titanite grains. Modal abundance of epidote is relatively higher in this sample. Some P-amp are partially replaced by polycrystalline

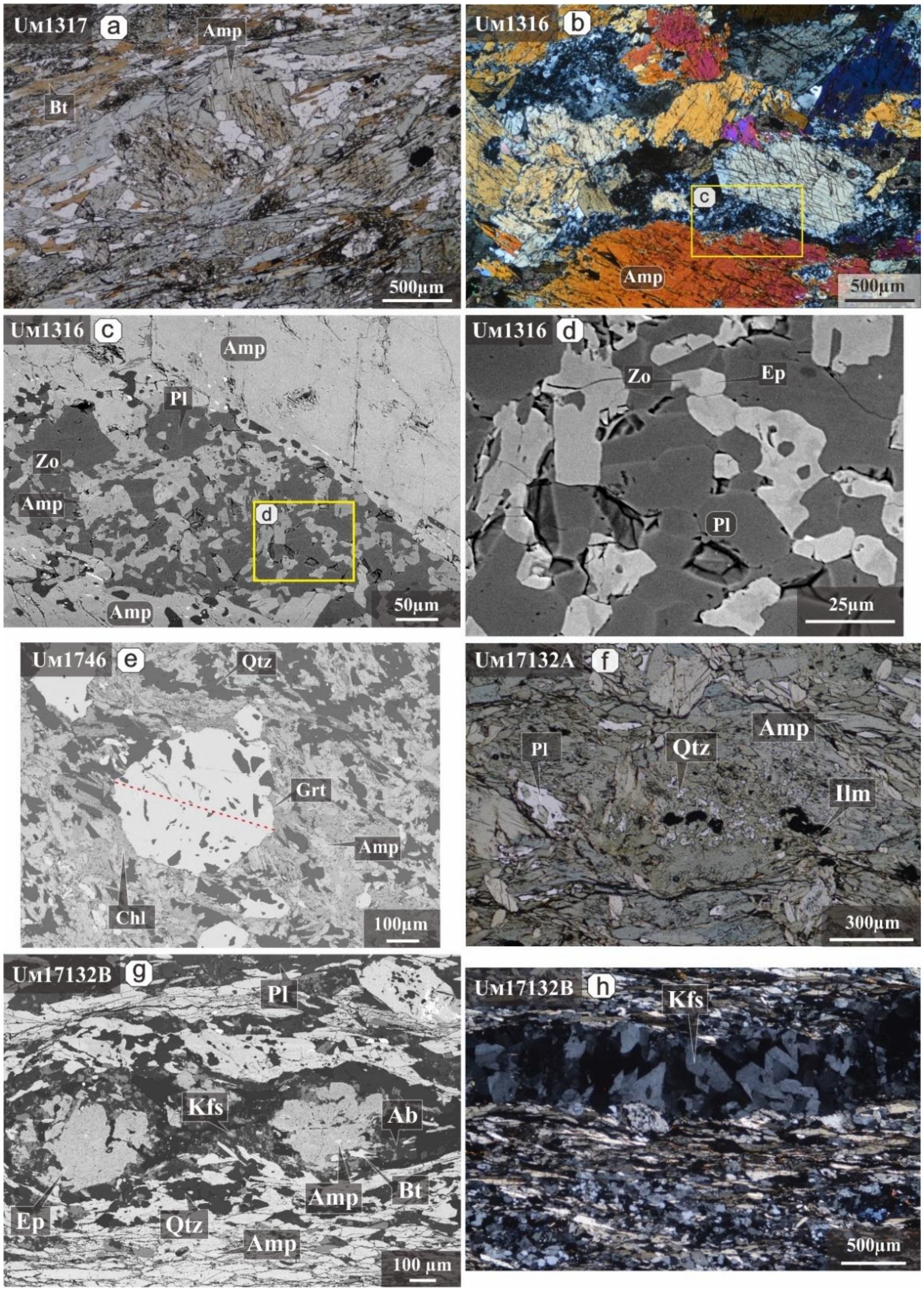

Figure 4.8. Representative microstructures of the metabasic rocks from the Munsiari Formation (MCTZ).

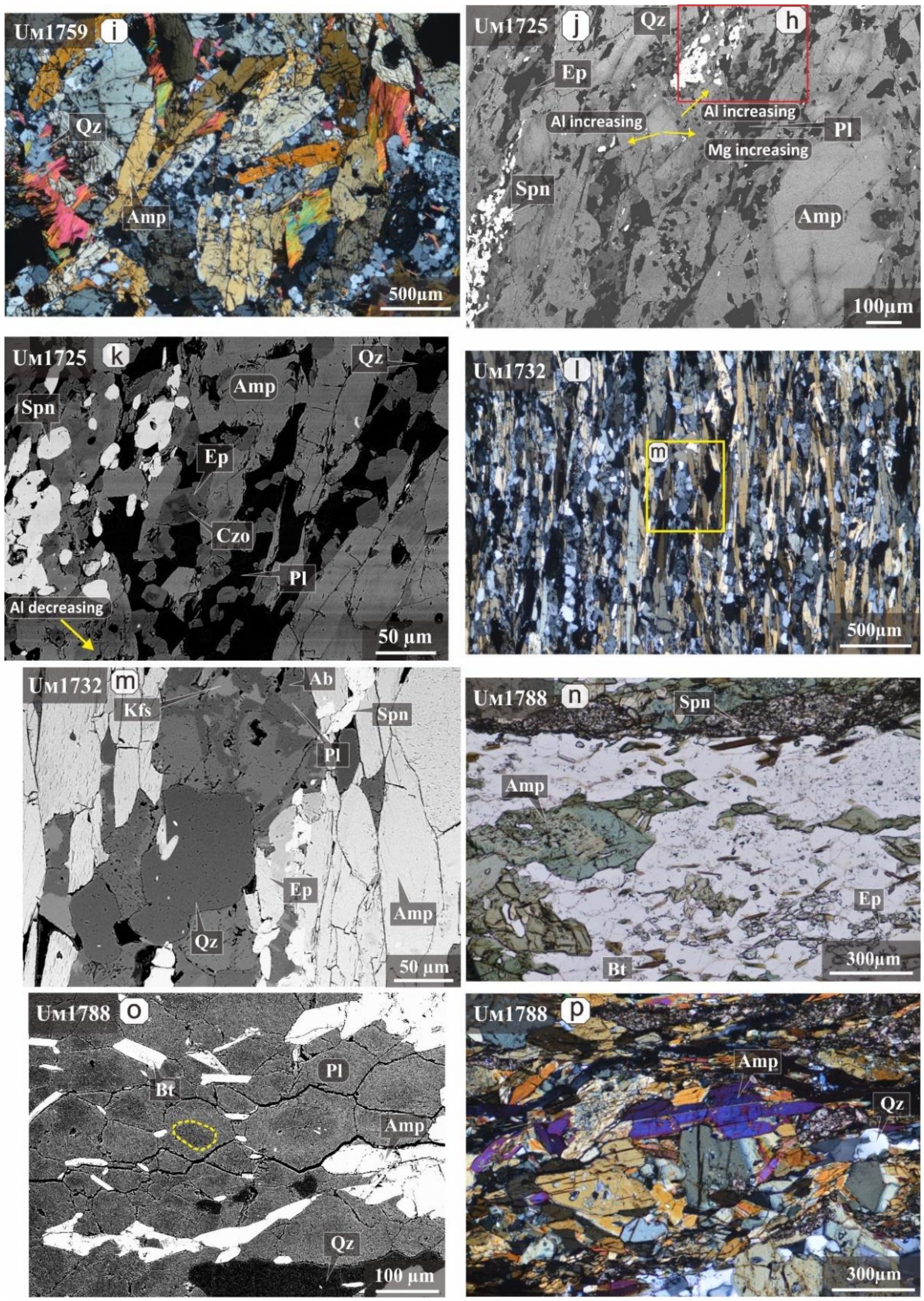

Figure 4.9. Representative microstructures of the metabasic rocks from the Munsiari Formation (MCTZ).

aggregates of epidote. Strong prograde zoning has been developed in P-Amp by means of increasing $Al^{(T)}$ content from 0.90 to 1.63 *a.p.f.u.* towards rim, whereas other part of the same grain has zoning generated by an increase of Mg content towards rim with constant Al content (Figure 4.9j). M-Amp and rim are charecterised by teschermakitic hornblende whereas core is classified as ferrian- magnesio hornblende (Leake et al., 1997). Distinct zoning is also present in epidote (Figure 4.9k) where Fe^{3+} increases towards rim indicating isostructural cation exchange between Al-Fe^{3+} (Enami and Banno, 1980).

Sample UM1732:

This metabasic sample shows closely spaced disjunctive foliation (Figure 4.9l) defined by the orientation of fine grained amphibole (~170 µm in length). Microlithons are characterized by very thin domain (~80 µm grain size) of quartzo-feldspathic aggregates. The mineral assemblage is amphibole, plagioclase, K-feldspar, quartz, sphene and epidote. Plagioclase (An_{23}) is dissolved and overgrown by albitic mantle (An_5) (Figure. 4.9m). On the other hand, K-feldspar intergrowth is also found to be developed within the albite (Figure 4.9m). Amphiboles are classified as tschermakitic hornblende.

Sample UM1788:

This sample is a schistose metabasic rock with alternating layers of elongated amphiboles and quartzo-feldspathic domain, which define the main foliation. Sampling has been done from structurally highest part of the MCTZ. The mineral assemblage is amphibole, plagioclase, quartz, sphene, epidote and biotite (Figure 4.9n). Quartzo-feldspathic layers are relatively thicker than other samples. P-Amp shows zoning pattern (Figure 4.9n) as same as other samples (UM1717, UM1316 and UM1725) which is embedded in M-Amp as well as quartzo-feldspathic matrix. Discrete flakes of biotite are observed to be aligned with the foliation. Clusters of sphene are dispersed with M-Amp. Fine-grained epidotes are mostly present in quartzo-feldspathic domain. Characteristics of plagioclase is as same as sample UM1316 (Figure 4.9o) but the size is relatively coarser (~120 µm). Zoning is marked by detecting Si-rich core and Ca-rich rim.

All amphibole compositions are summarized in the Table 4-8 and plotted in the scatter diagrams shown in the Figure 4.10.

Table 4-8. EPMA analysis of amphiboles of MCTZ metabasic rocks. The classification of amphiboles is based on Leake et al. (1997, 2004).

Samples	UM1717				UM1316		UM1746				UM17132A			UM132B				
Positions	core	rim	core	rim	core	Amp rim*	Amp	Amp	Grt core	Grt rim	Amp rim*	core	Amp	core	rim	Amp	Amp	Amp
SiO2	50.39	44.66	49.48	43.12	47.89	42.66	39.73	41.45	36.92	36.17	40.16	39.60	45.42	47.43	51.29	43.37	45.32	42.46
TiO2	0.14	0.34	0.10	0.28	1.17	0.35	0.28	0.38	0.07	0.04	0.53	0.31	0.19	0.33	0.04	2.46	0.34	0.41
Al2O3	6.00	11.75	4.45	13.05	6.83	15.43	17.33	14.32	22.29	22.40	15.22	20.80	9.99	10.29	4.38	11.64	11.77	14.70
FeO	13.63	15.51	13.42	16.17	16.27	15.75	19.99	20.12	31.34	33.97	18.15	14.52	17.63	15.40	13.15	15.43	15.41	16.10
MnO	0.25	0.30	0.26	0.26	0.23	0.30	0.16	0.16	3.78	1.64	0.27	0.33	0.30	0.23	0.30	0.25	0.33	0.31
MgO	14.05	11.51	15.69	10.45	12.43	9.40	6.74	7.90	1.61	2.08	7.55	4.74	10.60	11.45	15.05	9.51	11.23	9.51
CaO	11.75	11.18	11.89	11.45	11.30	11.54	10.99	10.83	6.37	5.55	11.29	15.11	11.44	11.77	12.15	12.75	11.50	11.72
Na2O	0.69	1.15	0.41	1.34	0.86	1.51	1.41	1.21	0.02	0.00	1.46	1.00	1.03	0.96	0.38	1.08	1.02	1.32
K2O	0.13	0.32	0.14	0.37	0.40	0.45	0.47	0.27	0.01	0.00	0.70	0.42	0.46	0.33	0.15	0.39	0.48	0.77
Total	97.03	96.72	95.83	96.48	97.38	97.39	97.09	96.64	102.40	101.86	95.33	96.83	97.04	98.19	96.89	96.87	97.40	97.30
Si	7.27	6.51	7.18	6.37	6.98	6.26	5.92	6.17	2.91	2.87	6.13	5.94	6.70	6.85	7.39	6.51	6.59	6.27
Al iv	0.73	1.49	0.76	1.63	1.02	1.74	2.08	1.83	0.09	0.13	1.87	2.06	1.30	1.15	0.61	1.49	1.41	1.73
Al vi	0.29	0.53	0.00	0.64	0.16	0.93	0.96	0.68	1.99	1.97	0.87	1.62	0.44	0.61	0.14	0.57	0.61	0.83
Ti	0.02	0.04	0.01	0.03	0.13	0.04	0.03	0.04	0.00	0.00	0.06	0.03	0.02	0.04	0.00	0.28	0.04	0.05
Fe3+	0.56	1.00	1.03	0.85	0.75	0.58	1.05	1.21	0.01	0.02	0.62	0.00	0.83	0.49	0.57	0.00	0.76	0.57
Fe2+	1.08	0.89	0.60	1.14	1.23	1.35	1.44	1.29	2.06	2.24	1.70	1.82	1.35	1.37	1.02	1.94	1.12	1.41
Mn	0.03	0.04	0.03	0.03	0.03	0.04	0.02	0.02	0.25	0.11	0.04	0.04	0.04	0.03	0.04	0.03	0.04	0.04
Mg	3.02	2.50	3.39	2.30	2.70	2.06	1.50	1.75	0.19	0.25	1.72	1.06	2.33	2.47	3.23	2.13	2.44	2.09
Ca	1.82	1.75	1.85	1.81	1.77	1.82	1.75	1.73	0.54	0.47	1.85	2.43	1.81	1.82	1.88	2.05	1.79	1.85
Na	0.19	0.32	0.11	0.38	0.24	0.43	0.41	0.35	0.00	0.00	0.43	0.29	0.29	0.27	0.11	0.31	0.29	0.38
K	0.02	0.06	0.02	0.07	0.07	0.08	0.09	0.05	0.00	0.00	0.14	0.08	0.09	0.06	0.03	0.07	0.09	0.14
Total	15.03	15.13	14.99	15.26	15.08	15.33	15.25	15.13	8.04	8.07	15.41	15.37	15.19	15.15	15.01	15.38	15.17	15.38
Amphibole classification	Actinolitic hornblende	Ferri-magnesio hornblende	Ferri-magnesio hoenblende	Ferrian tschermakitic hornblende	Ferri-magnesio hoenblende	Tschermakitic Hornblende	Ferri-tschermakite	Ferri-tschermakite			Tschermakite	Alumino ferro tschermakite	Ferrian-Magnesio Hornblende	Magnesio hornblende	Actinolitic hornblende	Titanian-magnesio hornblende	Ferrian magnesio hornblende	Tschermakitic hornblende

Samples	UM1725			UM1759				UM1732		UM1788			1794	17120
Positions	core	rim	Amp*	Amp*	Amp	Amp	Amp	rim	core	Amp*	Amp	Amp	Amp	Amp
SiO2	47.60	43.15	42.46	43.64	49.86	43.13	40.35	42.36	45.63	42.16	49.35	42.58	39.00	41.62
TiO2	0.57	0.32	0.36	0.54	0.29	0.52	0.24	0.47	0.31	0.47	0.30	0.37	0.51	1.38
Al2O3	5.11	13.90	15.88	12.19	8.24	15.06	22.70	14.02	9.74	13.15	6.02	13.61	14.55	13.09
FeO	17.12	15.11	15.21	16.44	12.00	14.75	10.44	16.56	15.26	17.66	15.68	18.18	17.21	15.01
MnO	0.32	0.32	0.28	0.33	0.22	0.36	0.22	0.28	0.29	0.25	0.29	0.29	0.23	0.21
MgO	12.51	10.33	9.37	9.75	14.14	9.57	2.38	9.59	11.72	9.48	13.26	9.12	8.49	10.06
CaO	11.90	11.69	11.59	11.02	11.77	11.64	19.15	11.86	12.32	11.53	12.05	11.65	11.70	12.42
Na2O	0.62	1.22	1.41	1.35	0.69	1.26	0.30	1.22	0.73	1.44	0.69	1.46	1.42	1.15
K2O	0.36	0.48	0.70	0.24	0.20	0.32	0.09	0.81	0.48	0.85	0.38	0.65	2.13	1.40
Total	96.10	96.51	97.26	95.51	97.42	96.61	95.88	97.17	96.48	96.99	98.01	97.91	95.22	96.33
Si	7.09	6.37	6.25	6.43	7.12	6.36	6.01	6.28	6.75	6.29	7.15	6.29	6.05	6.31
Al iv	0.90	1.63	1.75	1.57	0.88	1.64	1.99	1.72	1.25	1.71	0.85	1.71	1.95	1.69
Al vi	0.00	0.79	1.00	0.98	0.50	0.98	1.99	0.74	0.45	0.60	0.17	0.66	0.71	0.64
Ti	0.06	0.04	0.04	0.06	0.03	0.06	0.03	0.05	0.03	0.05	0.03	0.04	0.06	0.16
Fe3+	0.75	0.64	0.49	0.41	0.49	0.45	0.00	0.60	0.51	0.74	0.62	0.73	0.38	0.10
Fe2+	1.38	1.23	1.38	1.26	0.94	1.37	1.30	1.46	1.38	1.46	1.28	1.52	1.86	1.81
Mn	0.04	0.04	0.03	0.03	0.03	0.05	0.03	0.04	0.04	0.03	0.04	0.04	0.03	0.03
Mg	2.78	2.27	2.05	2.26	3.01	2.10	0.53	2.12	2.59	2.11	2.86	2.01	1.96	2.27
Ca	1.90	1.85	1.83	1.80	1.80	1.84	3.05	1.89	1.95	1.84	1.87	1.84	1.95	2.02
Na	0.18	0.35	0.40	0.41	0.19	0.36	0.09	0.35	0.21	0.42	0.19	0.42	0.43	0.34
K	0.07	0.09	0.13	0.07	0.04	0.06	0.02	0.15	0.09	0.16	0.07	0.12	0.42	0.27
Total	15.15	15.29	15.36	15.27	15.03	15.26	15.03	15.39	15.25	15.42	15.13	15.38	15.79	15.62
Amphibole classification	Ferrian magnesio hornblende	Tschermakitic hornblende	Tschermakite	Magnesio hornblende	Magnesio hornblende	tschermakitic hornblende	Alumino-ferro tschermakite	Tschermakitic hornblende	Magnesio hornblende	Tschermakitic hornblende	Magnesio hornblende	Tschermakitic hornblende	Potasian ferroan pargasite	Potasian ferroan pergasitic hornblende

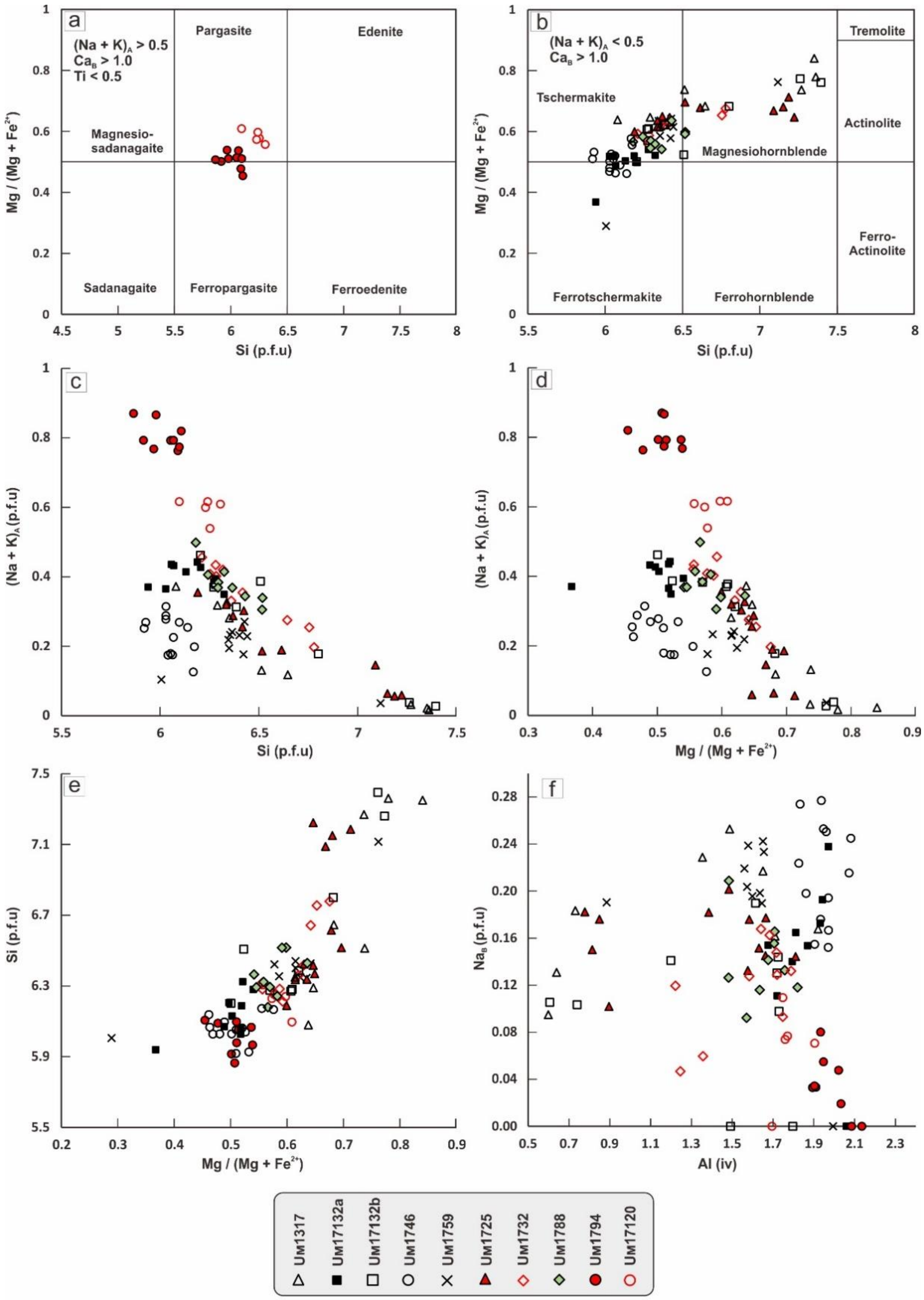

Figure 4.10. Compositional diagrams for amphiboles in metabasic rocks. (a, b) Amphiboles are classified on the basis of the classification scheme of Leake et al. (1997, 2004); (a) amphiboles from L-GHS where $(Na+K)_A > 0.5$; (b) amphiboles from the Munsiari Formation where $(Na+K)_A > 0.5$. (c) $(Na+K)_A$ v. Si plot. (d) $(Na+K)_A$ v. $Mg/Mg+Fe^{2+}$ plot. (e) Si v. $Mg/Mg+Fe^{2+}$ plot. (f) Na_B v. Al (iv) (Miyashiro plot).

4.7. Results

4.7.1. Geothermobarometry

P-T results are documented in this section to show the results of the thermobarometric analysis performed by assuming Fe^{2+} cation present in the matrix phases. All results obtained from metapelites and pelitic gneiss are summarized in the Table 4-9 and plotted in the Figure 4.11 to exhibit the variation in *P-T* conditions across the MCT. Plagioclase compositions for amphibole-plagioclase thermobarometry are given in the Table 4-10 and the P-T results are provided in the Table 4-11. Results from garnet-hornblende thermometer are recorded in the Table 4-12.

Munsiari formation (MCTZ) samples

Two samples from the lower Munsiari Formation (close to the Munsiari thrust), UM1755 and UM1757, yield peak temperature of 485±25 and 521±25 °C respectively obtained from GB thermometry (Holdaway, 2000). By applying GBMP barometer, pressure of 5.8±1.2 is estimated only for UM1757 as sample UM1755 is devoid of plagioclase. This pressure was taken to estimate the peak temperature for the sample UM1755. Ti-in-biotite thermometry is only applicable for these two samples since the calibration can be employed for those metapellites equilibrated within 3 to 6 kbar pressure (Henry et al., 2005). As a result, peak-T of 535.8±35.8 and 526.6±25 °C are obtained for the sample UM1755 and UM1757 respectively. On the other hand, Average *P-T* method by using the software Thermocalc 3.33 (Powell & Holland, 1994; Holland & Powell, 1998) estimates the peak-*T* of 554±25 °C and pressure of 5.5±1.5 kbar. Sample UM17152 (biotite absent) located in the middle of Munsiari Formation, experienced peak temperatures of about 574±32 °C and pressure at that temperature of about 8.7±1.1 kbar (average P-T result). This result can be supported by the result of garnet-ilmenite thermometry where the composition of ilmenite inclusion near garnet rim together with the garnet composition yields peak temperature of about 584.7±45.3 °C (pressure independent). Due to absence of plagioclase in the sample UM1787 (upper Munsiari formation), it only yields temperature estimations of about 633±25 °C (assuming 8 kbar pressure; change in 1 kbar pressure corresponds to a change in temperature of 3 °C) and 655.3±57 °C (pressure independent) obtained by applying GB and garnet-ilmenite thermometry respectively. Earliest growth history of garnet at the temperature of 512.5±35 °C, was evaluated using ilmenite inclusion at the core. Two samples from the upper part of Munsiari Formation, UM1789 and UM1326 (close to the MCT), record peak temperature of 576±25 and 594±19 °C respectively and the pressures at that temperatures are of 8±1.5 kbar and 9.4±1 kbar respectively (average *P-T* method). Sample UM1789 is also taken for garnet-ilmenite thermometry, record peak temperature of 665.5±35 °C which is much higher than the result obtained from average P-T method. Whereas, the result from garnet-biotite thermometry and GBMP barometer for the sample UM1326 (578.6±25 °C, 8.5±1.2 kbar), supports the result of average *P-T* estimation**.**

In the case of metabasic rocks, sample UM1316 close to the Munsiari thrust, was metamorphosed at 636.75±36.3 °C and 8-11 kbar whereas other samples (UM17132A, UM1759 and UM1725) from lower Munsiari formation yield peak-*T* of 681.8±25 to 696.5±22.3 °C and show an increasing trend of pressure from 8 to 13 kbar. Sample from upper Munsiari formation (UM1788) was equilibrated at 679±14 °C and 7-8 kbar.

Lower GHS samples

Sample UM1325, a migmatitic gneiss immediately above the MCT, exhibits a sharp increase in both peak temperature and pressure at that temperature up to 683±25 °C and 11 kbar respectively (GB thermometer and GBMP barometer). A trend of increasing P-T condition has been developed in L-GHS where other samples (UM1322, 1407, 17131, 17129) experienced peak temperature ranging from 697±25 to 806±25 °C and 723±43 to 821±52 °C (towards structural high) obtained from GB thermometer and average *P-T* estimation. Whereas, pressure at peak temperatures varies from 10.4±1.2 to 11.8±1.2 kbar and 11.8±1.5 to 13.4±1.7 kbar (towards structural high) estimated by GBMP barometer and average P-T method. Sample UM17119 (kyanite-bearing gneiss), structurally higher most sample, records peak temperature of 713±25 °C (GB thermometer) and pressure of 8.9±1.8 (GBAQ barometer) which further produce a decline in metamorphic P-T condition towards structural high.

Hornblende-plagioclase thermometer, less dependent on pressure, is applied only for two samples in L-GHS (UM1794 and UM17120). It is observed that peak metamorphic temperature increases from 662.5±21.4 (UM1794) to 796±17.4 °C (UM17120).

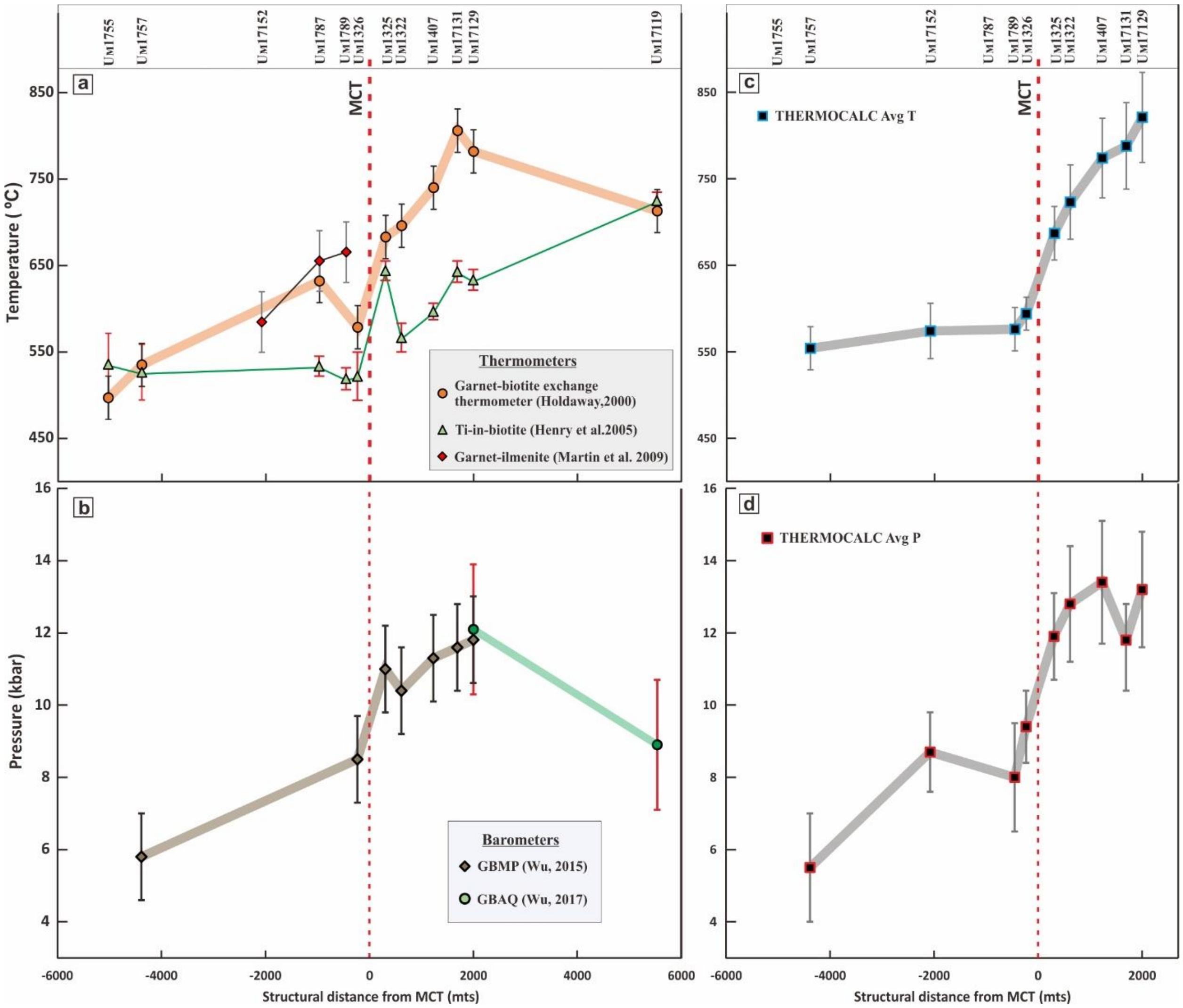

Figure 4.11. Results of thermobarometric analysis showing the distribution of peak metamorphic temperatures and pressures at peak-*T* across the MCT. (a) Calculated temperatures using garnet-biotite and garnet-ilmenite exchange thermometers. Temperatures obtained from Ti-in-biotite thermometer are also plotted; (b) Results of pressures acquired by using GBMP and GBAQ barometer; (c, d) Results of THERMOCALC average *P-T* estimation.

Table 4-9. Summary of P-T results obtained from the MCTZ metapelites and L-GHS pelitic gneiss.

Methods	Garnet-Biotite Holdaway, 2000		Garnet-Ilmenite Martin et al., 2009		Ti-in-Biotite Henry et al., 2005	Ti-in-Muscovite Wu & Chen, 2015	GBMP Wu, 2015		GBAQ Wu, 2017		Thermocalc Average PT estimation						Garnet diameter
Samples	T (°C) [SD ±25 °C]		T (°C) [SD ±35 °C]		T (°C) [SD ±24 °C]	T (°C) [SD ±65 °C]	P (kbar) [SD ±1.2 kbar]		P (kbar) [SD ±1.8 kbar]		*T* (°C)	1σ	P (kbar)	1σ	Cor.	σ_{fit}	(µm)
	Fe^{3+}	Fe^{2+}	Rim	Core			Fe^{3+}	Fe^{2+}	Fe^{3+}	Fe^{2+}							
Munsiari/MCTZ																	
UM1755	485	497			535.8 ±35.8 **(4)**												3381
UM1757	521	535			526.6 ±32.2 **(10)**		5.7	5.8			554	25	5.5	1.5	0.458	2.37	1057.26
UM17152			584.7 ±10.3 **(2)**								574	32	8.7	1.1	0.554	1.66	2586.22
UM1787	610	632	655.3 ±22.3 **(3)**	512.5													1427
UM1789			665.5	527.7							576	25	8	1.5	0.428	2.05	733
UM1326	561.7	578.6	438.2 (mid)				8.3	8.5			594	19	9.4	1	0.536	1.43	366, 408.15
L-GHS																	
UM1325	658	683					10.6	11			687	31	11.9	1.2	0.668	1.25	2482
UM1322	671	696					10.1	10.4			723	43	12.8	1.6	0.784	1.44	1033, 927
UM1407	712	740					11	11.3			774	46	13.4	1.7	0.763	1.43	3007, 2300
UM17131	768	806					11.2	11.6			788	50	11.8	1.5	0.682	1.38	1108
UM17129	748	782				697 ±76.8 **(10)**	11.4	11.8	10.8	12.1	821	52	13.2	1.6	0.698	1.32	1127
UM17119	680	713							8.2	8.9							2477

Table 4-10. EPMA point analysis of plagioclase for amphibole-plagioclase thermobarometry.

Samples	UM1759	UM1316	UM17132A	UM1725		UM1788
SiO2	59.59	61.15	60.23	58.52	59.15	60.68
TiO2	0.00	0.00	0.00	0.00	0.00	0.00
Al2O3	25.47	24.18	23.26	25.12	25.35	24.17
FeO	0.07	0.04	0.20	0.20	0.18	0.27
MnO	0.00	0.01	0.00	0.02	0.03	0.00
MgO	0.01	0.00	0.01	0.02	0.00	0.00
CaO	7.32	5.83	5.26	6.90	7.71	5.24
Na2O	6.31	9.74	9.08	7.75	8.38	8.58
K2O	0.08	0.07	0.07	0.14	0.09	0.14
Total	98.85	101.02	98.11	98.67	100.88	99.06
Si	2.67	2.71	2.73	2.65	2.63	2.72
Ti	0.00	0.00	0.00	0.00	0.00	0.00
Al	1.35	1.26	1.24	1.34	1.33	1.28
Fe	0.00	0.00	0.01	0.01	0.01	0.01
Mn	0.00	0.00	0.00	0.00	0.00	0.00
Mg	0.00	0.00	0.00	0.00	0.00	0.00
Ca	0.35	0.28	0.26	0.33	0.37	0.25
Na	0.55	0.84	0.80	0.68	0.72	0.75
K	0.00	0.00	0.00	0.01	0.00	0.01
Total	4.93	5.08	5.05	5.05	5.05	5.05

Table 4-11. Results of amphibole-plagioclase thermometry.

Samples	UM1316	UM132A	UM1759	UM1725	UM1788
Temperature (°C) (Holland and Blundy, 1994)	636.75 ± 36.31	681.75 ± 24.96	696.5 ± 22.25	685.33 ± 18.02	679 ± 14
Pressure (kbar) (Molina et al., 2015)	8 to 11	8 to 11	11 to 12	12 to 13	7 to 8

Table 4-12. EPMA point analysis of garnet and amphibole and the results of garnet-hornblende thermometry.

Samples	UM1746		UM1794		UM120	
No.	Grt rim	Amp	Grt rim	Amp	Grt core	Amp
SiO2	36.49	39.73	37.37	36.92	37.27	41.62
TiO2	0.02	0.28	0.06	0.56	0.07	1.38
Al2O3	22.52	17.33	20.32	14.80	21.10	13.09
Cr2O3	0.04	0.04	0.14	0.07	-0.01	0.15
FeO	33.38	19.99	20.79	17.68	22.86	15.01
MnO	1.69	0.16	1.71	0.23	1.99	0.21
MgO	2.06	6.74	1.84	8.10	4.30	10.06
CaO	5.92	10.99	16.50	11.77	11.72	12.42
Na2O	0.02	1.41	0.00	1.34	0.05	1.15
K2O	0.00	0.47	-0.01	2.25	0.03	1.40
Total	102.13	97.13	98.72	93.72	99.37	96.48
Si	2.89	5.92	2.98	5.86	2.94	6.31
Al iv	0.11	2.08	0.02	2.14	0.06	1.69
Al vi	1.99	0.96	1.89	0.64	1.90	0.64
Ti	0.00	0.03	0.00	0.07	0.00	0.16
Cr	0.00	0.00	0.00	0.00	0.00	0.00
Fe3+	0.01	1.05	0.09	0.49	0.08	0.10
Fe2+	2.20	1.44	1.29	1.86	1.43	1.81
Mn	0.11	0.02	0.12	0.03	0.13	0.03
Mg	0.24	1.50	0.22	1.92	0.50	2.27
Ca	0.50	1.75	1.41	2.00	0.99	2.02
Na	0.00	0.41	0.00	0.41	0.00	0.34
K	0.00	0.09	0.00	0.46	0.00	0.27
Total	8.06	15.25	8.03	15.87	8.04	15.62
Temperature T (°C) (Ravna, 2000)	344.28 (4) ±29.16		662.54 (6) ±21.38		796.02 (2) ±17.43	

4.8. Discussions and conclusions

4.8.1. Recognition of the MCT

It is difficult to define the upper boundary of the Munsiari formation (MCTZ) in the field because the Vaikrita Thrust is structurally not well defined. However, the basal part of the GHS, which forms the hanging wall of the Vaikrita Thrust, is distinguished from the MCTZ by the following petrographic features in pelitic rocks: (i) first appearance of microscopic needles of kyanite; (ii) subhedral-to-euhedral garnet porphyroblasts with random inclusion pattern and non-rotational growth history, which contrast with the anhedral-to-subhedral garnet porphyroblasts in MCTZ rocks with spiral inclusion trails; and (iii) chemically homogeneous garnet porphyroblasts except for a thin Mn-rich rim; this contrasts with the growth-zoned garnets in MCTZ rocks with a strong fractionation of Mn into core regions. The boundary delineated between the MCTZ and GHS based on these criteria is consistent with the Nd isotopic boundary defined by Ahmad et al. (2000).

4.8.2. P-T condition of metamorphism

The P–T conditions obtained from garnet-biotite thermometry and GBMP barometer for the Munsiari formation samples fall in the ranges of 5.7-8.3 kbar and 485-610 °C, while those for the L-GHS samples are 10.6 – 11.4 kbar and 658-768 °C (Fig. 4.11). By applying Thermocalc average P-T estimation, it is noticed that the Munsiari formation samples experienced P-T condition of 5.5 – 9.4 kbar and 658-768 °C, whereas the L-GHS samples experienced P-T condition of 11.9 – 13.2 kbar and 687-821 °C. Therefore, the results from both the methods show that there is an increase in P–T conditions of metamorphism in the L-GHS compared with those in the Munsiari formation. Peak-temperatures from garnet-biotite thermometry as well as average P-T, clearly show that there is a break exists in between the highest T values from the Munsiari formation and the lowest T values from the GHS. Similar observation has been marked for the pressure values obtained from the average P-T estimation. Hence, this indicates the presence of a discontinuity across the contact between the Munsiari formation and L-GHS. However, the results obtained from GBMP barometer show that the highest P values from the MCTZ overlap with the lowest P values from the HHCS within error. The discrepancy between the results of the two methods reflects the fact that different activity–composition models were used in used in average P-T estimation. The results reveal continuity but inverted metamorphism in both P and T between the MCTZ and the lowermost HHCS, where P and T peak and then decrease up-section in higher structural levels of the HHCS unit.

4.8.3. Inverted metamorphic field gradient and tectonic thinning process

Pressure difference between lowest and highest pressure (5.7 ±1.2 to 8.3 ±1.2 kbar; GBMP result) in the Munsiari formation is documented from about 4.1 km of strata which corresponds to a metamorphic pressure gradient of 0.62 kbar/km which is ~ 2 times higher than lithostatic pressure gradient (0.27kbar/km). In several places across the orogen, peak pressures collected through thick sections of Greater Himalayan rocks define upright, super-lithostatic field gradients that have been interpreted as the result of distributed, post–peak metamorphic thinning (Corrie et al., 2012; Larson et al., 2010). Tectonic thinning within mid-crustal Greater Himalayan rocks between the MCT and South Tibetan detachment system (STDS) locally resulted in decompression (e.g. Larson et al., 2010). Transport-parallel stretching along and above the MCT (e.g., Long et al., 2016, 2017) likely contributed displacement southward into an early, brittle foreland fold-thrust belt, which has now been removed by erosion. Tectonic thinning also explains the development of ubiquitous thrust-subparallel foliations and transport parallel stretching lineations within exhumed metamorphic terranes (e.g., Ring et al., 1999). In the Munsiari formation there are some locations where we observed the occurrence of normal faults. These extensional feature (Figure 3.5k) in a compressional thrust tectonic setting could be explained by the post-metamorphic thinning process.

Chapter 5

Microstructural Analysis of Quartz in Monomineralic and Polyphase domains: A case study from Main Central Thrust (MCT) Zone Mylonites, western Himalaya, India

5.1. Introduction

Deformational behavior of quartzo-feldspathic aggregate in response to ductile deformation within a shear zone, is an intriguing research topic in terms of thrust tectonics. Crustal scale thrusting in the Himalayan orogeny contribute to preserving the evolutionary history of naturally deformed rock bodies. Understanding the intracrystalline deformation of quartz and feldspars is fundamental to perceive the ideas of the research work on the parameters that controls the strain localization processes during the development of a shear zone. Numerous microstructural studies works has been performed on the monomineralic aggregates of quartz to investigate the deformation mechanism in synthetic samples (e.g.Griggs and Blacic, 1964, 1965; Griggs, 1967; McLaren et al., 1983, 1989; Jaoul et al., 1984; Post and Tullis, 1998; Stipp et al., 2006; Stipp and Kunze, 2008) as well as natural samples (e.g., Weathers et al., 1979; Law, 1986; Stipp et al., 2002). Deformation in monomineralic fraction leads to the recrystallization processes controlled by the grain-size-insensitive (GSI) dislocation creep (e.g., Hirth et al., 2001; Stipp et al., 2002; Behr and Platt, 2011; Kidder et al., 2012). Microstructural observations of shear zones in nature and experimental investigations of monomineralic systems in the laboratory have demonstrated that the evolution of a ductile fault rock through the mylonite series can entail a switch from a dislocation creep-controlled (grain-size-insensitive, GSI) to a diffusion creep-controlled (grain-size-sensitive, GSS) bulk rheology (e.g. Etheridge and Wilkie, 1979; Poirier, 1980; Kilian et al., 2011). Whereas, in the case of polymineralic aggregates, the strain localization process largely promotes GSS creep by diffusion creep with grain boundary sliding (Boullier and Gueguen, 1975; Stünitz and Fitz Gerald, 1993; Fliervoet et al., 1997; Kruse and Stünitz, 1999; Mehl and Hirth, 2008; Kanagawa et al., 2008).

In the Himalayas, previous studies examined the nature of strain including quartz textures, c-axis fabrics and vorticity in proximity to the top-to-the south-sense Main Central thrust (Jessup et al., 2006; Larson and Godin, 2009; Law et al., 2013; Frassi, 2015). These studies have demonstrated that deformation temperatures and differential stress vary systematically with distance from these structures with an inverse relationship of increasing temperature and decreasing differential stress farther away (Law et al., 2004, 2011, 2013; Frassi, 2015). Whereas, in the recent studies on monomineralic rock of the Main Central Thrust Zone (MCTZ), much

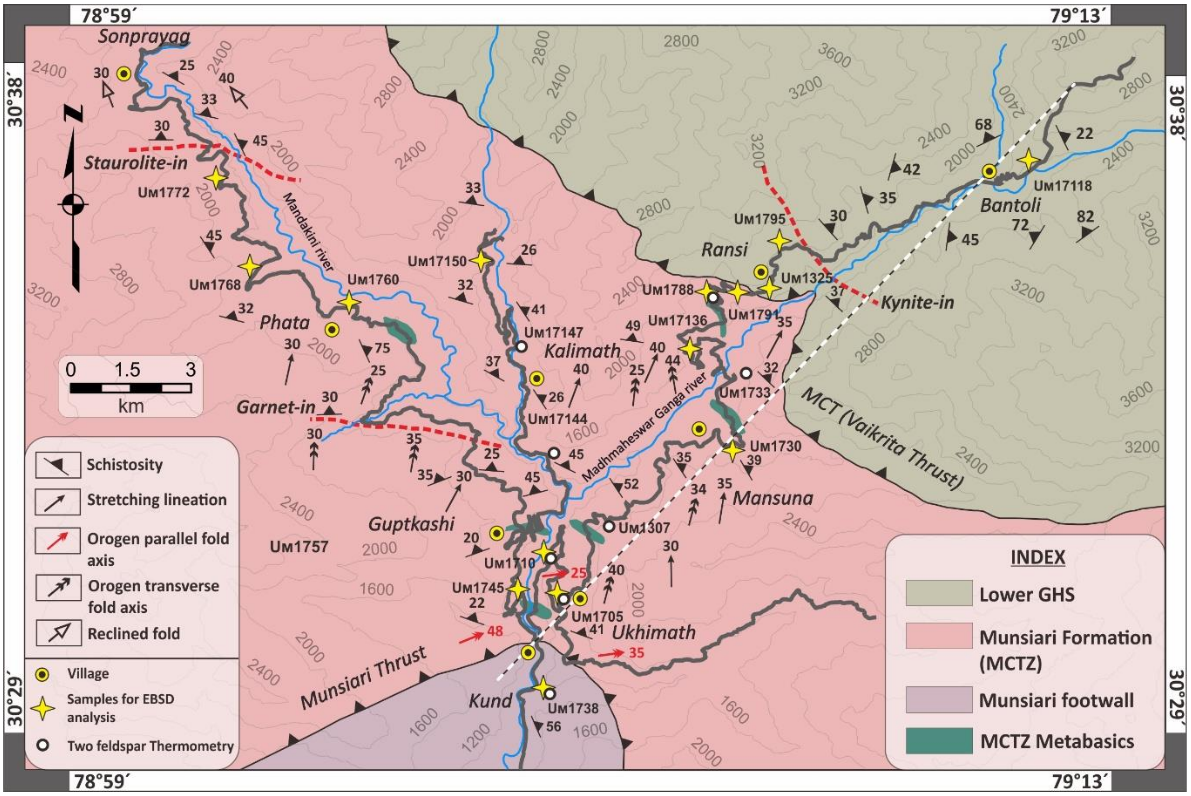

Figure 5.1. Geological map of western Himalaya along Mandakini river and Madhmaheswar river valley, Uttarakhand, India. The location of the study area is marked in Figure 2.1a. Attitudes of schistosity, mineral stretching lineation and folds are shown using different symbols. The Locations of the samples for EBSD analysis and 2-feldspar thermometry are shown with different symbols. Dashed line AB represents the line along which the cross section profile of the study area is drawn.

attention has been paid to define the shear zone boundary by means of strain localization processes inferred from the fabric strength parameters of quartz lattice preferred orientation (LPO) fabric (Larson, 2017; Hunter et al., 2018; Starnes et al., 2020).

There are very less studies done on polymineralic rocks of the Himalayas where they put emphasis only on the microstructural attributes of quartz within a polymineralic domain of granitic gneiss (Hunter et al., 2018). In addition, it is also noteworthy to analyze the quartz rich zones of the same sample to get a cumulative idea on how a polymineralic rock reacts while it is subjected to an external stress field. Hence, the present study aims to examine the quartz rich domain as well as the polymineralic fractions in mylonitic granitic gneiss of the Munsiari formation (MCTZ).In Himalayas, this study is the first attempt to investigate the quartz rich and polyphase domains from individual sample by considering different parameters such as effect of temperature, coaxial and non-coaxial deformation, water content and secondary mineral fraction. In particular, this study intends to expand the knowledge on difficulties arising from the shear zone rocks.

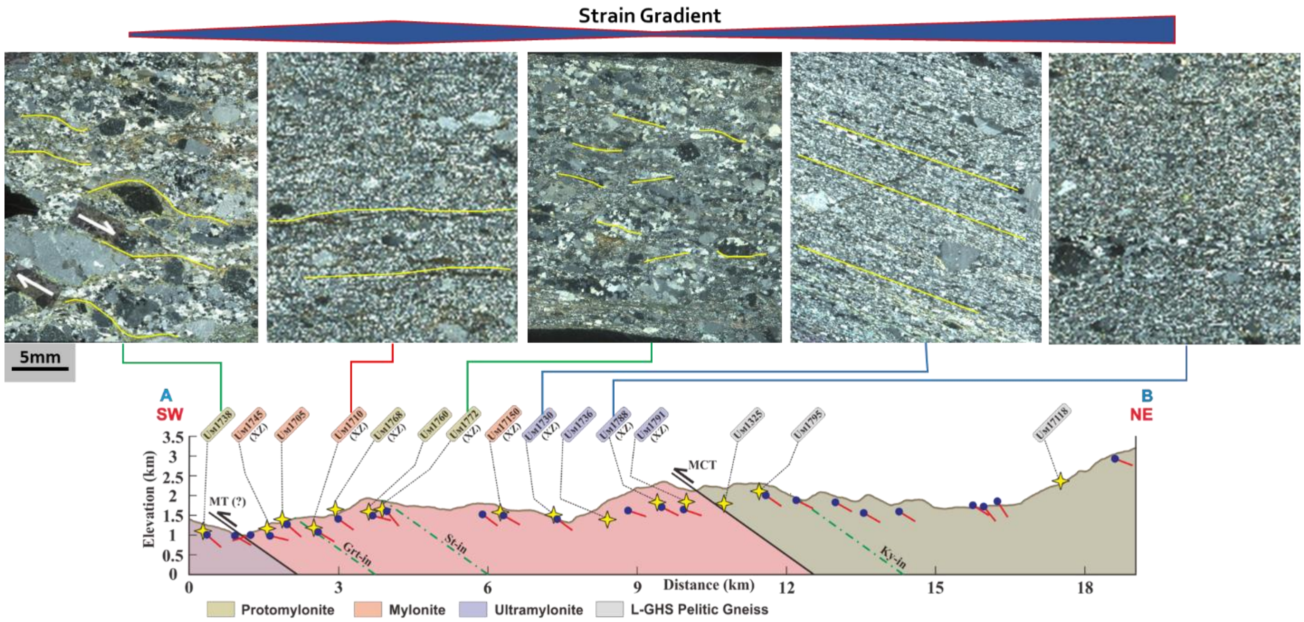

Figure 5.2. A geological cross section along AB line in Figure 5.1. Representative microphotographs showing overall microstructural variation which define a strain gradient across the Munsiari Formation.

5.2. Sample description

A variety of quartzofeldspathic gneisses belonging to the Munsiari Formation (~MCTZ) and Vaikrita Formation (~L-GHS) were collected from three road sections (Figure 5.1) for detailed microstructural analysis. A total of twelve samples were selected from the Munsiari Formation, while three samples were taken from the Vaikrita Formation for EBSD analysis.

Munsiari Formation samples have encountered the impact of non-coaxial deformation caused by shearing along the MCT. Evidences of such deformational features are documented in the Chapter 3. Samples collected from the Munsiari Formation were categorized on the basis of relative abundance of feldspar porphyroclast and the matrix phases (Figure 5.2). In the lower Munsiari Formation, the samples (UM1738, UM1768, UM1760 and UM1772) containing higher abundance of feldspar porphyroclast and anastomosing foliation defined by the micas, represent the characteristics of protomylonite (Figure 5.2). Whereas, some samples (UM1745, UM1705, UM1710 and UM17150) from the lower Munsiari Formation, exhibit well-developed mylonitic foliation (S_m) defined by the orientation of biotite and muscovite (Figure 5.2). Such samples are banded in nature where the alternating layers of ribbon-shaped quartz, fine-grained mica, and mixed quartzo-feldspathic domain create distinct compositional layers (Figure 5.4d and e). Quartz grain size in thick quartzose domain (~89 µm) of protomylonite is coarser than that of thin layers in mylonites (~65 µm). The samples (UM1730, UM1736 and UM1788) collected from the upper Munsiari Formation, are characterized by a relatively higher fraction of fine-grained quartzo-feldspathic aggregates (~33 µm) which reflect the characteristics of ultramylonite. L-GHS samples (UM1325, UM1795 and UM17118) are relatively coarse grained (~120 µm) and contains high-grade metamorphic minerals such as garnet and kyanite.

5.3. Methodology

The XZ plane parallel to the stretching lineation and perpendicular to the foliation were chosen to prepare thin sections (Figure 5.3) from eight rock samples (Figure 5.2). In addition, 8 more thin sections were prepared by cutting along the dip direction and perpendicular to the foliation plane from rock samples lacking stretching lineation. The initial stages of polishing was carried out using 3 and 1 mm diamond paste. Ultra-fine polishing in the final stage using colloidal silica was required for electron backscatter diffraction (EBSD) analysis.

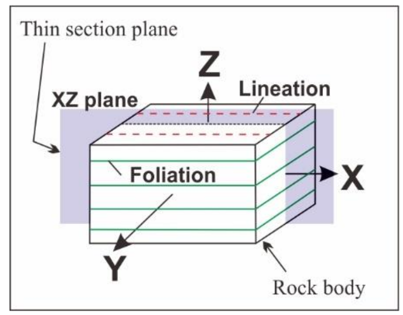

Figure 5.3. Reference frame (XZ plane) for microstructural analysis where X represents lineation and Z is the perpendicular to the foliation (XY); X,Y and Z represent maximum, intermediate and minimum principle strain axis respectively.

5.3.1. Analytical strategy

EBSD analysis was performed in a targeted manner on three types of microstructural domains, such as (i) quartzose domain in protomylonite, (ii) thin quartz layers (~70-165 µm thickness) separated by secondary mineral phases in mylonite and ultramylonite, and (iii) mixed polyphase domain in mylonite and ultramylonite. Quartz LPO data was collected from the first two domains mainly by point analysis at the scale of whole thin section (sample no. UM1738, UM1745, UM1710, UM1768, UM1760, UM1772, UM17150 and UM1730). Objective of point analysis is to avoid the effect of secondary mineral phases in the case of quartz rich domain. Whereas, point analysis was done on thin layers not to get the quartz in polyphase domain (UM1745, UM1710 and UM1730). However, some of the polyphase domains were separately mapped (sample no. UM1710, UM1705, UM1730, UM1736 and UM1788) for quantifying the microstructures like grain size, shape, modal proportion of phases etc. Moreover, we checked for any variation in the bulk LPO pattern from point analysis against the LPO data generated from small-scale mapping in case of several thin sections (UM1738 and UM1745). Such comparisons are important to increase the confidence level for interpreting the representative LPO fabric patterns. In order to understand the micro-scale processes of heterogeneous strain localization, EBSD mapping was carried out from both the quartz rich and polyphase domain of individual thin sections (UM1788, 1730, 1710).

5.3.2. Analytical conditions for EBSD analysis

Analysis was conducted in a JEOL JSM-7100F at Hokkaido University. This machine was operated at 30 kV in high current mode. Analysis was performed in variable pressure mode with 15 Pa of Nitrogen gas in the chamber. A NordlysF EBSD camera was used to measure diffraction patterns, and data were collected and indexed to extract crystallographic information using the Oxford Instruments AZtec software package. A working distance of between 20 and 25 mm was selected to position the signal in the center of the EBSD camera.

5.3.3. Data processing

Reduction of noise in the data was performed using the HKL Channel 5 software package. A 5-neighbour extrapolation was used to reduce zero solutions, and “wild spikes” (isolated pixels of incorrect orientation) were removed. Processed data from Channel 5 were analysed in the MTEX toolbox for Matlab™ (Bachmann et al., 2010) to determine grains based on a minimum 10 ° misorientation. The perceptually-uniform color map “broc” is used in this study to prevent visual distortion of the data (Crameri, 2018). Using Channel5, a data set was created from the maps on the basis of one point per individual grain and exported to text file for analyzing those in the Stereonet software (version 10.2.8; Allmendinger et al., 2013; Cardozo and Allmendinger, 2013) to obtain eigenvalues (λ_1, λ_2 and λ_3) of LPO of a sample.

5.3.4. LPO fabric analysis

Determining c-axis orientations of quartz is a useful component of LPO analysis, because it produces topologies that are easily identifiable and useful for quantitative characterization (e.g., Schmid and Casey, 1986). External stress field and other controlling factors cause deformation of

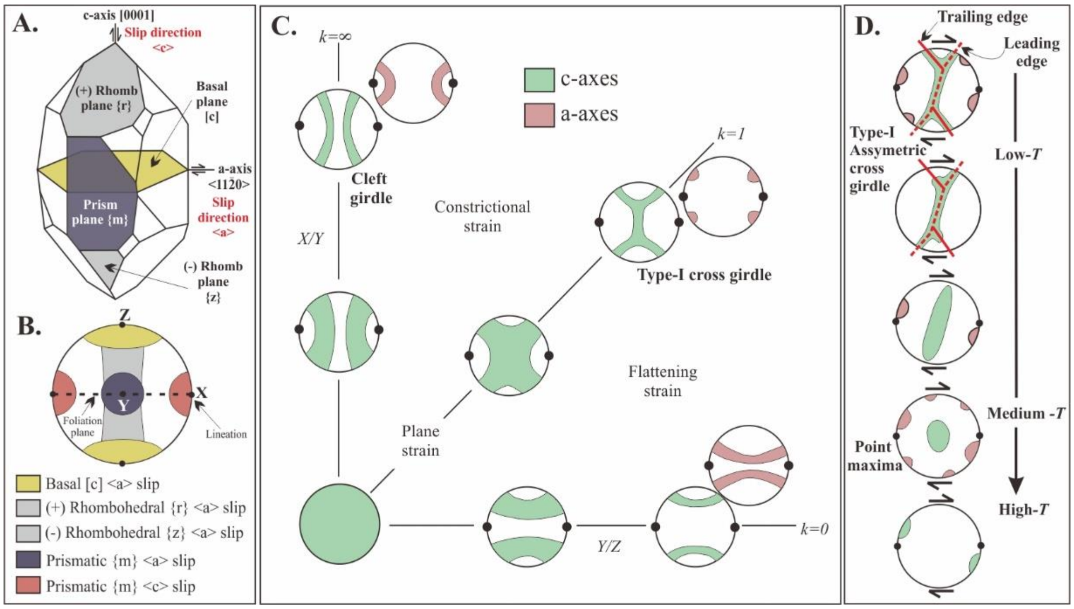

Figure 5.4. (A) Basic components of a trigonal crystal of quartz showing the presence of common slip systems (modified after Neumann, 2000). (B) Stereographic projection of the reference frame (XZ plane) for LPO analysis; Colored zones are the regions of quartz c-axes maxima corresponding to common slip system activity (modified after Toy et al., 2008). (C) and (D) showing the types of LPO fabrics of quartz c- and a-axes formed as result of slip system activity (modified after Passchier and Trouw, 2005). (C) Flinn diagram showing the relation of geometry of LPO patterns of quartz c-axes and a-axes with strain in the case of coaxial progressive deformation. (D) Quartz LPO fabrics showing the evolution of LPOs with increasing temperature during non-coaxial progressive deformation.

quartz crystals by means of slip system activity. EBSD analysis provides complete crystallographic orientation data in the form of Euler angles, which are directly transformed into lower hemisphere stereographic projection producing discrete pole figures of the main crystallographic directions c [0001] and a <11-20> and the poles to the main lattice planes m {10-10} and r {10-11}. The common distribution of c-axis maxima, when viewed on a (0001) pole figure, corresponds to various slip systems activity in quartz. Furthermore, the stereographic equal angle projection patterns of quartz c-axis orientations were then classified according to the patterns described in literature (Figure 5.4C, D). The results include small-circle girdle, cleft girdle, simple asymmetric girdle, type I and II crossed-girdle and type I asymmetric girdle (Tullis, 1977; Lister and Williams, 1979; Lister and Hobbs, 1980; Price, 1985; Schmid and Casey, 1986; Takeshita and Wenk, 1988; Passchier and Trouw, 2005).

5.3.5. Measurement of fabric strength

Quantification of LPO fabric is necessary to determine fabric strength numerically which further incorporates to a quantitative correlational study of different fabrics. The fabric strength was determined through various processes based on the relationships between normalized eigen values (B-index; Vollmer, 1990), Euler angles (J-index; Bunge, 1982; Mainprice et al., 1993) of the orientation tensor (e.g. Woodcock, 1977) and the distribution of uncorrelated misorientation angles (M-index; Skemer et al., 2005). B-index i.e. cylindricity measures an orientation tensor that is calculated by matrix summation of three-unit column eigenvectors that represent the orientation of each crystal (Vollmer, 1990), while the M-index compares the distribution of misorientation angles between crystals in a sample with the expected distribution of misorientation angles in an ideally random fabric (Skemer et al., 2005).

5.3.6. Deformation thermometry

Two-feldspar thermometry is used for calculating deformation temperature that can be compared with the assumed deformation temperature from quartz microstructures and LPO fabrics. Compositions of coexisting plagioclase and k-feldspar generally provide the temperature of chemical re-equilibrium of feldspars during tectonothermal events. The rim compositions of the adjacent feldspar pairs, give reasonable temperature estimates when the two-feldspar thermometer is applied. Myrmekitic plagioclase and k-feldspar from the Munsiari formation (Figure 5.12 b-f) are analyzed for the chemical composition while the perthitic k-feldspar and plagioclase (Figure 5.12 a) were selected for two feldspar thermometry. Electron microprobe analyses of the representative samples were carried out on the JEOL-8800R Electron Probe Micro Analyzer at Hokkaido University, Sapporo. Thin sections of the representative samples were prepared with the carbon coating prior to the EPMA analysis. The analyses were run with a probe current of 20 nA, an acceleration voltage of 15 kV and beam diameter of 1 μm. Temperatures were determined on the basis of two-feldspar thermometer of Stormer, 1975 and Stormer and Whitney, 1985.

5.4. Microstructural observations

Protomylonites of the lower Munsiari Formation consist of porphyroclast of perthitic K-feldspars and sericitised plagioclase, discontinuous layers of coarse-grained quartz aggregates, fine-grained quartzofeldspathic domain and fine-grained micas. Thick quartzose domains are comprised of recrystallized quartz grains with highly irregular grain boundary indicating the dynamic recrystallization occurred by grain boundary migration (GBM) at high temperature (Figure 5.5a).

Some of the quartz grains exhibit dislocation wall as it represents the recovery process followed by subgrain formation (Figure 5.5a). Plagioclase porphyroclasts are also deformed which are showing deformation lamellae.

In the banded mylonites of lower Munsiari Formation, core-mantle structure is common in thin quartzose layers of some samples (sample no. UM1745 and UM1705) where relict quartz is surrounded by the recrystallized quartz grains (Figure 5.5b). These recrystallized grains further experienced static grain growth evidenced by the presence of polygonal grains attached together forming triple point junction (Figure 5.5c). Whereas, some other mylonites in the lower Munsiari Formation (e.g. UM1710) contain thin layers of ribbon shaped quartz grains alternating with the layers of quartzofeldspathic domain (Figure 5.5d). Pinning effect of biotite and muscovite cause shape preferred orientation of quartz grains (Figure 5.5d) where the micas inhibit the migration of grain boundaries.

In the upper part of Munsiari Formation, ultramylonites are comprised of thin layers of elongated quartz grains, higher fraction of quartzofeldspathic aggregates and minor amount of biotite and muscovite (Figure 5.5e). A sample of micaceous quartzite (UM1791) shows the evidence of GBM recrystallization overprinted by low temperature deformation feature (deformation lamellae) (Figure 5.5f). Most of the grains associated with biotite flakes exhibit straight grain boundary due to the obstruction of grain boundary mobility by the micas (Figure 5.5f).

L-GHS samples are relatively coarser than the Munsiari formation sample. Mineral assemblage of these rocks contain quartz, plagioclase, muscovite, biotite, garnet and kyanite. Quartz grains have the signature of high grain boundary mobility ((Figure 5.5g, h). These grains also contain numerous elongated subgrains (Figure 5.8g, h). Quartz in kyanite bearing sample is consisted of chessboard pattern subgrain (Figure 5.8h). Deformation lamellae is present in plagioclase.

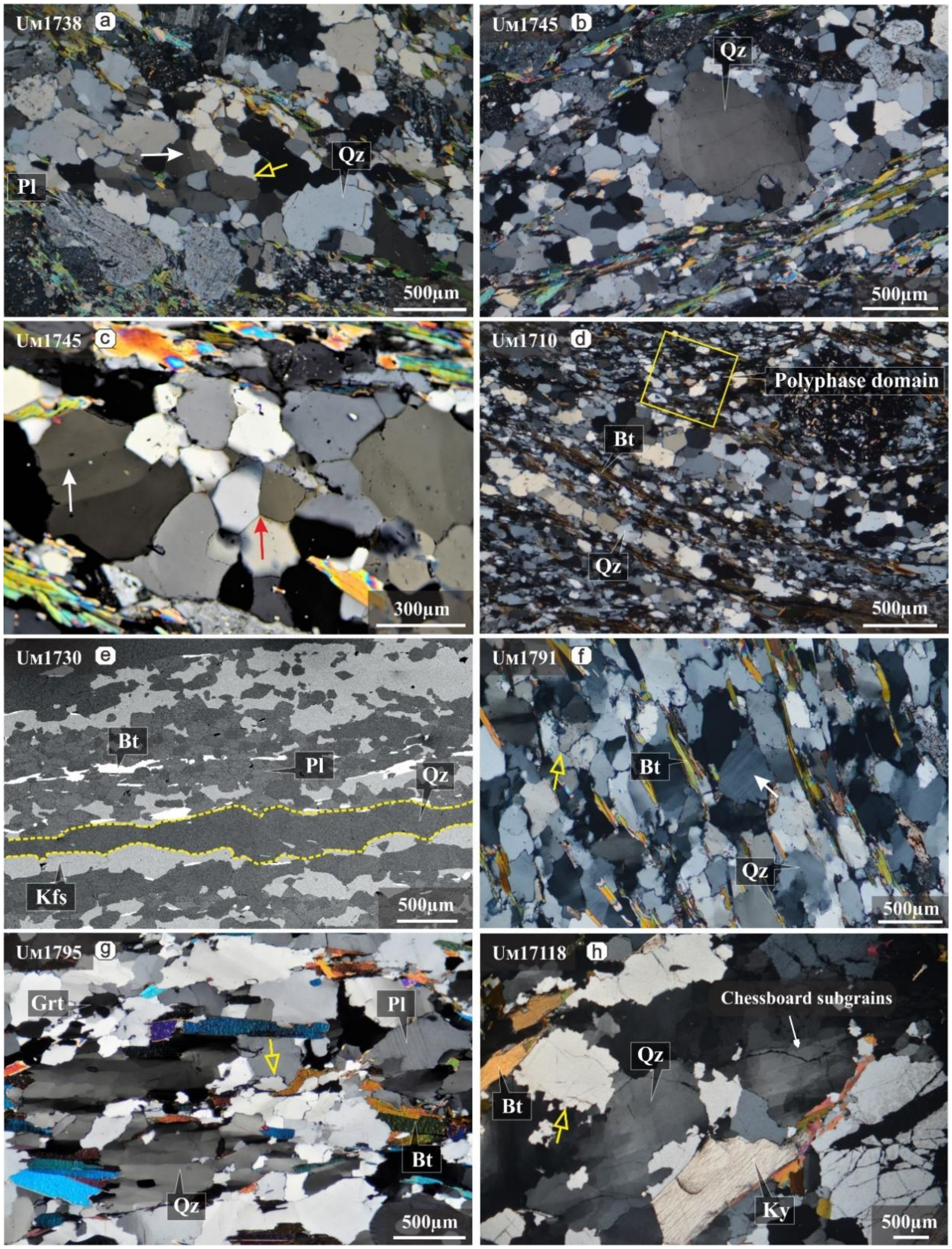

Figure 5.5. Representative microphotographs showing evidence of deformation mechanisms in different domain; (a) Quartz grain have dislocation wall (subgrain boundary) shown with white arrow. (b) Subgrain rotation recrystallization (SGR). (c) Triple point junction (red arrow) indicating static grain growth. (d) Well defined mylonitic foliation with alternating layers of ribbon shaped quartz and micas. (e) Thin quartz layers in ultramylonite, are surrounded by orthoclase. (f) Mobility of grain boundary towards the direction of schistosity whereas straight grain boundary across the schistosity showing the effect of mica pinning. (g) In L-GHS sample, quartz grains showing highly irregular grain boundary with elongated subgrains. (h) Structurally uppermost sample showing chessboard pattern subgrain of quartz in kyanite bearing paragneiss.

5.5. Results

5.5.1. Quartz LPOs and slip system activity

Thick quartzose domain in protomylonite

Projection of quartz c-axis (0001) orientations obtained by EBSD point analysis, exhibit type-II crossed-girdle pattern with point maxima around Y-direction of strain ellipsoid (Y-maxima) producing well-defined orthorhombic symmetry (Figure 5.6). Result of mapping was obtained for one sample (UM1738) which shows similarity with the result of point analysis (Figure 5.7). In all cases, a-axes maxima are oriented oblique to the x-direction whereas *m*-poles occur subparallel to the x-direction. LPO fabric of lower most sample (UM1738) indicates the activity of prism {m} <a> slip with minor rhomb {r} <a> slip and basal [c] <a> slip. Where other LPO fabrics (UM1768, UM1760, UM1772) show relatively higher density of c-axes around Y-direction which are formed exclusively by prism {m} <a> slip with minor basal [c] <a> slip.

Thin quartzose layer in banded mylonite

Lower most sample (UM1745) produces type-II crossed-girdle with Y-maxima and rhomb maxima (Figure 5.6) suggesting {m} <a> and {r} <a> slip. Mapping results from two samples (UM1745 and UM1705) also provides the same information with some random orientations of c-axes (Figure 5.7). Thin quartz layer of sample UM1710 generates weak asymmetric type-I girdle (Figure 5.6I) indicating the existence of simple shear component and the fabric is formed as a result of activation of {m} <a> slip, {r} <a> slip and [c] <a> slip. Whereas, type-II crossed-girdle is found for the sample UM17150.

Quartzose domains in ultramylonite

Sample UM1730 shows well-defined c-axis fabric similar to asymmetric type-I girdle (Figure 5.6) suggesting significant activity of {r} <a> slip. Furthermore, this asymmetric fabric helps to identify the effect of non-coaxial flow with top-to-the-southwest shear sense. Sample UM1788 also produces asymmetric type-I fabric with strong rhomb maxima (Figure 5.7) indicating the presence of {r} <a> slip. This fabric also give information of non-coaxial deformation as a result of top-to-the-south sense of simple shear. Quartz LPOs obtained from micaceous quartzite

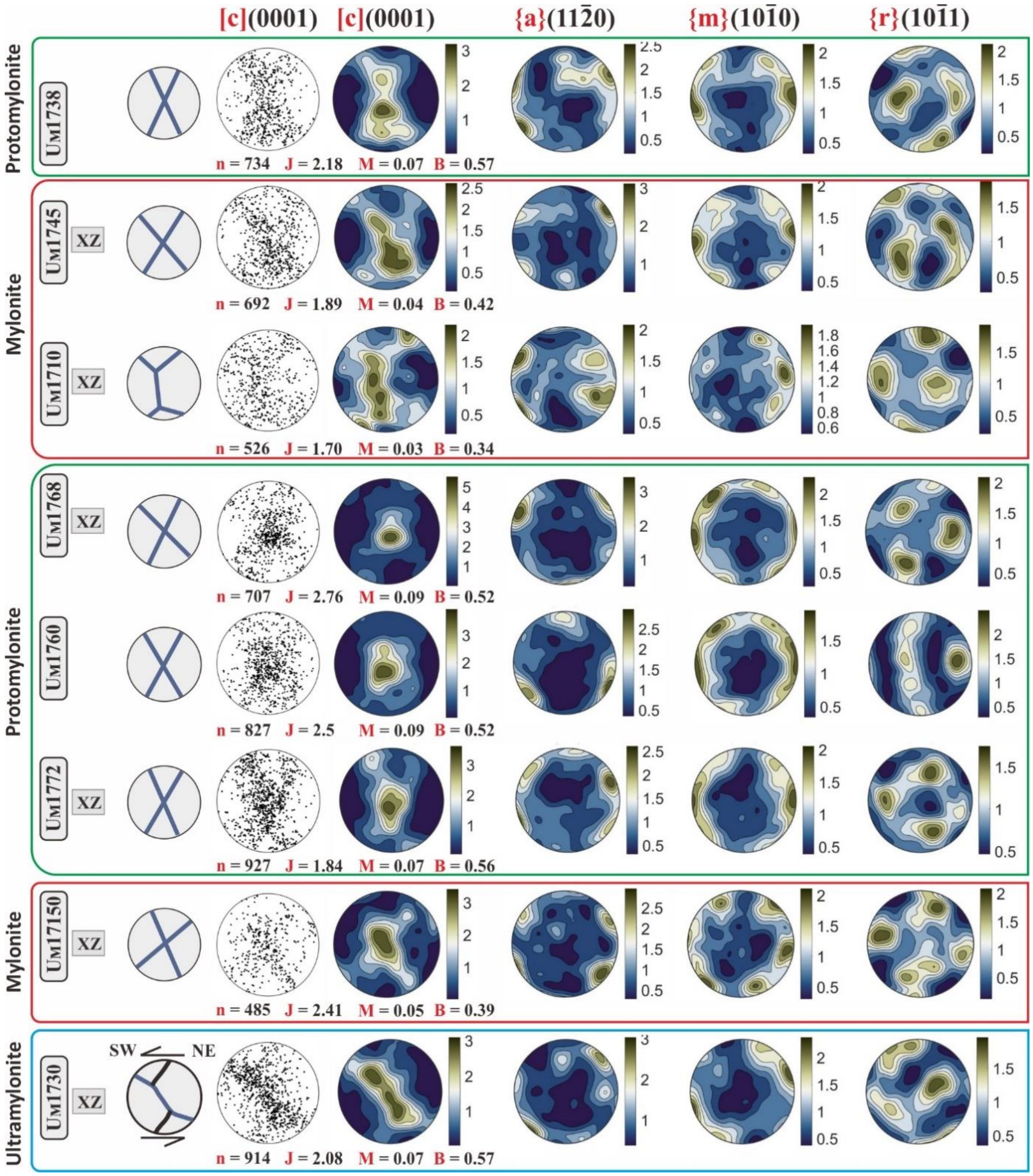

Figure 5.6. Calculated quartz pole figures up sequence, measured using electron backscattered diffraction (EBSD) by doing point analysis. Pole figures are contoured to multiples of uniform distribution, following the density range in the adjacent color bars.

(UM1791) in the zone of ultramylonite, is characterized by single girdle with monoclinic symmetry indicating {m} <a> slip with subordinate {r} <a> slip and [c] <a> slip (Figure 5.7).

Polyphase domain in mylonite and ultramylonite

Quartz grains in the polyphase domain of mylonites (UM1705 and UM1710) exhibit random LPO pattern (Figure 5.8). In contrast, the protomylonite samples UM1730 and UM1788, are characterized by a weak asymmetric type-I fabric suggesting the development of fabric during non-coaxial deformation (Figure 5.8). Sample UM1736 exhibits small circle girdle around X-direction, which can be defined as cleft girdle (Figure 5.8).

Quartz aggregates in L-GHS pelitic gneiss

Samples UM1325 and UM1795 show type-II crossed-girdle fabric with Y-maxima suggesting {m} <a> slip and [c] <a> slip (Figure 5.9).

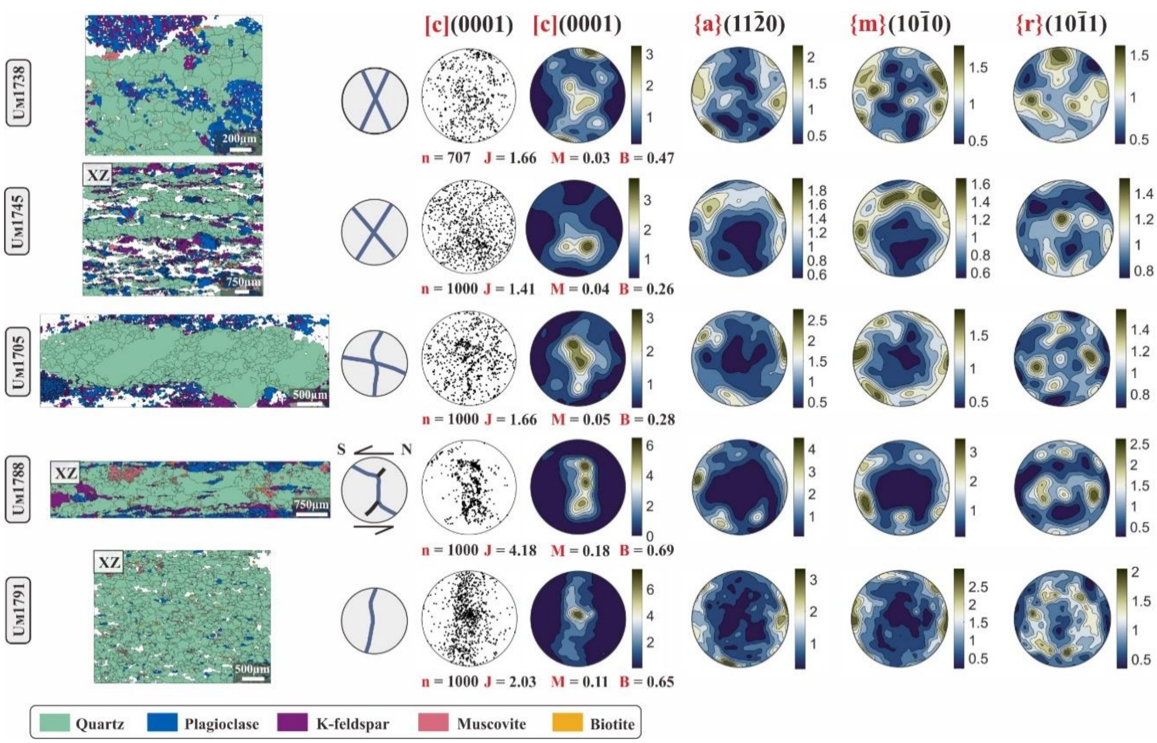

Figure 5.7. Calculated quartz pole figures up sequence, measured using electron backscattered diffraction (EBSD). These are the result of mapping analysis of quartz rich domains. Pole figures are contoured to multiples of uniform distribution, following the density range in the adjacent color bars.

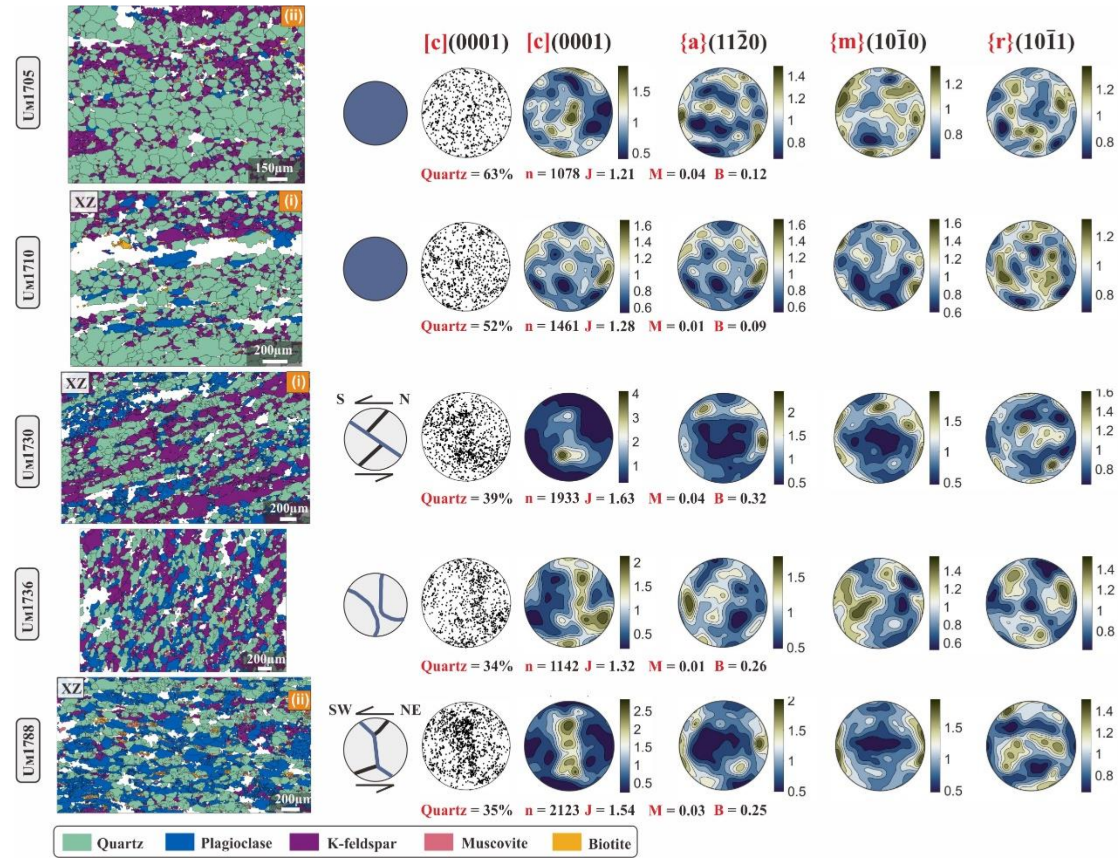

Figure 5.8. Representative colored phase map and pole figures of quartz obtained from EBSD analysis of polyphase domain. Figures are arranged in an order towards structural high. White areas mostly represent non-indexed fraction of micas.

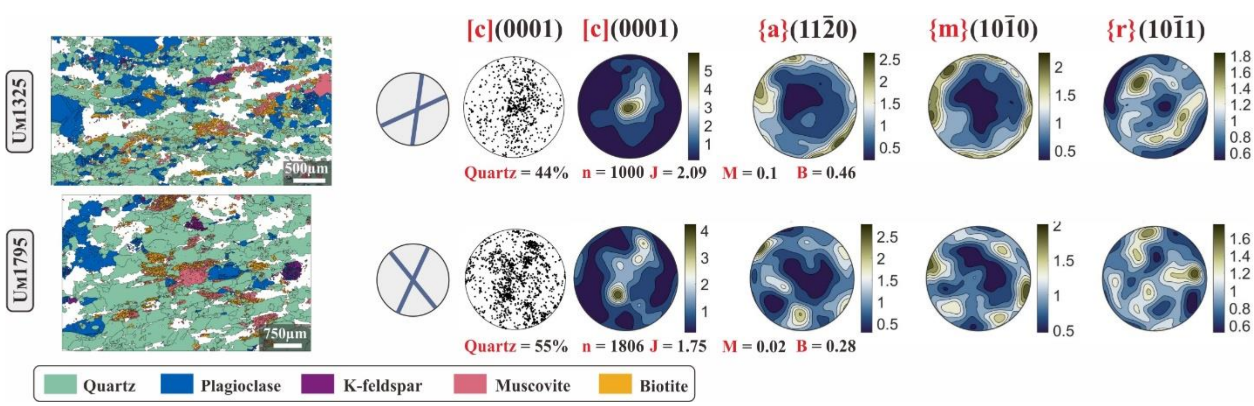

Figure 5.9. EBSD mapping results of L-GHS samples. Pole figures are contoured to multiples of uniform distribution, following the density range in the adjacent color bars.

5.5.2. *Fabric intensity*

Variation of fabric intensity (M and B-index) can be seen if all quartzose domains are compared to each other (Figure 5.10). M-index calculated from EBSD point analysis data exhibit a trend throughout the Munsiari formation where it decreases from the lowermost protomylonite to the zone of mylonite followed by an increase towards the zone of protomylonite (Figure 5.10). Therefore, the fabric intensity is observed to be higher for thick quartzose domain in protomylonite with compared to thin quartzose layers in the mylonites. However, the fabric intensity is further increased towards the zone of ultramylonite. EBSD mapping results are consistent with the result obtained from the point analysis.

Table 5-1. Summary of the fabric intensity parameters calculated from EBSD point analysis and mapping data.

	Sample No.	M-index	B-index
Quartzose layers in the Munsiari samples			
Point analysis	1738	0.07	0.57
	1745	0.04	0.42
	1710	0.03	0.34
	1768	0.09	0.52
	1760	0.09	0.52
	1772	0.07	0.56
	17150	0.05	0.4
	1730	0.07	0.57
Mapping	1738	0.03	0.47
	1745	0.04	0.26
	1705	0.05	0.28
	1788	0.18	0.69
	1791	0.11	0.65
Polyphase domain			
Munsiari	1705	0.004	0.12
	1710	0.005	0.09
	1730	0.04	0.32
	1736	0.01	0.26
	1788	0.03	0.25
L-GHS	1325	0.1	0.46
	1795	0.02	0.28

For the case of polyphase domain, M-index and B-index values are generally lower than that of the quartzose domains (Table 5-1). Plotting of the fabric intensity is being correlated with the modal abundance of quartz, K-feldspar and plagioclase (Figure 5.11). Among all the samples of the Munsiari formation, higher modal % of quartz was mapped in the samples UM1705 and UM1710 which provides with the result of relatively lower M-index than those with lower modal % of quartz. Overall trend of the fabric intensity parameters can not be correlated with the modal % of quartz and other associated phases. Textural relationship between the phases by means of % of area of quartz attached with other phases, is probably crucial to be noted.

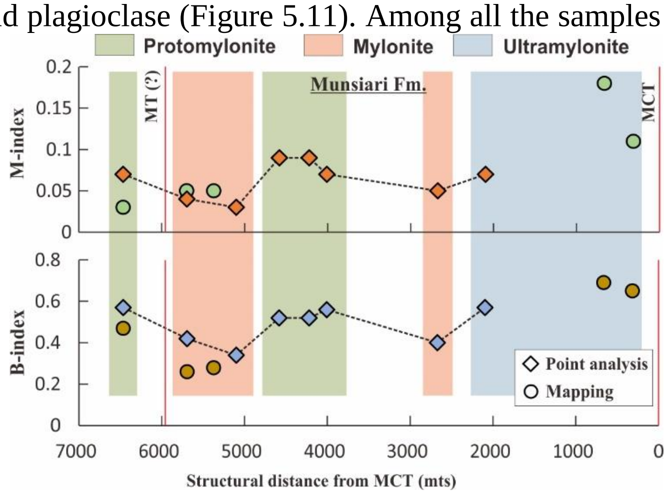

Figure 5.10. Fabric intensity parameters calculated for thick and thin quartzose layers, plotted against structural distance from the MCT.

Fabric intensity of the sample UM1325 is higher than all other samples and more or less similar with higher Munsiari samples (UM1788 and UM1791) (Table 5-1). Whereas, the sample

UM1795 results to a similar intensity as of other Munsiari samples.

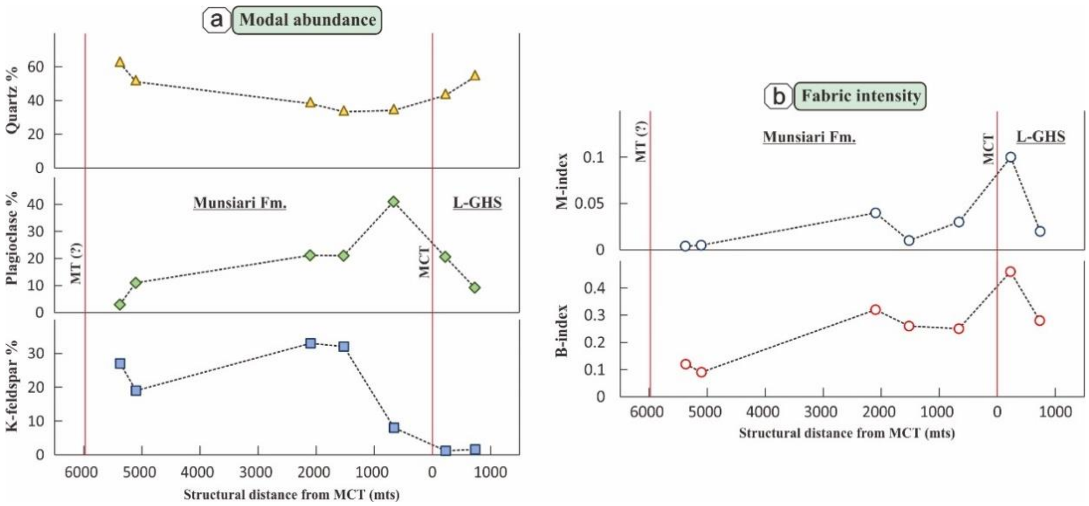

Figure 5.11. M-index and B-index calculated for the quartz grains in polyphase domain, plotted against structural distance from the Munsiari thrust. These intensity parameters are being correlated with the modal % of quartz, plagioclase and K-feldspar.

5.5.3. Grain size analysis

Grain size analysis was performed for the recrystallized quartz grain in three domains (Figure 5.12). It is observed that recrystallized grain size for thick quartzose domain in all protomylonites is around ~93.3 µm. Whereas, grain size for thin quartzose layers of all mylonites is around ~69.9 µm. Recrystallized quartz in polyphase domains of mylonite and ultramylonite is relatively fine grained with the grain size about ~33 µm. Therefore, a reduction in recrystallized grain size is observed from thick quartzose domain to polyphase domain.

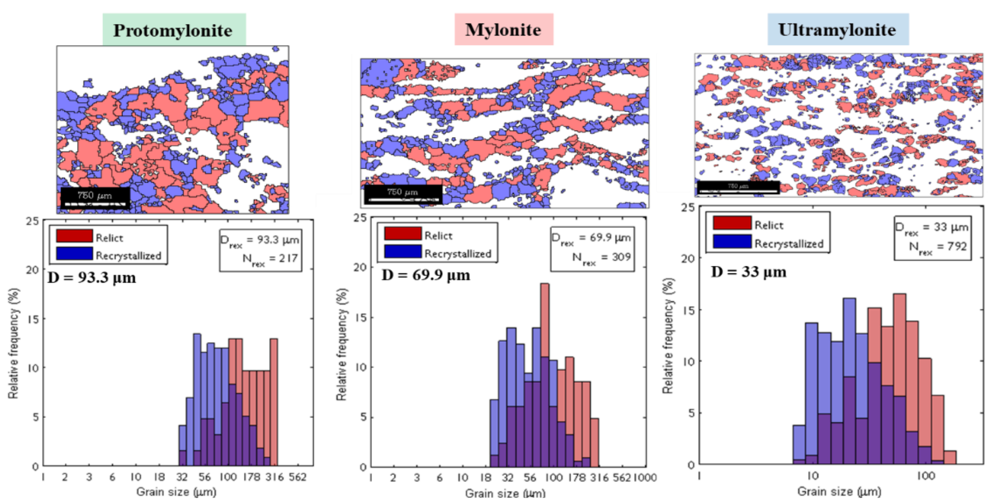

Figure 5.12. Results of grain size analysis obtained from the recrystallized quartz grains in three different domains in protomylonite, mylonite and ultramylonite.

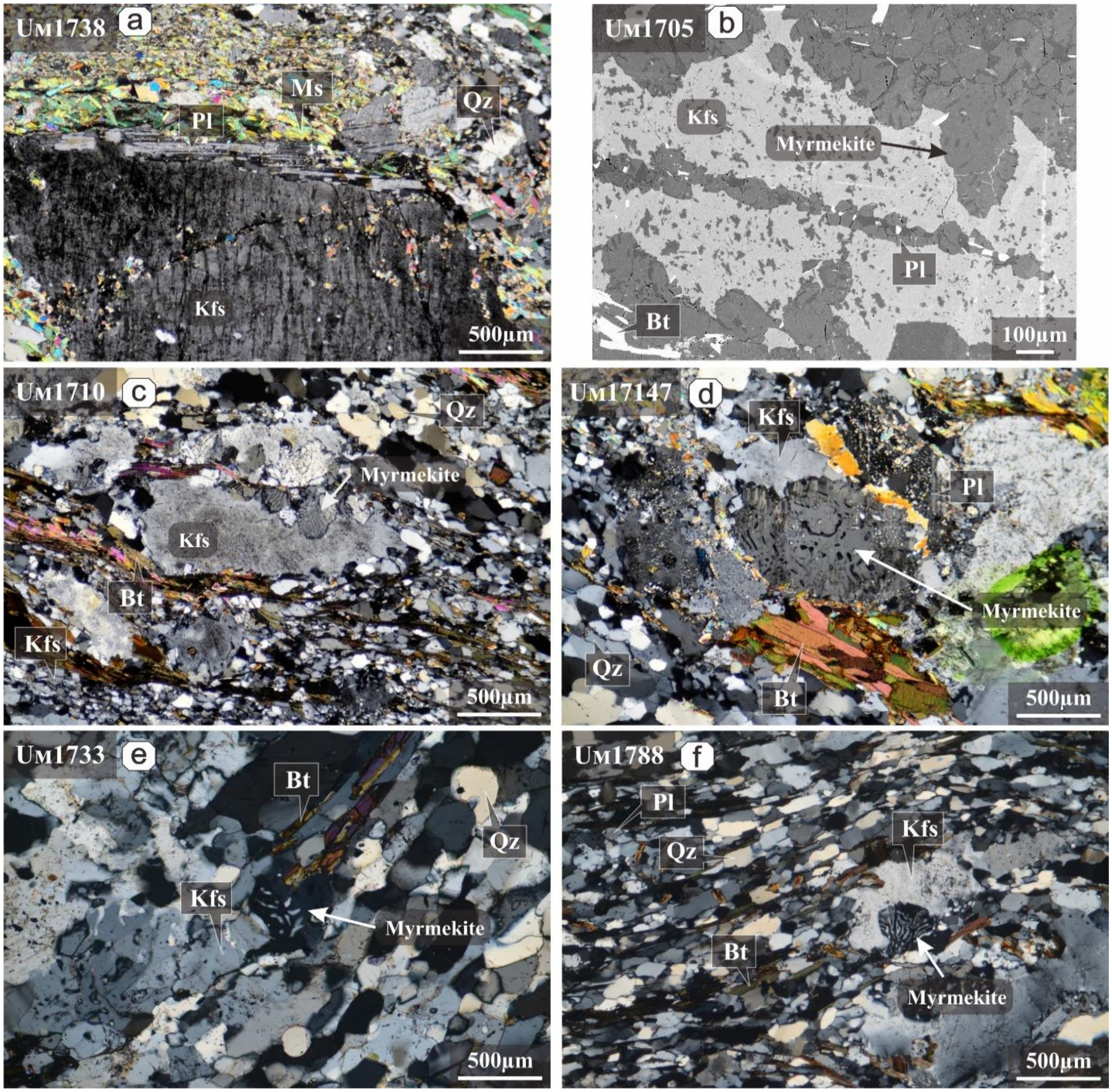

Figure 5.13. Representative microphotographs and BSE image of the samples used to show the textural relationship between K-feldspar and plagioclase. (a) Lower most sample with coexistence of plagioclase and perthitic K-feldspar. (b) BSE image showing the growth of myrmekite at the margin of K-feldspar porphyroclast. It also shows the occurance of fine grained plagioclase within the fracture oriented perpendicularly to the myrmekitic growth. (c) Direction of myrmekitic growth is perpendicular to the orientation of main foliation defined by the orientation of biotite flakes. (d) Coarse grained myrmekite associated with relatively finer grained K-feldspar. (e) Replacement of matrix K-feldspar by myrmekite. (f) Myrmekitic growth at the edge of K-feldspar porphyroclast.

5.5.4. Myrmekite and two-feldspar thermometry

Myrmekite present at the boundary of perthitic K-feldspar, is oriented perpendicularly to the main foliation (Figure 5.13c, f) which suggest the growth along incremental shortening direction. Thus, the presence of of myrmekite represents the site of high normal stress (Simpson & Wintsch, 1989). In some cases, fractures are observed in K-feldspar oriented at a high angle to the inferred to the myrmekite (Figure 5.13b). In the sample UM1733, myrmekite is generally fine grained and do not show the orthogonal relation with the schistosity (Figure 5.13e). Two-feldspar thermometry results show that deformation temperature of lowermost sample is about 356 °C whereas Munsiari formation rocks experienced deformation temperature ranging from 419 °C to 482 °C. Plotting of temperature distribution against structural distance from the Munsiari thrust does not show any increasing trend towards structural high (Figure 5.14).

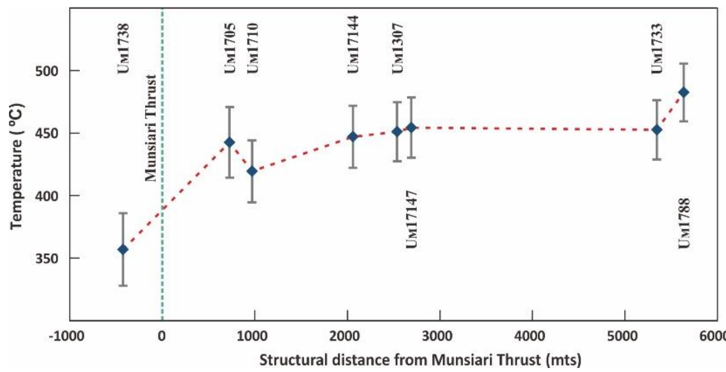

Figure 5.14. Results of two-feldspar thermometry are plotted against the structural distance from the Munsiari Thrust.

5.6. Discussion

5.6.1. Inferences from LPO fabric from quartz rich domain

In the case of quartz rich domains, type II crossed girdle with Y-maxima could be explained either by the effect of coaxial progressive deformation in constriction field (Bouchez, 1978) or high temperature deformation (Schmid and Casey 1986; Law 1990) which is further supported by the high temperature grain boundary mobility. However, presence of shear strain feature such as sigmoidal porphyroclast and shear band (sample UM1738), contradict the effect of high temperature on developing type-II crossed girdle. Several authors have described the close relationship between GBM recrystallization and prismatic <a> slip (Knipe and Law, 1987; Pennacchioni et al., 2010; Stipp et al., 2002b). However, it has also been shown that the prismatic <a> slip system can also dominate in quartz deformed under increased shear strains (Heilbronner and Tullis, 2006; Pennacchioni et al., 2010). This suggests that the activation of the prismatic <a>

slip system, and the onset of GBM recrystallization, may result from a complex interplay among temperatures, bulk shear strains, and possibly other parameters (e.g., water content). However, development of well-developed leading edge in the sample UM17150 (Figure 5.4J) could BE explained by the effect non-coaxial flow.

5.6.2. LPO as kinematic indicator

Asymmetric type-I quartz c-axis fabric is strongly developed in the sample UM1730 and UM1788. The fabric pattern is obtained from both quartzose layer and polyphase domain. Type-II crossed girdle from quartz rich domain (UM17150) with strong leading edge produces some extent of non-symmetrical distribution of c-axes. A weak asymmetric type-I fabric also persists in lower Munsiari sample (UM1710). All these fabrics represents top-to-the-South sense of shear.

5.6.3. Zone of high shear strain

Sample from upper part of the Munsiari formation exhibits the result of non-coaxial flow in quartz-rich as well as polyphase domain inferred from asymmetric type-I c-axis fabric as well as high fabric intensity. Sample UM1730 showing well-defined asymmetric type-I c-axis fabric and higher fabric intensity. This observation might suggest higher accumulation of shear strain in this region. Thus, the region indicates the probability of the high shear strain built up during thrusting along the MCT.

5.6.4. Monophase layer vs. Polyphase domain

EBSD results were obtained from both quartzose layers and polyphase domain for the Sample UM1710, UM1730 and UM1788. Thin quartz layer of the sample UM1730 experienced non-coaxial deformation inferred from type-I asymmetric c-axes fabric. Whereas, weak type-I asymmetric fabric can also be observed through mapping of two polyphase domains. This fabric is generally formed as a result of GSI creep mostly accommodated by rhomb <a> slip. Thus, this results indicate non-coaxial flow affects both the layer of quartz and the polyphase domain. Weak type-I asymmetric fabric might explain the process of grain boundary sliding. Generally, the randomness of LPO fabric of polyphase domain in lower Munsiari formation is due to abundant second phases (feldspar and mica) which is inhibiting the mobility of the grain boundaries of the quartz suggesting that GSI creep is hard to achieve steady state conditions. The data collected from quartzose layers and polyphase domain from some samples suggests that quartz grains from both domain respond to predominantly extrinsic conditions (e.g. strain rate, temperature). Although, it is likely that the phase interactions within polyphase domain rocks that could have caused some randomness in the quartz LPO fabric, rather than physical conditions outside the rock alone.

5.7. Conclusions

(1) Deformation mechanisms observed in Quartz aggregates of the metamorphic rocks in a shear zone is a function of set of controlling factors such as- (a) temperature, (b) strain rate, (c) water content, (d) modal abundance of secondary phases and (e) rheological contrast in a rock. Perhaps, deformed rocks are the results of complex interplay of these factors.

(2) Dislocation creep mechanism (GSI creep) is dominant in the thick quartz rich domain.

(3) Upper Munsiari formation samples show Existence of GSI creep under non-coaxial flow condition is perhaps persistent in both the quartzose layer and polyphase domain.

(4) Random fabric of quartz LPO can explain effect of strain partitioning among other secondary phases. However, GSS creep such as pressure solution process may influence to produce such randomness

(5) Extent of the shear zone can be defined with respect to the presence of asymmetric type-I girdle in lower Munsiari formation as well as upper Munsiari formation.

(6) Well defined asymmetric type-I fabric and higher fabric intensity in upper Munsiari samples could suggest the occurrence of the MCT.

(7) Rheological difference in a rock induced by the presence of porphyroclast, monophase and polyphase domain, could also be the reason behind the evolution of LPO fabric in the MCT zone.

(8) Furthermore, Deformation in a shear zone could also be the outcome of heterogeneities coming from existing different rock type with different rheological properties. Strain accumulation in a zone is broadly dependent on rheological heterogeneity of different rock types. There is a wide lithological variation persist in the study area as the granitic rocks are associated with pelitic, calcareous and metabasic rocks which could affect the deformational behavior of granitic gneiss.

References

Ahmad, T., Harris, N., Bickle, M., Chapman, H., Bunbury, J., Prince, C., 2000. Isotopic constraints on the structural relationships between the Lesser Himalayan Series and the High Himalayan Crystalline Series, Garhwal Himalaya. Bull. Geol. Soc. Am. 112, 467–477. https://doi.org/10.1130/0016-7606(2000)112<467:ICOTSR>2.0.CO;2

Aikman, A.B., Harrison, T.M., Lin, D., 2008. Evidence for Early (> 44 Ma) Himalayan Crustal Thickening, Tethyan Himalaya, southeastern Tibet. Earth Planet. Sci. Lett. 274, 14–23. https://doi.org/10.1016/j.epsl.2008.06.038

Aitchison, J.C., Xia, X., Baxter, A.T., Ali, J.R., 2011. Detrital zircon U-Pb ages along the Yarlung-Tsangpo suture zone, Tibet: Implications for oblique convergence and collision between India and Asia. Gondwana Res. 20, 691–709. https://doi.org/10.1016/j.gr.2011.04.002

Allegre, C.J., Courtillot, V., Tapponnier, P., Hirn, A., Mattauer, M., Coulon, C., Jaeger, J.J., Achache, J., Scharer, U., Marcoux, J., Burg, J.P., Girardeau, J., Armijo, R., Gariepy, C., Gopel, C.,Li, T.D.,Xiao, X.C., 1984. Structure and evolution of the Himalaya–Tibet orogenic belt. Nature 307, 17–22

Allmendinger, R.W., Cardozo, N.C., Fisher, D., 2013. Structural Geology Algorithms: Vectors & Tensors. 289 pp. Cambridge Univ. Press, Cambridge, England.

Arita, K., 1983. Origin of the inverted metamorphism of the lower Himalayas, Central Nepal. Tectonophysics 95, 43–60. https://doi.org/10.1016/0040-1951(83)90258-5

Avouac, J. P. (2007), Mountain building: From earthquakes to geological deformation. Dynamic processes in extensional and compressional settings, Treatise Geophys., 6, 377–439.

Bachmann, F., Hielscher, R., Jupp, P.E., Pantleon, W., Schaeben, H., Wegert, E., 2010. Inferential statistics of electron backscatter diffraction data from within individual crystalline grains. J. Appl. Crystallogr. 43, 1338–1355. https://doi.org/10.1107/S002188981003027X

Beaumont, C., Jamieson, R.A., Nguyen, M.H., Lee, B., 2001. Himalayan tectonics explained by extrusion of a low-viscosity crustal channel coupled to focused surface denudation. Nature 414, 738–742. https://doi.org/10.1038/414738a

Beaumont, C., Jamieson, R.A., Nguyen, M.H., Medvedev, S., 2004. Crustal channel flows: 1. Numerical models with applications to the tectonics of the Himalayan-Tibetan orogen. J. Geophys. Res. Solid Earth 109, 1–29. https://doi.org/10.1029/2003JB002809

Bédard, É., Hébert, R., Guilmette, C., Lesage, G., Wang, C.S., Dostal, J., 2009. Petrology and geochemistry of the Saga and Sangsang ophiolitic massifs, Yarlung Zangbo Suture Zone, Southern Tibet: Evidence for an arc-back-arc origin. Lithos 113, 48–67. https://doi.org/10.1016/j.lithos.2009.01.011

Bhattacharyya, K., Mitra, G., 2009. A new kinematic evolutionary model for the growth of a duplex - an example from the Rangit duplex, Sikkim Himalaya, India. Gondwana Res. 16, 697–715. https://doi.org/10.1016/j.gr.2009.07.006

Bollinger, L., Avouac, J.P., Beyssac, O., Catlos, E.J., Harrison, T.M., Grove, M., Goffé, B., Sapkota, S., 2004. Thermal structure and exhumation history of the Lesser Himalaya in central Nepal. Tectonics 23, 1–19. https://doi.org/10.1029/2003TC001564

Bollinger, L., Henry, P., Avouac, J.P., 2006. Mountain building in the Nepal Himalaya: Thermal and kinematic model. Earth Planet. Sci. Lett. 244, 58–71. https://doi.org/10.1016/j.epsl.2006.01.045

Bose, S., Mandal, N., Acharyya, S.K., Ghosh, S., Saha, P., 2014. Orogen-transverse tectonic window in the Eastern Himalayan fold belt: A superposed buckling model. J. Struct. Geol. 66, 24–41. https://doi.org/10.1016/j.jsg.2014.05.008

Brookfield, M.E., 1993. The Himalayan passive margin from Precambrian to Cretaceous times. Sediment. Geol. 84, 1–35. https://doi.org/10.1016/0037-0738(93)90042-4

Burchfiel, B.C., Royden, L.H., 1985. North-south extension within the convergent Himalayan region. Geology 13, 679–682. https://doi.org/10.1130/0091-7613(1985)13<679:NEWTCH>2.0.CO;2

Burchfiel, B. C., Chen, Z., Hodges, K. V., Liu, Y., Royden, L. H., Deng, C., & Xu, J. (1992). The South Tibetan Detachment System, Himalayan Orogen: Extension contemporaneous with and parallel to shortening in a collisional mountain belt. Geological Society of America Special Papers, 269, 1–41.

Caddick, M.J., Bickle, M.J., Harris, N.B.W., Holland, T.J.B., Horstwood, M.S.A., Parrish, R.R., Ahmad, T., 2007. Burial and exhumation history of a Lesser Himalayan schist: Recording the formation of an inverted metamorphic sequence in NW India. Earth Planet. Sci. Lett. 264, 375–390. https://doi.org/10.1016/j.epsl.2007.09.011

Caddick, M.J., Konopásek, J., Thompson, A.B., 2010. Preservation of garnet growth zoning and the duration of prograde metamorphism. J. Petrol. 51, 2327–2347. https://doi.org/10.1093/petrology/egq059

Cardozo, N., Allmendinger, R.W., 2013. Spherical projections with OSXStereonet. Comput. Geosci. 51, 193–205. https://doi.org/10.1016/j.cageo.2012.07.021

Carosi, R., Lombardo, B., Molli, G., Musumeci, G., Pertusati, P.C., 1998. The south Tibetan detachment system in the Rongbuk Valley, Everest region. Deformation features and geological implications. J. Asian Earth Sci. 16, 299–311. https://doi.org/10.1016/S0743-9547(98)00014-2

Carosi, R., Montomoli, C., Iaccarino, S., Massonne, H.J., Rubatto, D., Langone, A., Gemignani, L., Visonà, D., 2016. Middle to late Eocene exhumation of the Greater Himalayan Sequence in the Central Himalayas: Progressive accretion from the Indian plate. Bull. Geol. Soc. Am. 128, 1571–1592. https://doi.org/10.1130/B31471.1

Célérier, J., Harrison, T.M., Beyssac, O., Herman, F., Dunlap, W.J., Webb, A.G., 2009. The Kumaun and Garwhal Lesser Himalaya, India: Part 2: Thermal and deformation histories. Bull. Geol. Soc. Am. 121, 1281–1297. https://doi.org/10.1130/B26343.1

Clift, P.D., Hodges, K. V., Heslop, D., Hannigan, R., Van Long, H., Calves, G., 2008. Correlation of Himalayan exhumation rates and Asian monsoon intensity. Nat. Geosci. 1, 875–880. https://doi.org/10.1038/ngeo351

Corrie, S.L., Kohn, M.J., 2011. Metamorphic history of the central Himalaya, Annapurna region, Nepal, and implications for tectonic models. Bull. Geol. Soc. Am. 123, 1863–1879. https://doi.org/10.1130/B30376.1

Cottle, J.M., Jessup, M.J., Newell, D.L., Searle, M.P., Law, R.D., Horstwood, M.S.A., 2007. Structural insights into the early stages of exhumation along an orogen-scale detachment: The South Tibetan Detachment System, Dzakaa Chu section, Eastern Himalaya. J. Struct. Geol. 29, 1781–1797. https://doi.org/10.1016/j.jsg.2007.08.007

Crameri, F., 2018. Geodynamic diagnostics, scientific visualisation and StagLab 3.0. Geosci. Model Dev. 11, 2541–2562. https://doi.org/10.5194/gmd-11-2541-2018

DeCelles, P.G., Gehrels, G.E., Najman, Y., Martin, A.J., Carter, A., Garzanti, E., 2004. Detrital geochronology and geochemistry of Cretaceous-Early Miocene strata of Nepal: Implications for timing and diachroneity of initial Himalayan orogenesis. Earth Planet. Sci. Lett. 227, 313–330. https://doi.org/10.1016/j.epsl.2004.08.019

DeCelles, P.G., Gehrels, G.E., Quade, J., LaReau, B., Spurlin, M., 2000. Tectonic implications of U-Pb zircon ages of the Himalayan orogenic belt in Nepal. Science (80-.). 288, 497–499. https://doi.org/10.1126/science.288.5465.497

DeCelles, Peter G., Gehrels, G.E., Quade, J., Ojha, T.P., 1998. Eocene-early Miocene foreland basin development and the history of Himalayan thrusting, western and central Nepal. Tectonics 17, 741–

765. https://doi.org/10.1029/98TC02598

DeCelles, P. G., Gehrels, G.E., Quade, J., Ojha, T.P., Kapp, P.A., Upreti, B.N., 1998. Neogene foreland basin deposits, erosional unroofing, and the kinematic history of the Himalayan fold-thrust belt, western Nepal. Bull. Geol. Soc. Am. 110, 2–21. https://doi.org/10.1130/0016-7606(1998)110<0002:NFBDEU>2.3.CO;2

Decelles, P.G., Robinson, D.M., Quade, J., Ojha, T.P., Garzione, C.N., Copeland, P., Upreti, B.N., 2001. Stratigraphy, structure, and tectonic evolution of the Himalayan fold-thrust belt in Western Nepal. Tectonics 20, 487–509. https://doi.org/10.1029/2000TC001226

DeCelles, P.G., Robinson, D.M., Zandt, G., 2002. Implications of shortening in the Himalayan fold-thrust belt for uplift of the Tibetan Plateau. Tectonics 21. https://doi.org/10.1029/2001TC001322

Enami, M., Banno, S., 1980. Zoisite-clinozoisite relations in low- to medium-grade high-pressure metamorphic rocks and their implications. Mineral. Mag. 43, 1005–1013. https://doi.org/10.1180/minmag.1980.043.332.08

Florence, F.P., Spear, F.S., 1991. Effects of diffusional modification of garnet growth zoning on P-T path calculations. Contrib. to Mineral. Petrol. 107, 487–500. https://doi.org/10.1007/BF00310683

Gansser, A., 1964. Geology of the Himalayas. Interscience Publisher, London.

Garzanti, E., 1999. Stratigraphy and sedimentary history of the Nepal Tethys Himalaya passive margin. J. Asian Earth Sci. 17, 805–827. https://doi.org/10.1016/S1367-9120(99)00017-6

Gehrels, G., Kapp, P., Decelles, P., Pullen, A., Blakey, R., Weislogel, A., Ding, L., Guynn, J., Martin, A., McQuarrie, N., Yin, A., 2011. Detrital zircon geochronology of pre-Tertiary strata in the Tibetan-Himalayan orogen. Tectonics 30. https://doi.org/10.1029/2011TC002868

Ghosh, S., 2017. Structure and tectonics of the Darjeeling Sikkim fold thrust belts and its implication on the evolution of eastern Himalaya. Ph.D. thesis. pp. 173. http://hdl.handle.net/10603/244875

Godin, L., 2003. Structural evolution of the Tethyan sedimentary sequence in the Annapurna area, central Nepal Himalaya. J. Asian Earth Sci. 22, 307–328. https://doi.org/10.1016/S1367-9120(03)00066-X

Godin, L., Gleeson, T.P., Searle, M.P., Ullrich, T.D., Parrish, R.R., 2006. Locking of southward extrusion in favour of rapid crustal-scale buckling of the Greater Himalayan sequence, Nar valley, central Nepal. Geol. Soc. Spec. Publ. 268, 269–292. https://doi.org/10.1144/GSL.SP.2006.268.01.13

Grujic, D., Casey, M., Davidson, C., Hollister, L.S., Kündig, R., Pavlis, T., Schmid, S., 1996. Ductile extrusion of the Higher Himalayan Crystalline in Bhutan: Evidence from quartz microfabrics.

Tectonophysics 260, 21–43. https://doi.org/10.1016/0040-1951(96)00074-1

Guidotti, C. V., Sassi, F.P., 1998. Petrogenetic significance of Na-K white mica mineralogy: Recent advances for metamorphic rocks. Eur. J. Mineral. 10, 815–854. https://doi.org/10.1127/ejm/10/5/0815

Guidotti, C.V., 1984. Micas in metamorphic rocks. In: Bailey, S.W. (Ed.), Reviews in Mineralogy, vol. 13, pp. 357–467

Hébert, R., Bezard, R., Guilmette, C., Dostal, J., Wang, C.S., Liu, Z.F., 2012. The Indus-Yarlung Zangbo ophiolites from Nanga Parbat to Namche Barwa syntaxes, southern Tibet: First synthesis of petrology, geochemistry, and geochronology with incidences on geodynamic reconstructions of Neo-Tethys. Gondwana Res. 22, 377–397. https://doi.org/10.1016/j.gr.2011.10.013

Hébert, R., Huot, F., Wang, C., Liu, Z., 2004. Yarlung Zangbo ophiolites (Southern Tibet) revisited: Geodynamic implications from the mineral record. Geol. Soc. Spec. Publ. 218, 165–190. https://doi.org/10.1144/GSL.SP.2003.218.01.10

Henry, D.J., Guidotti, C. V., Thomson, J.A., 2005. The Ti-saturation surface for low-to-medium pressure metapelitic biotites: Implications for geothermometry and Ti-substitution mechanisms. Am. Mineral. 90, 316–328. https://doi.org/10.2138/am.2005.1498

Herman, F., Copeland, P., Avouac, J.P., Bollinger, L., Maheo, G., Le Fort, P., Rai, S., Foster, D., Pecher, A., Stuwe, K., Henry, P., 2010. Exhumation, crustal deformation, and thermal structure of the Nepal Himalaya derived from the inversion of thermochronological and thermobarometric data and modeling of the topography. J. Geophys. Res. Solid Earth 115, 1–38. https://doi.org/10.1029/2008JB006126

Himalaya, E., 2017. Structure and Tectonics of the Darjeeling-Sikkim fold-thrust belts and its implications on the evolution of Eastern Himalaya Subhajit Ghosh.

Hodges, K. V., 2000. Tectonics of the Himalaya and Southern Tibet from two perspectives. Bull. Geol. Soc. Am. 112, 324–350. https://doi.org/10.1130/0016-7606(2000)112<324:TOTHAS>2.0.CO;2

Hodges, K. V., Hurtado, J.M., Whipple, K.X., 2001. Southward extrusion of Tibetan crust and its effect on Himalayan tectonics. Tectonics 20, 799–809. https://doi.org/10.1029/2001TC001281

Hodges, K. V., Parrish, R.R., Housh, T.B., Lux, D.R., Burchfiel, B.C., Royden, L.H., Chen, Z., 1992. Simultaneous miocene extension and shortening in the Himalayan orogen. Science (80-.). 258, 1466–1470. https://doi.org/10.1126/science.258.5087.1466

Holdaway, M.J., 2000. Application of new experimental and garnet Margules data to the garnet-biotite geothermometer. Am. Mineral. 85, 881–892. https://doi.org/10.2138/am-2000-0701

Holland, T., Blundy, J., 1994. Non-ideal interactions in calcic amphiboles and their bearing on amphibole-plagioclase thermometry. Contrib. to Mineral. Petrol. 116, 433–447. https://doi.org/10.1007/BF00310910

Hubbard, M.S., 1989. at Geologisches Institute , Hubbard and Harrison : 40Ar / 39Ar Ages , Nepal Himalaya 8, 865–880.

Hunter, N.J.R., Weinberg, R.F., Wilson, C.J.L., Luzin, V., Misra, S., 2018. Microscopic anatomy of a "hot-on-cold" shear zone: Insights from quartzites of the Main Central Thrust in the Alaknanda region (Garhwal Himalaya). Bull. Geol. Soc. Am. 130, 1519–1539. https://doi.org/10.1130/B31797.1

Iaccarino, S., Montomoli, C., Carosi, R., Montemagni, C., Massonne, H.J., Langone, A., Jain, A.K., Visonà, D., 2017. Pressure-Temperature-Deformation-Time Constraints on the South Tibetan Detachment System in the Garhwal Himalaya (NW India). Tectonics 36, 2281–2304. https://doi.org/10.1002/2017TC004566

Imayama, T., Arita, K., 2008. Nd isotopic data reveal the material and tectonic nature of the Main Central Thrust zone in Nepal Himalaya. Tectonophysics 451, 265–281. https://doi.org/10.1016/j.tecto.2007.11.051

Jadoul, F., Berra, F., Garzanti, E., 1998. The Tethys Himalayan passive margin from Late Triassic to Early Cretaceous (South Tibet). J. Asian Earth Sci. 16, 173–194. https://doi.org/10.1016/S0743-9547(98)00013-0

Kohn, M.J., 2014. Himalayan Metamorphism and Its Tectonic Implications, Annual Review of Earth and Planetary Sciences. https://doi.org/10.1146/annurev-earth-060313-055005

Kohn, M.J., 2008. P-T-t data from central Nepal support critical taper and repudiate large-scale channel flow of the Greater Himalayan Sequence. Bull. Geol. Soc. Am. 120, 259–273. https://doi.org/10.1130/B26252.1

Kohn, M.J., Spear, F., 2000. Retrograde net transfer reaction insurance for pressure-temperature estimates. Geology 28, 1127–1130. https://doi.org/10.1130/0091-7613(2000)028<1127:RNTRIF>2.3.CO;2

Kumar, R., Ghosh, S.K., Sangode, S.J., 2003. SPECIAL SECTION: GLOBAL CORRELATION OF LATE CENOZOIC FLUVIAL DEPOSITS -- FOCUS ON INDIA - Mio-Pliocene sedimentation history in the northwestern part of the Himalayan Foreland Basin, India. Curr. Sci. - New Delhi 84, 1006–1013.

Kumar, R., Sangode, S.J., Ghosh, S.K., 2004. A multistorey sandstone complex in the Himalayan Foreland Basin, NW Himalaya, India. J. Asian Earth Sci. 23, 407–426. https://doi.org/10.1016/S1367-

9120(03)00176-7

La Roche, R.S., Godin, L., Cottle, J.M., Kellett, D.A., 2016. Direct shear fabric dating constrains early Oligocene onset of the South Tibetan detachment in the western Nepal Himalaya. Geology 44, 403–406. https://doi.org/10.1130/G37754.1

Larson, K., Cottle, J., Lederer, G., Rai, S.M., 2017. Defining shear zone boundaries using fabric intensity gradients: An example from the east-central Nepal Himalaya. Geosphere 13, 771–781. https://doi.org/10.1130/GES01373.1

Laskowski, A.K., Kapp, P., Vervoort, J.D., Ding, L., 2016. High-pressure Tethyan Himalaya rocks along the India- Asia suture zone in southern Tibet. Lithosphere 8, 574–582. https://doi.org/10.1130/L544.1

Lavé, J., Avouac, J.P., 2000. Active folding of fluvial terraces across the Siwaliks Hills, Himalayas of central Nepal. J. Geophys. Res. Solid Earth 105, 5735–5770. https://doi.org/10.1029/1999jb900292

Le Fort, P., 1975. Himalayas: the collided range. present knowledge of the continental arc. Am. J. Sci.

Mandal, S, Robinson, D.M., Khanal, S., Das, O., 2015. Redefining the tectonostratigraphic and structural architecture of the Almora klippe and the Ramgarh-Munsiari thrust sheet in NW India. Tectonics of the Himalaya 412, 247–269. https://doi.org/10.1144/SP412.6

Mandal, S., Robinson, D.M., Khanal, S., Das, O., 2015. Redefining the tectonostratigraphic and structural architecture of the Almora klippe and the Ramgarh-Munsiari thrust sheet in NW India. Geol. Soc. Spec. Publ. 412, 247–269. https://doi.org/10.1144/SP412.6

Mandal, S., Robinson, D.M., Kohn, M.J., Khanal, S., Das, O., 2019. Examining the tectono-stratigraphic architecture, structural geometry, and kinematic evolution of the Himalayan fold-thrust belt, Kumaun, northwest India. Lithosphere 11, 414–435. https://doi.org/10.1130/L1050.1

Mandal, S., Robinson, D.M., Kohn, M.J., Khanal, S., Das, O., Bose, S., 2016. Zircon U-Pb ages and Hf isotopes of the Askot klippe, Kumaun, northwest India: Implications for Paleoproterozoic tectonics, basin evolution and associated metallogeny of the northern Indian cratonic margin. Tectonics 35, 965–982. https://doi.org/10.1002/2015TC004064

Martin, A.J., 2017. A review of definitions of the Himalayan Main Central Thrust. Int. J. Earth Sci. 106, 2131–2145. https://doi.org/10.1007/s00531-016-1419-8

Martin, A.J., DeCelles, P.G., Gehrels, G.E., Patchett, P.J., Isachsen, C., 2005. Isotopic and structural constraints on the location of the Main Central thrust in the Annapurna Range, central Nepal Himalaya. Bull. Geol. Soc. Am. 117, 926–944. https://doi.org/10.1130/B25646.1

Martin, A.J., Ganguly, J., DeCelles, P.G., 2010. Metamorphism of greater and lesser himalayan rocks exposed in the Modi Khola valley, central Nepal. Contrib. to Mineral. Petrol. 159, 203–223. https://doi.org/10.1007/s00410-009-0424-3

McKenzie, N.R., Hughes, N.C., Myrow, P.M., Xiao, S., Sharma, M., 2011. Correlation of Precambrian-Cambrian sedimentary successions across northern India and the utility of isotopic signatures of Himalayan lithotectonic zones. Earth Planet. Sci. Lett. 312, 471–483. https://doi.org/10.1016/j.epsl.2011.10.027

Metcalfe RP (1993) Pressure, temperature and time constraints on metamorphism across the Main Central Thrust zone and High Himalayan Slab in the Garhwal Himalaya. In: Treloar PJ, Searle MP (eds) Himalayan tectonics, Geol Soc London (Special Publication) 74: 485–509

Mishra, P., Mukhopadhyay, D.K., 2012. Structural evolution of the frontal fold-thrust belt, NW Himalayas from sequential restoration of balanced cross-sections and its hydrocarbon potential. Geol. Soc. Spec. Publ. 366, 201–228. https://doi.org/10.1144/SP366.6

Molina, J.F., Moreno, J.A., Castro, A., Rodríguez, C., Fershtater, G.B., 2015. Calcic amphibole thermobarometry in metamorphic and igneous rocks: New calibrations based on plagioclase/amphibole Al-Si partitioning and amphibole/liquid Mg partitioning. Lithos 232, 286–305. https://doi.org/10.1016/j.lithos.2015.06.027

Mugnier, J.L., Huyghe, P., Chalaron, E., Mascle, G., 1994. Recent movements along the Main Boundary Thrust of the Himalayas: Normal faulting in an over-critical thrust wedge? Tectonophysics 238, 199–215. https://doi.org/10.1016/0040-1951(94)90056-6

Mukhopadhyay, D.K., Mishra, P., 2005. A balanced cross section across the Himalayan frontal fold-thrust belt, Subathu area, Himachal Pradesh, India: Thrust sequence, structural evolution and shortening. J. Asian Earth Sci. 25, 735–746. https://doi.org/10.1016/j.jseaes.2004.07.007

Myrow, P.M., Hughes, N.C., Derry, L.A., Ryan McKenzie, N., Jiang, G., Webb, A.A.G., Banerjee, D.M., Paulsen, T.S., Singh, B.P., 2015. Neogene marine isotopic evolution and the erosion of Lesser Himalayan strata: Implications for Cenozoic tectonic history. Earth Planet. Sci. Lett. 417, 142–150. https://doi.org/10.1016/j.epsl.2015.02.016

Myrow, P.M., Hughes, N.C., Paulsen, T.S., Williams, I.S., Parcha, S.K., Thompson, K.R., Bowring, S.A., Peng, S.C., Ahluwalia, A.D., 2003. Integrated tectonostratigraphic analysis of the Himalaya and implications for its tectonic reconstruction. Earth Planet. Sci. Lett. 212, 433–441.

https://doi.org/10.1016/S0012-821X(03)00280-2

Najman, Y., 2006. The detrital record of orogenesis: A review of approaches and techniques used in the Himalayan sedimentary basins. Earth-Science Rev. 74, 1–72. https://doi.org/10.1016/j.earscirev.2005.04.004

Najman, Y., Appel, E., Boudagher-Fadel, M., Bown, P., Carter, A., Garzanti, E., Godin, L., Han, J., Liebke, U., Oliver, G., Parrish, R., Vezzoli, G., 2010. Timing of India-Asia collision: Geological, biostratigraphic, and palaeomagnetic constraints. J. Geophys. Res. Solid Earth 115, 1–18. https://doi.org/10.1029/2010JB007673

Najman, Y., Carter, A., Oliver, G., Garzanti, E., 2005. Provenance of Eocene foreland basin sediments, Nepal: Constraints to the timing and diachroneity of early Himalayan orogenesis. Geology 33, 309–312. https://doi.org/10.1130/G21161.1

Najman, Y., Jenks, D., Godin, L., Boudagher-Fadel, M., Millar, I., Garzanti, E., Horstwood, M., Bracciali, L., 2017. The Tethyan Himalayan detrital record shows that India–Asia terminal collision occurred by 54 Ma in the Western Himalaya. Earth Planet. Sci. Lett. 459, 301–310. https://doi.org/10.1016/j.epsl.2016.11.036

Najman, Y., Johnson, K., White, N., Oliver, G., 2004. Evolution of the Himalayan foreland basin, NW India. Basin Res. 16, 1–24. https://doi.org/10.1111/j.1365-2117.2004.00223.x

Nelson, K.D., Zhao, W., Brown, L.D., Kuo, J., Che, J., Liu, X., Klemperer, S.L., Makovsky, Y., Meissner, R., Mechie, J., Kind, R., Wenzel, F., Ni, J., Nabelek, J., Chen, L., Tan, H., Wei, W., Jones, A.G., Booker, J., Unsworth, M., Kidd, W.S.F., Hauck, M., Alsdorf, D., Ross, A., Cogan, M., Wu, C., Sandvol, E., Edwards, M., 1996. Partially molten middle crust beneath southern Tibet: Synthesis of project INDEPTH results. Science (80-.). 274, 1684–1685. https://doi.org/10.1126/science.274.5293.1684

Neumann, B., 2000. Texture development of recrystallised quartz polycrystals unravelled by orientation and misorientation characteristics. J. Struct. Geol. 22, 1695–1711. https://doi.org/10.1016/S0191-8141(00)00060-2

Nicolas, A., Girardeaut, J., Marcoud, J., Dupret, B., Xibin, W., 1981. The Xigaze ophiolite (Tibet): a peculiar oceanic lithosphere 294, 414–417.

Passchier, C.W. & Trouw, R.A.J., 2005. Microtectonics. Springer, Berlin, 366 pp.

Parrish, R.R., Hodges, K. V., 1996. Isotopic constraints on the age and provenance of the Lesser and Greater Himalayan sequences, Nepalese Himalaya. Bull. Geol. Soc. Am. 108, 904–911. https://doi.org/10.1130/0016-7606(1996)108<0904:ICOTAA>2.3.CO;2

Paudel, L.P., Arita, K., 2006. Thermal evolution of the Lesser Himalaya, central Nepal: Insights from K-white micas compositional variation. Gondwana Res. 9, 409–425. https://doi.org/10.1016/j.gr.2006.01.003

Pearson, O.N., DeCelles, P.G., 2005. Structural geology and regional tectonic significance of the Ramgarh thrust, Himalayan fold-thrust belt of Nepal. Tectonics 24, 1–26. https://doi.org/10.1029/2003TC001617

PECHER, A., 1989. The metamorphism in the Central Himalaya. J. Metamorph. Geol. 7, 31–41. https://doi.org/10.1111/j.1525-1314.1989.tb00573.x

Ratschbacher, L., Frisch, W., Liu, G., Chen, C., 2014. BL-60 Kun Lun. Med. Acupunct. Pregnancy 99. https://doi.org/10.1055/b-0034-61114

Ravikant, V., Wu, F.Y., Ji, W.Q., 2011. U-Pb age and Hf isotopic constraints of detrital zircons from the Himalayan foreland Subathu sub-basin on the Tertiary palaeogeography of the Himalaya. Earth Planet. Sci. Lett. 304, 356–368. https://doi.org/10.1016/j.epsl.2011.02.009

Ravna, E.K., 2000. Distribution of Fe2+ and Mg between coexisting garnet and hornblende in synthetic and natural systems: An empirical calibration of the garnet-hornblende Fe-Mg geothermometer. Lithos 53, 265–277. https://doi.org/10.1016/S0024-4937(00)00029-3

Replumaz, A., Capitanio, F.A., Guillot, S., Negredo, A.M., Villaseñor, A., 2014. The coupling of Indian subduction and Asian continental tectonics. Gondwana Res. 26, 608–626. https://doi.org/10.1016/j.gr.2014.04.003

Richards, A., Argles, T., Harris, N., Parrish, R., Ahmad, T., Darbyshire, F., Draganits, E., 2005. Himalayan architecture constrained by isotopic tracers from clastic sediments. Earth Planet. Sci. Lett. 236, 773–796. https://doi.org/10.1016/j.epsl.2005.05.034

Robinson, D.M., DeCelles, P.G., Copeland, P., 2006. Tectonic evolution of the Himalayan thrust belt in western Nepal: Implications for channel flow models. Bull. Geol. Soc. Am. 118, 865–885. https://doi.org/10.1130/B25911.1

Robinson, D.M., DeCelles, P.G., Garzione, C.N., Pearson, O.N., Harrison, T.M., Catlos, E.J., 2003. Kinematic model for the Main Central thrust in Nepal. Geology 31, 359–362. https://doi.org/10.1130/0091-7613(2003)031<0359:KMFTMC>2.0.CO;2

Robinson, D.M., DeCelles, P.G., Patchett, P.J., Garzione, C.N., 2001. The kinematic evolution of the Nepalese Himalaya interpreted from Nd isotopes. Earth Planet. Sci. Lett. 192, 507–521. https://doi.org/10.1016/S0012-821X(01)00451-4

Robinson, D.M., Pearson, O.N., 2013. Was Himalayan normal faulting triggered by initiation of the Ramgarh-Munsiari thrust and development of the Lesser Himalayan duplex? Int. J. Earth Sci. 102, 1773–1790. https://doi.org/10.1007/s00531-013-0895-3

Schelling, D., & Arita, K., 1991. Thrust tectonics, crustal shortening, and the structure of the far-eastern Nepal Himalaya. Tectonics, 10, 851–862.

Schmid, S.M., Casey, M., 1986. Analysis of Some Commonly Observed Quartz C-Axis (a). Miner. rock Deform. Lab. Stud. 36, 263–286.

Searle, M.P., Cottle, J.M., Streule, M.J., Waters, D.J., 2009. Crustal melt granites and migmatites along the Himalaya: Melt source, segregation, transport and granite emplacement mechanisms. Earth Environ. Sci. Trans. R. Soc. Edinburgh 100, 219–233. https://doi.org/10.1017/S175569100901617X

Searle, M.P., Law, R.D., Godin, L., Larson, K.P., Streule, M.J., Cottle, J.M., Jessup, M.J., 2008. Defining the Himalayan Main Central Thrust in Nepal. J. Geol. Soc. London. 165, 523–534. https://doi.org/10.1144/0016-76492007-081

Searle, M.P., Simpson, R.L., Law, R.D., Parrish, R.R., Waters, D.J., 2003. The structural geometry, metamorphic and magmatic evolution of the Everest massif, High Himalaya of Nepal-South Tibet. J. Geol. Soc. London. 160, 345–366. https://doi.org/10.1144/0016-764902-126

Seeber, L., Armbruster, J.G., 1981. Earthquakes Along the Himalayan Arc Quaternary and Reworked Tertiary J Folding Thrusting. Earthq. Predict. An Int. Rev. 4, 259–277. https://doi.org/10.1029/9; http://dx.doi.org/10.1029/98GL02256; doi:10.1029/9

SIMPSON, C., WINTSCH, R.P., 1989. Evidence for deformation-induced K-feldspar replacement by myrmekite. J. Metamorph. Geol. 7, 261–275. https://doi.org/10.1111/j.1525-1314.1989.tb00588.x

Skemer, P., Katayama, I., Jiang, Z., Karato, S.I., 2005. The misorientation index: Development of a new method for calculating the strength of lattice-preferred orientation. Tectonophysics 411, 157–167. https://doi.org/10.1016/j.tecto.2005.08.023

Soucy La Roche, R., Godin, L., Cottle, J.M., Kellett, D.A., 2018. Preservation of the Early Evolution of the Himalayan Middle Crust in Foreland Klippen: Insights from the Karnali Klippe, West Nepal. Tectonics 37, 1161–1193. https://doi.org/10.1002/2017TC004847

Spear, F.S., 1991. On the interpretation of peak metamorphic temperatures in light of garnet diffusion during cooling. Journal of Metamorphic Geology, 9, 379–388.

Spear, F.S., 1993. Metamorphic Phase Equilibria and PressureTemperature-Time Paths. Mineralogical Society of America, Washington, DC, pp. 799.

Spencer, Christopher J., Harris, R.A., Dorais, M.J., 2012. The metamorphism and exhumation of the Himalayan metamorphic core, eastern Garhwal region, India. Tectonics 31, 1–18. https://doi.org/10.1029/2010TC002853

Spencer, C. J., Harris, R.A., Dorais, M.J., 2012. Depositional provenance of the Himalayan metamorphic core of Garhwal region, India: Constrained by U-Pb and Hf isotopes in zircons. Gondwana Res. 22, 26–35. https://doi.org/10.1016/j.gr.2011.10.004

Srivastava, P., Mitra, G., 1994. Thrust geometries and deep structure of the outer and lesser Himalaya, Kumaon and Garhwal (India): Implications for evolution of the Himalayan fold-and-thrust belt. Tectonics 13, 89–109. https://doi.org/10.1029/93TC01130

Starnes, J.K., Long, S.P., Gordon, S.M., Zhang, J., Soignard, E., 2020. Using quartz fabric intensity parameters to delineate strain patterns across the Himalayan Main Central thrust. J. Struct. Geol. 131, 103941. https://doi.org/10.1016/j.jsg.2019.103941

Stephenson, B.J., Waters, D.J., Searle, M.P., 2000. Inverted metamorphism and the Main Central Thrust: Field relations and thermobarometric constraints from the Kishtwar Window, NW Indian Himalaya. J. Metamorph. Geol. 18, 571–590. https://doi.org/10.1046/j.1525-1314.2000.00277.x

Stormer, J.C., Whitney, J.A., 1985. Two feldspar and iron-titanium oxide equilibria in silicic magmas and the depth of origin of large volume ash-flow tuffs. Am. Mineral. 70, 52–64.

Stormer, J.C.J., 1975. A practical two-feldspar geothermometer. Am. Mineral. 60, 667–674.

Stübner, K., Grujic, D., Dunkl, I., Thiede, R., Eugster, P., 2018. Pliocene episodic exhumation and the significance of the Munsiari thrust in the northwestern Himalaya. Earth Planet. Sci. Lett. 481, 273–283. https://doi.org/10.1016/j.epsl.2017.10.036

Thakur, S.S., Patel, S.C., Singh, A.K., 2015. A P–T pseudosection modelling approach to understand metamorphic evolution of the Main Central Thrust Zone in the Alaknanda valley, NW Himalaya. Contrib. to Mineral. Petrol. 170, 1–26. https://doi.org/10.1007/s00410-015-1159-y

Toy, V.G., Prior, D.J., Norris, R.J., 2008. Quartz fabrics in the Alpine Fault mylonites: Influence of pre-existing preferred orientations on fabric development during progressive uplift. J. Struct. Geol. 30, 602–621. https://doi.org/10.1016/j.jsg.2008.01.001

Tracy, R.J., Robinson, P. & Thompson, A.B., 1976. Garnet composition and zoning in the determination of temperature and pressure of metamorphism, central Massachusetts. American Mineralogist, 61, 762–775.

Valdiya, K.S., 1979. An outline of the structural set-up of the Kumaun Himalaya. J. Geol. Soc. India 20, 145–157.

Valdiya, K.S., 1980. The two intracrustal boundary thrusts of the Himalaya. Tectonophysics 66, 323–348.

Vannay, J.C., Grasemann, B., 2001. Himalayan inverted metamorphism and syn-convergence extension as a consequence of a general shear extrusion. Geol. Mag. 138, 253–276. https://doi.org/10.1017/S0016756801005313

Viruete, J.E., Indares, A., Arenas, R., 2000. P-T paths derived from garnet growth zoning in an extensional setting: An example from the Tormes Gneiss Dome (Iberian Massif, Spain). J. Petrol. 41, 1489–1515. https://doi.org/10.1093/petrology/41.10.1489

Visonà, D., Lombardo, B., 2002. Two-mica and tourmaline leucogranites from the Everest-Makalu region (Nepal - Tibet). Himalayan leucogranite genesis by isobaric heating? Lithos 62, 125–150. https://doi.org/10.1016/S0024-4937(02)00112-3

Vollmer, F.W., 1990. An application of eigenvalue methods to structural domain analysis. Bull. Geol. Soc. Am. 102, 786–791. https://doi.org/10.1130/0016-7606(1990)102<0786:AAOEMT>2.3.CO;2

Webb, A.A.G., 2013. Preliminary balanced palinspastic reconstruction of cenozoic deformation across the Himachal Himalaya (northwestern India). Geosphere 9, 572–587. https://doi.org/10.1130/GES00787.1

Webb, A.A.G., Yin, A., Harrison, T.M., Célérier, J., Burgess, W.P., 2007. The leading edge of the Greater Himalayan Crystalline complex revealed in the NW Indian Himalaya: Implications for the evolution of the Himalayan orogen. Geology 35, 955–958. https://doi.org/10.1130/G23931A.1

Whitney, D.L., Evans, B.W., 2010. Abbreviations for names of rock-forming minerals. Am. Mineral. 95, 185–187. https://doi.org/10.2138/am.2010.3371

Wintsch, R.P., Aleinikoff, J.N., Yi, K., 2005. Foliation development and reaction softening by dissolution and precipitation in the transformation of granodiorite to orthogneiss, Glastonbury Complex, Connecticut, U.S.A. Can. Mineral. 43, 327–347. https://doi.org/10.2113/gscanmin.43.1.327

Wu, C.M., 2017. Calibration of the garnet–biotite–Al 2 SiO 5 –quartz geobarometer for metapelites. J. Metamorph. Geol. 35, 983–998. https://doi.org/10.1111/jmg.12264

Wu, C.M., 2015. Revised empirical garnet-biotite-muscovite-plagioclase geobarometer in metapelites. J. Metamorph. Geol. 33, 167–176. https://doi.org/10.1111/jmg.12115

Wu, C.M., Chen, H.X., 2015. Calibration of a Ti-in-muscovite geothermometer for ilmenite- and Al2SiO5-bearing metapelites. Lithos 212–215, 122–127. https://doi.org/10.1016/j.lithos.2014.11.008

Wu, C.M., Cheng, B.H., 2006. Valid garnet-biotite (GB) geothermometry and garnet-aluminum silicate-plagioclase-quartz (GASP) geobarometry in metapelitic rocks. Lithos. https://doi.org/10.1016/j.lithos.2005.09.002

Yeats, R.S., Lillie, R.J., 1991. Contemporary tectonics of the Himalayan frontal fault system. Folds, blind thrusts and the 1905 Kangra earthquake. J. Struct. Geol. 13, 227–233. https://doi.org/10.1016/0191-8141(91)90069-U

Yin, A., 2006. Cenozoic tectonic evolution of the Himalayan orogen as constrained by along-strike variation of structural geometry, exhumation history, and foreland sedimentation. Earth-Science Rev. 76, 1–131. https://doi.org/10.1016/j.earscirev.2005.05.004

Yin, A., Harrison, T.M., Murphy, M.A., Grove, M., Nie, S., Ryerson, F.J., Feng, W.X., Le, C.Z., 1999. Tertiary deformation history of southeastern and southwestern Tibet during the Indo-Asian collision. Bull. Geol. Soc. Am. 111, 1644–1664. https://doi.org/10.1130/0016-7606(1999)111<1644:TDHOSA>2.3.CO;2